Studies on Metal Induced Crystallization of Amorphous Silicon Thin Films

A Thesis submitted for the degree of

DOCTOR OF PHILOSOPHY

In Physics

Tesi di

DOTTORATO DI RICERCA IN FISICA

by

Uma Mahendra Kumar Koppolu

University of Hyderabad
Hyderabad, India

Università degli Studi di Trento
Trento, Italy.

Hyderabad-500 046
India
May 1st 2008

DECLARATION

I hereby declare that the content embodied in this thesis entitled "***Studies on Metal Induced Crystallization of Amorphous Silicon Thin Films*** " is the result of investigations carried out by me under the internationally co-tutored PhD programme at the School of Physics, University of Hyderabad, Hyderabad, India, and at the Department of Physics, University of Trento, Trento, Italy, under the supervision of Dr. M. Ghanashyam Krishna (University of Hyderabad) and Prof. Giuseppe Dalba (University of Trento).

Place: Hyderabad

Date: **(Uma Mahendra Kumar Koppolu)**

CERTIFICATE

This is to certify that the work described in this thesis has been carried out by Mr. **Uma Mahendra Kumar Koppolu** under our collaborative supervision at the University of Hyderabad, Hyderabad, India, and at the Department of Physics, University of Trento, Trento, Italy, and this has not been submitted for any degree or diploma at this or any other University.

Place: Hyderabad
Date:

(Dr. M. Ghanashyam Krishna)

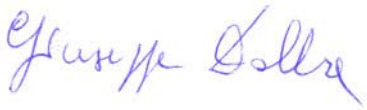

Place: Trento
Date:

(Prof. Giuseppe Dalba)

Dean
School of Physics
University of Hyderabad

Acknowledgements

It is with immense respect and gratitude; I take this opportunity to thank my mentors, Dr M Ghanashayam Krishna and Prof G Dalba for their constant support, expert guidance, and encouragement. Today I am a Physicist because of these gentlemen and fine teachers.

I am also grateful to Prof Anil K Bhatnagar for his help and advice throughout my research work.

I owe special thanks to Prof Francisco Rocca and Dr Rolly Grisenti for their support and guidance in EXAFS measurements and data analysis.

It is my pleasure to thank the Dean, School of Physics, University of Hyderabad, and the Dean, Dipartimento Di Fisica, Univesitsa Degli Study Di Trento, for their kind cooperation and providing necessary infrastructural facilities in the department. I thank all the faculty members of both the schools for their cooperation through out my PhD work.

I am also grateful to many of colleagues who have contributed to my knowledge and success in physics. In particular I thank Nasser Afify, Trivikrama Rao, Rajeeb Brahma and Sita Ramaraju. Thanks to Shiv Kiran, Krishna Chaitanya and Gangadharan for making my stay in Trento memorable.

I am deeply indebted to Prof V Sundararaja, SV University for introducing me to the fascinating field of Semiconductor Physics.

The encouragement and support provided by the non-teaching staff in the school is highly appreciable. I thank Mr. Murthy and Ms. Rama Devi of the central instrumentation lab for their patience in confocal microscopy measurements.

I also thank all the non-teaching and administrative staff for their co-operation. I wish to thank Dr PSR Prasad NGRI Hyderabad and Dr Ajay Gupta & Dr. Vasant Sathe, UGC-DAE CSR, Indore centre, for the invaluable help in Raman spectroscopy measurements.

I thank all my dearest friends for their warmth and generosity.

My sincere THANKS to my parents and my brother Rajesh without their constant support and encouragement, none of this would have been possible.

Finally I would like to thank the DST-ITPAR for providing me the *Bose-Romagnosi* fellowship and various instrumental facilities during the course of my work.

Contents

Chapter 3

Chapter 4

Chapter 1

Introduction

to

Metal induced crystallization

Metal induced crystallization

A brief treatise on Metal Induced Crystallization (MIC) in a-Si thin films is presented. Developments in fabrication of device quality polycrystalline silicon (poly-Si) thin films on inexpensive substrates and understanding the MIC processes while lowering the a-Si crystallization temperature are reviewed. Different theoretical and phenomenological models used to explain the MIC effect are also reviewed.

EXAFS as an experimental technique to study the role of metal in lowering the crystallization temperature, while studying the local environment of metal is introduced. The role of Raman Spectroscopy and its unique applicability to the Silicon research has been presented in brief. In recent years, Silicon has emerged as a new optoelectronic material; its optical properties after crystallization may be appealing to explore for different applications in large area electronics like displays, Active devices like transistors and passive electronic devices. Some of these aspects are discussed.

1.1 Nickel induced Crystallization

Hydrogenated amorphous Silicon (a-Si:H) is on of the most successful materials in the electronic industry. However, a-Si:H has its own disadvantages like, high leakage currents, lattice relaxation due to device heating, porosity in the structure, dangling bonds and various ageing problems. The industry was, therefore forced to look for an alternative material and poly crystalline Silicon (poly-Si) emerged as the best candidate to substitute a-Si: H in electronic and optoelectronic applications like flexible displays and solar cells. Poly crystalline silicon can provide logic circuits as well as pixel switching devices for display applications [1].

Most of the applications need poly silicon in thin film form, which has to be supported by a substrate. Apart from the technological point of view, the choice of substrates for the device was also based on economics. Substrates like, glass and polymers offer low production cost and thin film growth on these substrates at low temperatures is one of the challenges that has been attracting much interest. Poly-Si thin films can be obtained by following two basic methods. One is depositing poly-Si directly by LPCVD, PECVD or other CVD methods at high substrate temperatures, or first deposit the amorphous silicon followed by thermal recrystallization. This second method has been found to be the best for production of device quality silicon thin films, when compared with depositing the poly-Si thin films directly, because larger grains and smoother surfaces can be attained [2].

The three major methods to recrystallize amorphous silicon are: conventional furnace annealing (FA), rapid thermal annealing (RTA), and Excimer laser annealing (ELA). All these three methods have their own advantages and disadvantages. In ELA, for example, the substrate thermal stability is not of great concern and any kind of substrate can be used, since the thermal agitation can be confined to the depths required. But the grain size is strongly dependent on the intensity of the laser. Lack of uniformity is still an issue to overcome and it is not suitable for large area fabrication. The grain size varies from 0.005 to 0.5μm. This wide range of grain size distribution

affects the electrical characteristics of the silicon thin films. So, considering the role of grain boundaries and eventually the electrical properties, the other recrystallization techniques like furnace annealing and RTA are more suitable. They have several advantages over laser crystallization, which include smoother surfaces, better uniformity, and possibility of batch process in furnace annealing [2]. In a furnace crystallized amorphous Si, the major drawback is the long time required to transform the material. The above-mentioned methods come under one major technique called Solid Phase Crystallization (SPC).

Earlier industry has used single crystal silicon as substrate to make crystalline thin films of silicon for solar cells or for other applications. Amorphous Silicon thin films rely on the underlying single crystal silicon substrate to provide seed crystal to promote epitaxial crystallization. This process will take place typically at 600 ^{o}C to 700 ^{o}C and this was first reported by Mayer *et al.* [3]. Solid Phase Crystallization has been studied over a number of years to understand the process and achieve better control over the recrystallization. After traditional furnace annealing, at about 700 ^{o}C, to reduce the fabrication cost further there was a move to use low cost substrates like glass and polymer films. This demanded the lowering of recrystallization temperature below the softening point glass, which is around 600 ^{o}C. Therefore, there have been many attempts to decrease the crystallization temperature and to shorten the crystallization time.

An innovative method, Metal-Induced Crystallization (MIC), to fabricate polycrystalline silicon thin-film transistors, by inserting a thin, discontinuous Pd layer between the substrate and the amorphous-Si precursor was introduced by Liu and Fonash in 1993[4]. During annealing, the Pd reacted to form a silicide seed layer, reducing the crystallization time at 600 ^{o}C from tens of hours to 2 hours. Although MIC is a known science since 60's, there has been a recent emergence of interest in this area due to its technological implications. In following sections we present the details about MIC and further developments in this field.

1.1.1 Phenomenological model for MIC

Thin film metal silicides play an essential role in the integrated circuit industry [5]. The ability of retaining their good electrical characteristics even below the sub micron lateral and vertical dimension made these silicides attractive materials in CMOS technology. Amongst all silicides, Nickel silicides are the most interesting, as their sheet resistance remains unchanged even for lines down to 0.1 μm [6, 7]. During structural and other studies of these nickel silicides, Cammarata *et al.* found that these silicides catalyzed the formation of crystalline silicon(c-Si) [8]. This phenomenon was named as Silicide Mediated Crystallization (SMC). The presence of a little metallic phase enhances the growth of c-Si [9, 10]. One of the systems that have received considerable attention is Indium (In) implanted a-Si [11]. Another report of enhancement of the solid phase crystallization in Si is through the Pd_2Si layer [12]. The next system that has taken advantage of the silicide formation in the transformation of Si from amorphous to crystalline phase is $NiSi_2$, where nickel is the dominant species of diffusion. Hayzelden and Bastone proposed a mechanism for the enhancement of crystallization in low temperature annealing of Ni implanted amorphous silicon thin films in 1993[13]. This is the very first report of this kind. Based on this model, later a large number of articles appeared in literature.

These authors (Hayzelden and Bastone) implanted nickel in to a-Si and used transmission electron microscopy for their study. According to Hayzelden *et al.* there are three major steps in MIC,

- Precipitation of $NiSi_2$,
- Nucleation of Si on $NiSi_2$ precipitates,
- Subsequent migration of $NiSi_2$ precipitates and the enhancement of Si crystallization at temperature as low as 484 ^{o}C.

Nickel is added or doped in to a-Si film in many different ways. Hayzelden and Bastone used ion implantation. Gulliants *et al.* [14] used a pre-layer of nickel before deposition of a-Si. Yoon *et al.*, Jang *et al.* [15] used a top-layer of nickel either patterned or blanketed thin film followed by annealing for the realization of MIC. Figure 1.1 shows the very beginning stage of MIC [16]. Once the silicon thin film

with nickel blanket is annealed, the $NiSi_2$ precipitation all over the film is observed. In the case of Hayzelden and Bastone the precipitation and precipitate areal number density was dependent on the Nickel dose implanted,

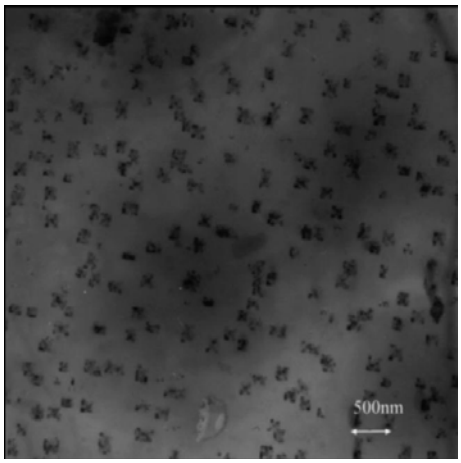

Figure 1.1: Plane view of TEM image for the 30-nm-thick Si film with 0.5 nm thick Ni and annealed at 450 ^{o}C.[16]

i.e the precipitation rate is dependent on the nickel concentration and a critical concentration of metal is proposed for precipitation to start [17]. Once the silicides start precipitating, the migration of $NiSi_2$ through the a-Si thin film also starts, leaving behind a trail of c-Si in the form of needle like structures as shown in figure 1.2. It is found that these needles like structures are led by $NiSi_2$ precipitates.

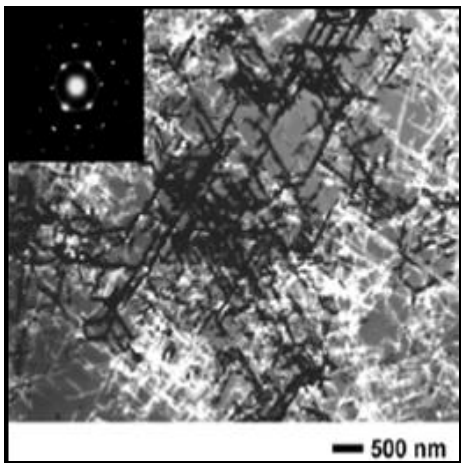

Figure 1.2: The TEM images of a Ni-SMC poly-Si film crystallized at 400 ^{o}C [15]

These precipitates migrate through several tens of microns. The crystalline part of Si frequently showed {110} orientation. *In situ* studies revealed that the nucleation of epitaxial c-Si occurred first on one or more faces of {111} plane of the individual precipitates. The growth direction of epitaxial c-Si, is then purely dependent on orientation of $NiSi_2$ precipitate. A detailed investigation of silicide mediated crystallization of silicon was described by Hayzelden *et al.* The driving force for the migration of $NiSi_2$ in a-Si is explained in terms of chemical potential of diffusing species. The chemical potential of Ni is low at $NiSi_2$/a-Si interface and for Si the chemical potential is low at $NiSi_2$/c-Si interface. A migrating $NiSi_2$ precipitate consumes silicon atoms at the leading interface and leaves a trail of c-Si behind. There is a driving force for forward diffusion of Ni atoms through the $NiSi_2$ precipitate and a driving force for Si atoms in the reverse direction through the $NiSi_2$. The diffusion of these to kinds of atoms Ni and Si can be explained based on two models, One is dissociate and other is the non-dissociate model. In dissociate model, the $NiSi_2$ layer dissociates to provide free silicon for epitaxial growth at $NiSi_2$/c-Si, with new $NiSi_2$ formed at the leading $NiSi_2$/a-Si interface. In this case all the silicon atoms that are originally in $NiSi_2$ layer would be incorporated in the epitaxially grown c-Si and replaced by Si atoms from the a-Si. In the non-dissociate model, Si atoms will simply diffuse through the $NiSi_2$ from the a-Si and bond to the epitaxial c-Si.

1.1.2 Field induced crystallization

The crystalline seed (metal silicide phase) can propagate into the metal-free area by thermal diffusion (Metal Induced Lateral Crystallization: MILC), thus obtaining good quality of poly-Si film without metal contamination. Crystallization by MILC, however, takes relatively long time since crystallization velocity is determined mainly by a sluggish diffusion process. The recognition of the role of $NiSi_2$ resulted in the development of Field Assisted or induced crystallization (FALC). Being a metallic phase, $NiSi_2$, could be driven by the electric field. Therefore, by applying an electric field during the crystallization, the transformation rate could be enhanced due to the

increased diffusivity of $NiSi_2$. As the electric field, of the order of 80V/cm, is applied across the film the crystallization time at 500 ^oC decreases from 25 h to 10 minutes and the thin film is completely crystalline and no amorphous phase is detected [18]. The net charge of the Ni atoms inside silicon matrix is negative and the nickel diffusion enhances due to the application of electric field [19]. In another report Kim *et al.* [20] used UV annealing to control the shape and size of the Silicon crystallites. These authors found an optimum Ni atom concentration as follows.

- Needle like growth 2.5×10^{13} cm^{-1} (Ni atom conc.)
- Small grain like growth 1.4×10^{13} cm^{-1} (Ni atom conc.)

To form nucleation sites a critical density of Ni atoms is needed. When UV light was used along with MIC for annealing, a-Si partially crystallized with a circular shape of grains. This phenomenon was ascribed to the Joule heating effect caused by the large current density in the film [21]. However, these two observations cannot be compared directly because the applied electric fields are high in the case of Sun *et al.* (of the order of 200 V/cm) where as in the report by Jang *et al.* it was just 80V /cm.

In conclusion we can say that in field assisted metal induced crystallization,

1. ***Ni is the diffusing species in a-Si matrix. Significantly, No report indicates that $NiSi_2$ are moving with applied voltage.***
2. Ni atoms are negatively charged in a-Si network
3. Upon applying the electric field the diffusion coefficient increases
4. The annealing times have decreased substantially from 25 h to 10 minutes.
5. According to Li *et al.,* the crystallization process is ascribed to the Joule heating effect caused by large current densities

1.1.3 Metal induced growth

Guliants *et al.* [14] have given a new insight about the epitaxial growth of Si on $NiSi_2$ seed layer. The group has proposed a new model called metal induced growth. The growth of the poly Si has been explained as follows:

A 25 nm thick Ni layer was deposited on glass and on its top a-Si thin films was deposited by RF magnetron sputtering. The Si atoms that are arriving towards the

substrate, which is already coated with Ni pre layer of 25 nm, will readily react with Ni and form a $NiSi_2$ layer. This will further work as template for the growth of poly-Si epitaxially. In this method of deposition one important point that has to be noted is that the substrates prior to the deposition and while deposition are maintained at 500 ^oC. The overall advantage of this processing method is that post deposition annealing can be avoided. The report states that no migration of $NiSi_2$ nodules was observed in the Silicon thin film. The growth and crystallization takes place simultaneously and hence no further annealing is needed.

1.1.4 Kinetic many body model

Yu L Khait *et al.* [23] proposed a model which explains the re-growth mechanism of pure and doped semiconductors. The model explains the enhanced recrystallization rate in a-Si when Boron(B) Phosphorus (P) and Arsenic (As) atoms are introduced, as well as the reduced crystallization rate due to the presence of Oxygen and Carbon atoms.

It was suggested that in pure a-Si the crystallization starts from nucleation, followed by epitaxial growth [24]. It has been assumed that the dopant atoms inside the a-Si will modify the Fermi level, which helps in recrystallization. For the recrystallization process the Silicon atoms have to move from a disordered state to a more ordered state. This transition takes place via energy fluctuation assisted jump over a barrier of height E >> kT. Only those atoms whose thermal energy is more than this barrier energy contribute to the "ordered jump". These jumps are sometimes of the order of interatomic distance creating short-lived energy fluctuations (SLEF). These SLEFs' induce potential wells where the free electrons are trapped. This transient localization of weakly bonded electrons results in release of energy 'δE' in the vicinity of the atoms and that energy was utilized by the atoms to hop to more ordered positions. Therefore the re-growth rate increases by $\exp\left(\frac{\delta E}{kT}\right)$. This rate is purely dependent on the probability of energy release and its utilization.

1.1.5 The effect of film thickness and dopants on MIC

The effect of thickness and dopants of silicon thin in the metal-induced laterally crystallized process MILC has been studied by Tianfu Ma and Man Wong [25]. The MILC length decreases gradually with decreasing thickness. Below 30 nm, a more drastic reduction is observed, with essentially no observable MILC for the 10 nm thick films. The MILC length of the boron, implanted samples after 24 h of heat treatment is for a sample 100 nm thick, Boron at a high dose of 33 x 10^{15} /cm^2 is found to drastically accelerate the MILC rate, while phosphorus or arsenic at the same dose decelerates slightly the MILC rate. The MILC is more sensitive to the nature of the substrate material on which the a-Si thin films are deposited. The MILC rate of an intrinsic sample on thermal oxide, and those of the samples on phosphosilicate glass PSG substrates are significantly reduced. Interestingly, the MILC rate enhancement at high boron doping was not observed on the PSG substrates. The morphology of an intrinsic sample on PSG substrate is far different from the film grown on thermal oxide.

1.2 EXAFS Spectroscopy in MIC studies

Different metal inclusions have been used to crystallize amorphous Silicon. Different phenomena were observed and reported on the interaction of metals with amorphous silicon. Metals such as Al and Au [25, 26] do not form silicides while others such as Pt and Pd and Ni [28, 29, 30] form a silicide even at room temperature.

1.2.1 Aluminum (Al) Induced crystallization

EXAFS studies to understand the metal induced crystallization were earlier carried out in the case of aluminum (*Al*) induced crystallization in hydrogenated amorphous germanium (a-Ge:H) and in the case of Gold (Au) induced crystallization of amorphous Germanium (a-Ge)[25,26]. The degree of reduction in the crystallization temperature was found to be dependent on the type of metal-semiconductor contact [26]. Al, Au metal induced crystallizations broadly fall in the category of heterogeneous nucleation where a foreign particle acts as a nucleation center and then

the substance will crystallize and grow on that nucleus as crystallites. In Al induced crystallization also, Al offers such a nucleation center for germanium to become crystalline after annealing.

Chambouleyron *et al.* [25] have studied Al crystallization in a-Ge and proposed a phenomenological model. According to this model, in side the a-Ge matrix aluminum will form Al_4 rigid entities due to compressive stress and Sp^3 hybridisation. This causes the Al-Ge first shell distance to shrink and more order is likely to be expected. When Gallium (Ga) atoms are doped in to a-Ge:H [27] there is increase in the local order with increase in the doping concentration . Based on these considerations the following conclusions were drawn

- Al_4 will be present at perfectly tetrahedral site in the a-Ge lattice.
- Al-Ge distance may be similar to the Ge-Ge distance aiding the epitaxy
- Thus these tetrahedral sites will act as "nucleation seeds" for germanium crystallization

From the above study one can conclude that an impurity in the amorphous network will make bonds with the host material in such a way that nucleation takes place. This could be explained as a kind of heterogeneous nucleation.

1.2.2 Gold (Au) Induced crystallization

EXAFS studies on gold (Au) induced crystallization were reported by Tan *et al* [26]. In the authors view "The lowering of the crystallization temperature does not seem to be due to a seeding effect since crystalline Si and Ge contacts do not induce similar crystallization". The environment of the Au and Ge were determined by Ge K edge EXAFS and Au L_3 edge. The brief summary of EXAFS results is as follows

- In the amorphous state Au-Ge bonding are observed and upon crystallization bonding is weakened or broken.
- In the amorphous sample Au has Ge atoms around but not Au atoms, suggesting metal clustering is absent. After annealing or after crystallization

of Ge, Au forms FCC metal clusters which are not observed before crystallization.

- This metal is squeezed out of the crystalline Ge, because of lower solubility.

Summarizing, the above two studies suggest that metallic nature of the contact is playing a significant role in lowering the crystallization temperature. The metal concentration and annealing temperature dependence on Metal-Germanium (M-Ge) bonding and bond breaking has to be addressed to understand the phenomenon of metal induced crystallization.

It is clear from the foregoing that the process of Metal Induced Crystallization of silicon has great technological consequences. The process has been known for many years but it is not very well understood. The main issues need to be addressed are

- The role of processes in lowering the crystallization temperature.
- Exact nature of influence of the seed layer
- Effect of film substrate interface on MIC.
- Ability to lower the MIC temperatures by an optimized combination of these factors.

In the light of these observations, Studies on Ni induced crystallization in a-Si thin films using EXAFS technique become one of the themes of this particular thesis. The data collection, reduction and analysis are presented in the subsequent chapters.

1.3 Raman Spectroscopy in Silicon Research

Raman spectroscopy is a non-destructive optical method to characterize the phase sensitive vibrational properties of Silicon. It is well known that amorphous Silicon (a-Si) and crystalline Silicon (c-Si) exhibit characteristic Raman peaks at 480 and 520 cm^{-1} respectively. The peak position, shape and its area have structural information about the material under investigation. This following section describes briefly the structural details which can be derived form Raman spectra in the case of a-Si, nanocrystalline and c-Si. The Raman frequency shift has correlation with bond angle distribution and crystallite size, the broadening of the Raman peak was attributed to

the phonon confinement in nanocrystalline material and in turn, its shape and size are obtained form characteristic Raman peak analysis. These details are explained briefly in the context of nanocrystalline silicon.

1.3.1 Amorphous Silicon

The experimental Raman spectra of a-Si have two distinct bands at 150 and 480 cm^{-1} associated with transverse acoustic (TA) and transverse optic (TO) vibrational modes, respectively. The TO band in the Raman spectra is more sensitive to the structural changes. The shift in the TO band is related to the root mean square bond angle variation [31]. Vink *et al.* [32] proposed a semi empirical relation between the Raman peak width 'Γ' and the variation in the bond angle 'Δθ' in a-Si network. The amorphous silicon network local order is greatly influenced by the preparation method and conditions. According to Vink *et al.* the empirical relation ship between the Raman peak width 'Γ' and the bond angle variation 'Δθ' is given by

$$\frac{\Gamma}{2} = 3.3\Delta\theta + 9.2 \qquad \ldots\ldots\ldots\ldots\ldots\ldots\ldots\ldots (1.1)$$

Raman peak position 'ω_{TO}' and bond angle variation are related by

$$\omega_{TO} = -2.5\Delta\theta + 505.5 \quad \ldots\ldots\ldots\ldots\ldots\ldots\ldots (1.2)$$

Where, ω_{TO} is the Raman peak position. According to this equations the shift in ω_{TO} of 7.5cm^{-1} going from unannealed a-Si ($\Delta\theta = 13^{o}$) to the annealed sample ($\Delta\theta = 10^{o}$). Sokolov *et al.* [33] proposed a correlation between, the Raman peak intensity and the optical band gap of the a-Si. The TA band intensity goes to zero for an 'ideal a-Si' whose optical band gap is equal to 2.0 to 2.2 eV with no structural disorder and hence no Urbach tails. However, Raman spectral changes are more sensitive to the structural changes in the medium range scale of about 0.4-0.6 nm.

When a-Si is hydrogenated, the amorphous network relaxes with a decrease in the bond angle variation. This fact was experimentally proved by Raman measurements of Wakagi *et al.* [34] where $\Delta\theta = 11.4$ for a-Si and after hydrogenation decreases to $\Delta\theta = 8.8$. The EXAFS measurements show that the bond lengths are larger in the

amorphous silicon compared to crystalline by 0.014 Å while those for amorphous silicon hydrogenated were 0.009 Å only. These observations have confirmed that the hydrogenation relaxes the a-Si network. The Raman peak positions shifted downwards to 462 cm^{-1} for Si-Si bonds in a-Si in the absence of clustering. When clustering occurs, the a-Si peaks shift towards 477 cm^{-1} for Si_{200} and 470 cm^{-1} for Si_{50}.

1.3.2 Crystalline hydrogenated silicon

Iqbal *et al.* reviewed the application of Raman spectroscopy in the research of microcrystalline silicon (μc-Si) [35]. Crystalline silicon has a Raman peak centered at 520 cm^{-1} originating from the Raman allowed frequency at Γ'_{25} to Γ'_5 transition in the single crystal silicon. This peak position has been reported by various authors to be between 520 and 522cm^{-1} [36, 37]. However, a careful calibration says that the crystalline silicon has Raman peak at 520cm^{-1}. Significantly, when silicon thin films were deposited on different substrates, no significant differences were observed in the Raman spectra.

1.3.3 Crystallite Size and Raman Frequency

A downward shift in the central Raman frequency of poly-Si is observed when the crystallite size decreases down to 3 nm from the single crystal value of 520cm^{-1} to 512 cm^{-1}. The decrease in the Raman frequency is attributed the lattice expansion in both crystalline and amorphous components of silicon. However, stress inside the films grown while deposition will also shift the Raman peaks towards lower frequency. The shift is dependent on the crystallite size rather than on the hydrogen content. Hydrogen, rather, plays a secondary role of relaxing the amorphous network subsequently contributing to variation in the lattice expansion.

However, an alternative and equally attractive explanation for downward shift of the Raman peaks is given by the *phonon confinement model* based on correlation length. This phenomenological model, called '*RCF model*', was proposed by Ritcher *et al.* [38, 39] and later improved by Pisanec *et al.* [40]. In this model, the spectral position

and peak broadening of the Raman peak were brought in to context to account for variations with size and morphology(nano dot and nano rod) of the nanocrystalline silicon.

The Raman intensity in the RCF model is given by

$$I(\omega) = \int \frac{|C(0,q)|^2}{[\omega - \omega(q)]^2 + (\Gamma_0/2)^2} d^3q \quad \ldots\ldots\ldots\ldots\ldots\ldots (1.3)$$

Where $|C(0,q)|^2 = \exp\left(\frac{-q^2d^2}{16\pi^2}\right)$ and $\omega(q) = [A + B\cos(q\pi/2)]^{0.5} + D$ and

A=1.74x10^5 cm^{-2}

B=10^5 cm^{-2}.

Later it was found that the correlation model does not give a satisfactory description of Raman band shape modifications below 4 to 5 nm. Zi *et al.* [41] established a model, which relates the Raman shift with the size of the silicon sphere.

$$\Delta\omega(D) = -A\left(\frac{a}{D}\right)^{\gamma} \quad \ldots\ldots\ldots\ldots (1.4)$$

Where $\Delta\omega(D)$ is the Raman peak shift in a nanocrystals with diameter D, '*a*' is the lattice parameter, A=47.41 cm^{-1} and γ = 1.44 are the fit parameters that describe the phonon confinement in nanometric spheres of silicon.

Another possible reason for the shift in the Raman peak is the temperature reached by the sample while irradiating with laser. As reported by Viera *et al.* [42] the Raman peak modifications due to the local temperature can give a wrong value for the calculated crystallite size. For this reason, care has to be taken that Raman spectra are not misinterpreted.

Based on this knowledge, with in the framework of this thesis, we have applied Raman spectroscopy to characterize the metal induced crystallization in Si thin films on glass. A detailed line profile analysis [43] has been given to extract the contribution from a-Si, grain boundaries and from nc-Si.

1.4 Silicon optical properties

Information on fundamental optical parameters like refractive index, absorption coefficient and band gap information is of practical importance. Many optical devices like wave guides, fibers, coupling devices works, based on the difference between in refractive index of the materials and its surrounding environment. Thus, precise determination of refractive index of the material has paramount importance from an application point of view. Another aspect of the studies is variation of refractive index as a function of wavelength, history of thermal treatment and the structural changes due to doping and crystallization. The same is true for the optical absorption coefficient determination. This single parameter determines the quality of the amorphous silicon layer, whether it has application potential in solar cells or not; where absorption of solar radiation, is the predominant factor. The behaviour of refractive index and optical absorption of a-Si and its correlation with structural factors are discussed in the following sections.

1.4.1 Refractive Index

Wemple in his classic work in 1973 [44] depicted the structural properties in terms of optical constants. An empirical relationship has been derived between the refractive index and the structural and chemical quantities like coordination number and chemical valence. Often the amorphous materials suffer from deficiency of density when compared to their crystalline counter parts. Usually amorphous films exhibit a void content of about 15% depending upon the method of preparation and conditions. However, it is a well known fact that the atoms in the covalent semiconductors like Si and Ge will retain their tetrahedral coordination.

The coordination number and refractive index are related in terms of optical dispersion energy 'E_d',

$$n^2 - 1 = \frac{E_d E_o}{{E_d}^2 - E^2} \quad \text{..... (1.5)}$$

Where E_d, is the dispersion energy and E_O, is the Effective Dispersion Oscillator energy.

And E_d is defined as

$$E_d = \beta N_c Z_a N_e \qquad \text{..... (1.6)}$$

Where $\beta = 0.37 \pm 0.004$ for covalent materials

And $\beta = 0.26 \pm 0.003$ for ionic materials

N_c = Coordination number of cation nearest neighbour to the anion

Z_a = Chemical valence of the anion

N_e = Total number of valence electron per anion

At this juncture we should emphasize some of the facts from the discussion. The refractive index is characterized by the dispersion energy E_d, which is in turn related to the coordination number (Eq.(1.6)) of the anion and number of valence electrons available per anion. Apart from the inefficient packing, in disordered materials, the nearest neighbour coordination affects the refractive index.

Another interpretation of the refractive index behaviour is in terms of the ***Penn gap***. The Penn gap has the units of energy and is the same energy described in Eq.(1.5) as E_o. Usually, the interpretations were found for hydrogenated amorphous Silicon (a-Si: H). The increase in Penn gap is a measure of *bond strength* that can be sensibly divided in to covalent and ionic contributions. For crystalline Silicon(c-Si), Penn gap was 4.8 eV whereas for a-Si the value decreases to 3.7 eV due to weakening of the Si-Si bonds in a-Si [45, 46, 47].

The relation between the Penn gap and refractive index was given in Eq.(1.5). In a few cases the refractive index of the a-Si thin films was greater that that of the c-Si. In unhydrogenated a-Si thin films the refractive index ranges from 3.4 to 4.1 (in the dispersion free region) whereas for the c-Si it is 3.4 only. The reason given for this is the reduced Penn gap in a-Si and refractive index decreases upon annealing because the Penn gap increases with the relaxation of the strained network in a-Si.

In this thesis we have presented behaviour of the refractive index (n) of a-Si thin films. Amorphous Silicon thin films were blanketed with Ni and Cr metal and then annealed. The behaviour of n was explained on the basis of the above mentioned empirical relationship. Other phenomenological effects also considered, such as the inhomogeneity that arises due to silicide formation in the case of Ni and Cr doped thin films. We have proposed a model to explain the dispersion curves based on the assumption of formation of a layered silicide structure formation in the a-Si thin after annealing.

1.4.2 Optical absorption and Urbach edge

Optical absorption measurements are the simplest experiments, amongst all, to probe the electronic band structure of materials. The sample under investigation is placed in front of the output of a monochromator that excites electrons, which allows one to discover all the possible transitions an electron can make and in turn the distribution of energy levels. These include all possible kinds of transitions such as band to band, excitons, between sub bands, between impurities and bands and many more. Thus, from a simple measurement a detailed picture of the electronic structure can be obtained.

The optical absorption coefficient is proportional to the probability of transition at the incident photon energy from initial state to the final state. Thus, the probability depends on the available final energy levels, number of electrons available in the initial state and the process is resultant of all transitions possible between those two energy levels.

Among different kinds of transitions, band to band transitions are more intense ones. Based on the quantum selection rules the absorption coefficient is given as [48]

$$\alpha(h\upsilon) \approx 2 \times 10^4 \left(h\upsilon - E_g\right)^{1/2} \qquad \ldots\ldots\ldots\ldots\ldots\ldots (1.7)$$

$$\alpha(h\upsilon) \approx 1.3 \times 10^4 \left(h\upsilon - E_g\right)^{3/2} \qquad \ldots\ldots\ldots\ldots\ldots\ldots (1.8)$$

These two equations represent the absorption coefficient of band to band direct allowed and direct forbidden transitions.

The above two equation can be generalized as follows

$$\alpha h\upsilon = B\left(h\upsilon - E_g\right)^r \qquad \ldots\ldots\ldots\ldots\ldots\ldots (1.9)$$

Where 'r' and inter represents the type of the transitions

Direct allowed	1/2
Direct forbidden transitions.	3/2
Indirect allowed	2
Indirect forbidden	3

Where B is a transition matrix element and E_g is the optical band gap.

The energy gap can be determined in several ways. The photon energy at which the absorption coefficient reaches the order of 10^4 or 10^3 cm^{-1} is considered as E_{04} or E_{03}. A second method was proposed by Tauc *et al.* [49] and most of the experimentalists use this method of extrapolation. In the Tauc method, the absorption coefficient is plotted in the form of $(\alpha h\upsilon)^r$ Vs hυ yields a curve whose linear part is extrapolated to the zero of absorption coefficient. The point at which the extrapolated line intersects the energy axis, determines the band gap energy.

Alkaline halides, semiconductors like CdS, and several different kinds of materials have exhibited entirely different functional dependence of photon energy on absorption coefficient. Normally in direct allowed band to band transitions the "α" will rise by several orders of magnitude with in the few tenths of an electron volt near the absorption band edge. However, in amorphous materials even if the direct

allowed band to band transitions occur, one can observe a gradual increment in the 'α' extending over several electron volts. This behaviour of the absorption edges was first observed by Urbach [50] and postulated that the edges obey an empirical law

$$\alpha = \alpha_o \exp\left\{-\gamma' \frac{(E_o - h\upsilon)}{kT}\right\} \quad \ldots\ldots\ldots\ldots\ldots\ldots (1.10)$$

γ' is a constant, T is the absolute temperature. The edge broadens when the temperature increases. These types of edges are usually the most characteristic feature of the amorphous semiconductors. Different models have been proposed to explain the origin of the Urbach edges.

Popular model was the broadening of the absorption coefficient in the presence of electric field. Dow and Redfield proposed a model based on micro-electric fields present in the materials that would modify the finite probability for tunneling of the Bloch states in to the gap.

A possible explanation was also given by Tauc [51] and Lanyon [52] based on the electronic transitions between localized energy states with in the band edge. However, Davis and Mott opposed this idea on the basis that a wide variety of materials exhibit similar kind of slope and it was unlikely to have state tailing so similar in all materials.

In the absence of the electric fields the absorption coefficient follows exponential law given by

$$\alpha(h\upsilon) \approx 10^5 \times \frac{(h\upsilon - E_o)}{h\upsilon} cm^{-1} \ldots\ldots\ldots\ldots\ldots (1.11)$$

Where E_o is the optical band gap. This optical band gap is different from the one derived by Tauc method, discussed earlier. The distinction is given by Davis and Mott [53] in their classic work in 1970.

According to Davis *et al.* the Tauc gap actually measures the mobility gap and when the 'α' curve is fitted to the Eq.(1.11) one can determine E_o. The difference $\Delta E = E_g - E_o$ gives the energy distribution of the states inside the forbidden gap.

As a part of the thesis work the different models which explain the origin of Urbach edges are verified, the distribution of localized energy states in the forbidden band gap are also derived.

The present work, thus, relies on the motivation of these earlier studies to understand the optical properties of the silicon thin films crystallized by metal induced crystallization. The potential application of MIC crystallized silicon thin films in the silicon based optical devices is explored, while determining the fundamental optical characteristics of the material which can be utilized by communities working in basic research as well as in industry for silicon optoelectronics and other fields.

Reference:

1. J R Ayers, S D Botherton and N D Young *Solid State Electron*. **34** 671 (1991)
2. K. Nakazawa and K. Tanaka. *J. Appl. Phys*, **68** 1029 (1990)
3. J W Mayer, L Eriksson, S T Picraux and J A Davies *Can. J. Phys*. **46** 663 (1968)
4. G. Liu and S. J. Fonash. *Appl. Phys. Lett*, **62** 254 (1993)
5. K.N.Tu. *Advances in electronic materials*. pp-147, Metals Park, OH American Society Of Metals. (1986)
6. M. Koike T. Morimoto A. Nishiyama Y. Ushiku T. Yoshitomi M. Ono M. SatoT. Ohguro, S. Nakamura and H. Iwai. *IEEE Trans. Electron Devices*,**41** 2305 (1994)
7. E. Yoon C. Blair, E. Demirlioglu and J. Pierce. Editors S. Mantl R. W. Fathauer, L.Schowalter and K. N. Tu, in *Silicides, Germanides, and Their Interfaces*, pp 53, Materials Research Society, Pittsburgh, MRS Symp. Proc. No. 320. (1994)
8. C. Hayzelden and K.N.Tu R.C.Cammarata, C.V.Thomson. *Jour. Mater. Res*, **5** 2133 (1990)
9. R S Wagner and. WC Ellis *Appl. Phys. Lett*, **4** 89 (1964)

10. S. R. Herd, P. Chaudhari and M. H. Brodsky *J. Non-Cryst. Solids*, 7 309 (1972)
11. E. Nygren, A. P. Pogany, K. T. Short, J. S. Williams, R. G. Elliman, and J. M. Poate, *Appl. Phys. Lett.* 52, 439 (1988)
12. C. Canali, J. W. Mayer, G. Ottaviani, D. Sigurd, and W. van der Weg, *Appl. Phys. Lett*. **25**, 3 (1974)
13. C. Hayzelden and J. L. Batstone, *J. Appl. Phys.* **73**, 8279 (1993)
14. E. A. Guliants, W. A. Anderson, L. P. Guo and V. V. Guliants, *Thin Solid Films*, **385,** 74 (2001)
15. Soo Young Yoon, Seong Jin Park, Kyung Ho Kim and Jin Jang *Thin Solid Film* **383** 34 (2001)
16. Y. Uchida, N. Katsumata and K. Ishida *Thin Solid Films*, **427** 294 (2003)
17. Jong Hyun Choi, Do Young Kim, Seung Soo Kim, Seong Jin Park and Jin Jang *Thin Solid Films*, **440** 1 (2003)
18. Jang Jin, Oh Jae Young, Kim Sung Ki, Choi Young Jin, Yoon Soo Young, and Kim Chae Ok *Nature* **395** 481 (1998)
19. Hiroko Murakami, Kazunori Ono and Hiroshi Takai, *Applied Surface Science* **117** 289 **(**1997)
20. Kyung Ho Kim, Seong Jin Park, Ah Young Kim and Jin Jang, *Journal of Non-Crystalline Solids* **299** 83 **(**2002)
21. J.F. Li, X.W. Sun, M.B. Yu, G.J. Qi and X.T. Zeng *Applied Surface Science* **240** 155 (2005)
22. Yu L Khait and R Beserman *Phys. Rev* B, **33** 2983 (1986)
23. J W Christian, in *Physical Metallurgy* edited by P N Cahn (North Holland, Amsterdam, (1970)
24. Tianfu Ma and Man Wong. *J. Appl. Phys*, **91** 1236 (2002)
25. I. Chambouleyron, F. Fajardo, and A. R. Zanatta, *Appl. Phys. Lett*. **79**, 3233 (2001)
26. Tan, Zhengquan S. M Heald, M. Rapposch, C. E Bouldin, J. C Woicik, *, Phys. Rev. B* **46**, 9505 (1992)

27. G. Dalba, P. Fornasini, R. Grisenti, F. Rocca, D. Comedi, and I. Chambouleyron, (1999)*Appl. Phys. Lett*. **74**, 281.
28. Köhler U K Demuth J E and Hamers R J (1988)*Phys. Rev. Lett*. **60** 2499,
29. C. Canali J W, Mayer G, Ottaviani D, Sigurd, and W F van derWeg, (1974) *Appl. Phys. Lett*. **25**, 3.
30. OS S Lau and W F van der Weg, in '*Thin Films-Inter diffusion and Reactions*, edited by J M Poate, K N Tu, and J W Mayer (Wiley,New York, 1978), p. 450.
31. W C Sinke , S Roorda, and F W Saris *J. Mater. Res* **3** 1021 (1988)
32. R L C Vink, G T Barkema, W F van der Weg, *Phys. Rev B* **63** 115210 (2001)
33. A P Sokolov, A P Shebanin, O A Golikova and M M Mezdrogina *Journal of Physics: Condensed Matter* **3** 9887 (1991)
34. M Wakagi, K Ogata and A Nakano, *Phys. Rev. B* **50** 10666 (1994)
35. Z Iqbal and S Veprek *J. Phy. C: Solid State Phys* **15**, 377 (1982)
36. G Kanellis, J F Morhange and M Balkanski *Phys. Rev B* **21** 1543 (1980)
37. R Tsu, M Izu S R Ovinsky and F H Pollak *Solid State Commun*. **36** 817 (1980)
38. H Richter and L Ley *J. Appl. Phys.* **52** 7281 (1981)
39. I H Campbell and P M Fauchet *Solid State Commun*. **58** 739 (1986)
40. S Pisanec, MContoro, A C Ferrari, J A Zapien, Y Lifshitz, S T Lee, S Hofmann and J Robertson *Phys. Rev. B* **68** 241312(R) (2003)
41. Jian Zi, H. Buscher, C. Falter, W. Ludwig, Kaiming Zhang, and Xide Xie, *Appl. Phys. Lett.* **69**, 200 (1996)
42. G. Viera, P. Roca I Cabarrocas, J. Costa, S. Martinez,. E. Bertran, *Mater. Res Soc Symp Proc* **507** 993 (1998)
43. E Schubert, J Fahlteich, B Rauschenbach, M Schubert, M Lorenz, M Grudmann and G Wagner *J. Appl. Phys.* **100** 016107 (2006)
44. S H Wemple *Phys. Rev B* **7** 3767 (1973)
45. E C Freeman W Paul *Phys. Rev. B* **20** 726 (1979)
46. M. H .Brodsky, R. S. Title, and K.Weiser, and G. D Pettit, *Phys. Rev. B* **1** 2632 (1970)

47. G K M Thuthupally, S G Tomlin J Phys. C 10 467 (1977)
48. J I Pankove *Optical Processes in semiconductors* pp.36, Dover publications Newyork.
49. J Tauc, R Grigorovici A Vancu *Phys. Stat. Sol.* **15** 627 (1966)
50. F Urbach *Phys. Rev.* **92** 1324 (1953)
51. J Tauc *Optical Porperties of Solids* edieted by F Abeles (North Holand) (1969)
52. H P D Lanyon *Phys.Rev* **130 134** (1963)
53. E A Davis and N F Mott *Philos. Mag.* 22 903 (1970)

Chapter 2

Experimental Techniques

Experimental Techniques

*In this chapter, different techniques used in the current work to grow a-Si thin films on glass, their crystallization, Structural and optical characterization are presented. The samples were prepared by thermal evaporation, ion beam sputtering and RF sputtering. The samples were characterized by a variety of structural and optical probes. Extended X ray absorption fine structure (**EXAFS**) was used to study the local structure of Ni atoms in a-Si matrix and these observations are complemented by X ray diffraction studies. Raman spectroscopy was employed to study the crystallization of amorphous Silicon thin films where crystallographic phase identification from **XRD** became difficult. It is shown that studies of optical properties are one among those viable techniques which are non destructive and non contact and with great experimental simplicity, allows one to study the electronic structure of the materials by **analyzing optical transmission** and **reflectivity** of a-Si thin films.*

2.1 Sample preparation

Samples prepared by RF sputtering were used for EXAFS measurements, while samples prepared by thermal evaporation and ion beam sputtering were used for studies of crystallization and the optical properties of a-Si thin films and metal doped Si films

2.1.1 Sample preparation for EXAFS measurements

RF sputtered a-Si thin films, deposited on crystalline quartz, containing 0.5% of Ni concentration are annealed at 600, 700 and 800 °C respectively. The reduced percentage of metal seed used in the present experiment is motivated, as explained previously, for understanding the atomic mechanism of MIC rather than for practical application where higher concentration of metal seed produce larger crystallites at lower annealing temperature. The films of about 2 μm thick were prepared by RF sputtering of a c-Si target together with small Ni pieces in an atmosphere of pure argon. Isochronal thermal annealing treatment of 15 minutes each was carried out at 600, 700 and 800 ^{o}C. The "as deposited" sample, whose substrate temperature was of the order of 200 ^{o}C does not evidence the typical peak of the presence of Si crystallites from Raman spectroscopy. Typical deposition conditions are tabulated below

Deposition Procedure	RF sputtering
Targets	Silicon(99.9%)+Ni(99%)
Substrate	Crystalline Quartz
Thickness	~2μm (Profilometer)
EXAFS Measurements	Fluorescence mode BM29 Beam line Esrf, Grenoble, France.
Samples	0.5% of nickel(600°C-800°C)

2.1.2 Samples for optical characterization

Thermal evaporation

Amorphous Silicon thin films were prepared by thermal evaporation on Borosilicate glass (BSG). Using tantalum dimple boats, via resistive evaporation 99.99% pure Silicon granules are evaporated on to the glass substrates held at a distance of 8 cm from the source. The distance between source and the substrate was constant for all the samples used for this thesis work. The effect of substrate temperature on the optical properties was studied in the case of pure a-Si thin films of different thickness. Typical conditions of the thermal evaporation are

- Pumping Unit : Diffusion pump + Rotary pump
- Base Vacuum : 3×10^{-6} Torr
- While evaporation : $2\text{-}5 \times 10^{-5}$ Torr
- Substrate to source distance : 8 cm
- Substrate Temparature : RT to 350 ^{o}C

Ion beam Sputtering

Amorphous Silicon thin films are grown directly on BSG substrates in a home built ion beam deposition system equipped with a TMP (turbo molecular pump). The deposition unit is incorporated with a Kaufmann type ion source (DC25 of Oxford Instruments, UK) capable of producing ion beams 2.5 cm in diameter with a beam energy up to 1.5 K eV. The ions are extracted and accelerated by applying a suitable potential to a dual-grid ion extraction system. The deposition chamber was evacuated to a base pressure of an order of 10^{-7} Torr before introducing argon gas into the system. The pressure during deposition was 5×10^{-4} Torr. The substrates were held at room temperature during deposition and mounted on a substrate holder which is 8 cm far from the substrate and source axis

2.2 EXAFS Measurements

2.2.1 EXAFS Measurements: Transmission and Fluorescence mode

A simple schematic diagram of the EXAFS experimental setup has been shown in figure 2.1. Major requirements are

- An x-ray source that can be tuned in energy,
- A monochromator to tune the energy
- High-quality detectors of x-ray intensity.

The x-ray source typically used is a synchrotron, which provides a full range of x-ray wavelengths, and a monochromator made from Silicon which uses Bragg diffraction to select a particular energy. The "white" X-ray beam is generated from a synchrotron and passed through a monochromator consisting of 2 Silicon crystals, usually of silicon. Radiation satisfying the Bragg condition $n\lambda=2d\sin\theta$ is reflected, where 'd' is the lattice spacing of the crystal plane. The desired X-ray energy is selected by varying 'θ'. The X-rays are polarized in the plane of the ring. ê is the electric-field polarization vector.

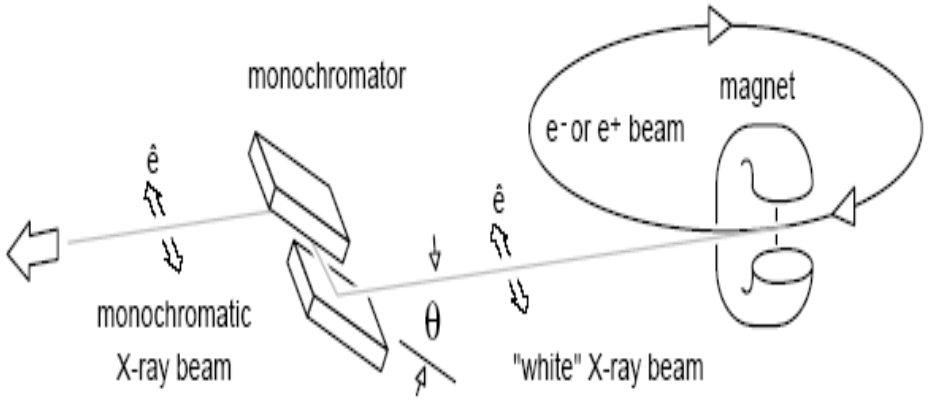

Figure 2.1 A schematic diagram of the generation of monochromatic x-ray beam. The energy resolution of the spectrometer will depend more on the monochromator. The best quality single crystal Silicon was used in monochromators. These monochromators should have high thermal stability and reproducibility. Energy resolutions of ~1 eV at 10 keV are readily achieved.

2.2.2 Transmission mode of detection

In a transmission mode, the intensity of the X-ray beam is measured before and after passing through a sample of thickness 'x', the absorbance (μ_t) can be calculated using the expression:

$$\mu_t x = -\ln\left(\frac{I_1}{I_o}\right) \ldots\ldots\ldots\ldots\ldots (2.1)$$

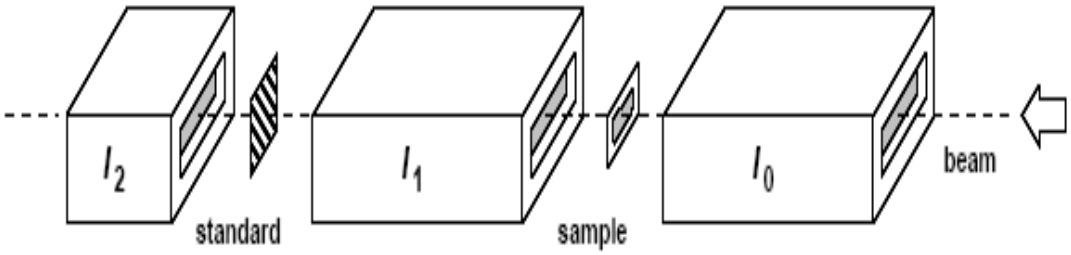

Figure 2.2. Typical apparatus for transmission XAFS experiment. *I*0, *I*1 and *I*2 are ionization detectors. A minimal experiment requires only *I*0 and *I*1. The addition of *I*2 permits the XAS of a standard such as a metal foil to be measured. This standard XAS is used for accurate energy calibration.

The intensity of the X-ray beam is measured using gas ionization detectors. A simple ion chamber consists of a parallel plate capacitor filled with an inert gas, and with a high voltage across it through which the x-ray beam passes. While passing through this chamber, X-rays will ionize the gas molecules in to positive ions and electrons, those ions are recorded as ion current which is proportional to the pressure of the gas filled-in and accordingly the intensity of the X-rays was calibrated. The X-ray beam passes through windows at each end of the chamber between two oppositely-charged plates. The (photo ion) current passing between the plates is proportional to the X-ray intensity. Figure 2.2 represents the detection setup for transmission mode EXAFS experiment. As shown in the figure 2.2, a third detector is often added to allow the

concurrent measurement of the XAFS from a standard. This standard spectrum is used to calibrate the energy scale using the position of features (transitions and inflection points) with known energy. In general sample thickness is a serious consideration in the transmission mode. The thickness of the sample should be such that $\mu x \approx 2.5$. Next to the thickness, the sample should be uniform and pinhole free.

2.2.3 Fluorescence mode of detection

For experiments where sample thickness becomes an issue or the extremely diluted samples not possible in transmission mode, the alternative way is "Fluorescence mode of detection". For thick samples or lower concentrations (down to the ppm level), monitoring the x-ray fluorescence is the preferred technique. However, as every method has its own advantages and disadvantages, in a fluorescence EXAFS measurement, the x-rays emitted from the sample will include the fluorescence line of interest and also the fluorescence lines from other elements in the sample and both elastically and inelastically (Compton) scattered x-rays. Figure 2.3 and 2.4 show typical fluorescence mode of detection with "Z-1" filter and Soller slits.

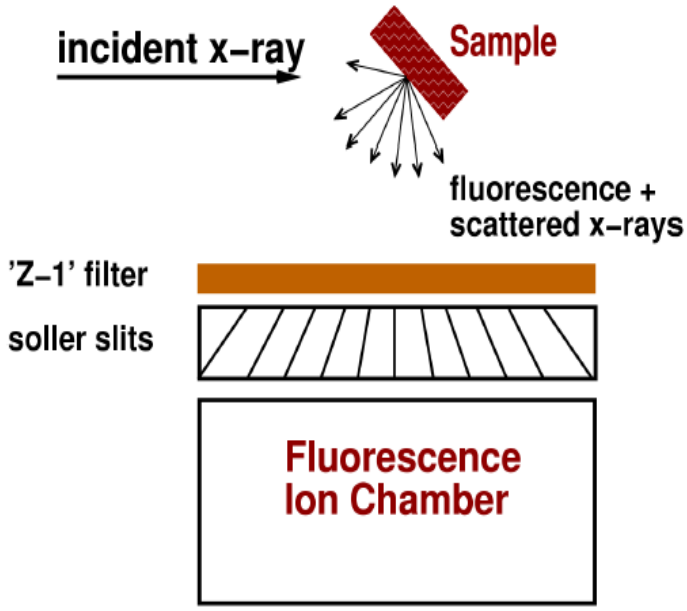

Figure 2.3 Schematic diagram of fluorescence detection.
The graphical illustrations shows "Z-1" filter and Soller slit arrangements.

If F is the intensity of the X-rays fluorescence, the absorption coefficient is given by:

$$\mu_F x = C\left(\frac{F}{I_o}\right) \qquad \text{..... (2.2)}$$

Where, C is approximately constant. C is normally neglected as it is eliminated when the EXAFS is extracted.

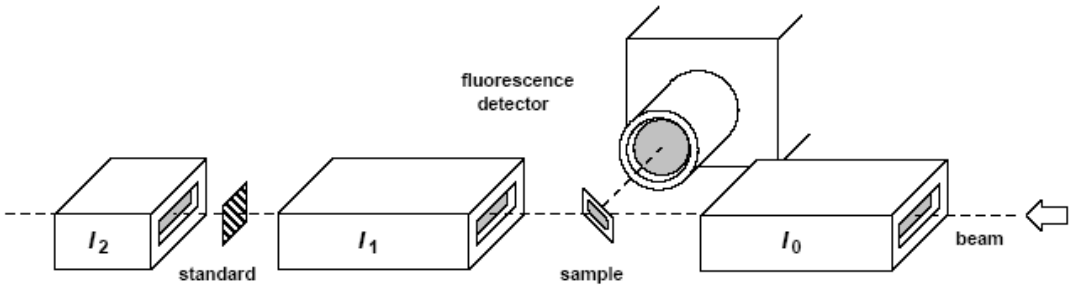

Figure 2.4 represents the detection apparatus for a fluorescence EXAFS experiment. The sample is commonly oriented at 45° to the beam and the fluorescence detector placed at 90°. Because the X-rays do not have to pass through the fluorescence detector, a solid state detector or an ionization detector filled with a gas of high X-ray cross-section to maximize detection is normally used.

As explained above, the principle aim of these experiments was to explore Ni environment in a-Si matrix. When these systems are annealed the coordination of Ni with Silicon will change and information about these parameters may help the understanding of metal induced crystallization in a-Si network. Thus, a-Si thin films of thickness 2μm were grown on quartz substrates, while maintaining the substrate temperature (T_s) constantly at 200 ^oC.

A series of EXAFS measurements were performed at the BM29 beam line of the ESRF facility. The EXAFS measurements were carried out at Ni K-edge (8333 eV).

For each sample on average 5 to 6 spectra were recorded to ensure the reproducibility of the data and hence to estimate the statistical error bars associated with the different structural parameters coming out from the modeling of EXAFS data.

Since the crystallization mechanism in Ni doped a-Si was believed to be due to the epitaxial growth of Si on the NiSi2 nodules as {111} plane of the NiSi2 offers overall lower free energy for Silicon to grow epitaxially, in the present study also the silicide formation was expected. To compare the sample EXAFS signal, the EXAFS of $NiSi_2$ powders were recorded in transmission mode. Apart from that Ni forms different phases with Silicon starting from Nickel rich Ni_3Si to the monosilicide NiSi. Among all these phases $NiSi_2$ is the stable phase. Hence, some reference compounds such as the metal rich phase Ni_2 Si and the Silicon rich $NiSi_2$, required for obtaining the experimental (or reconfirming check the validity of the theoretical models) scattering functions were also measured in the transmission mode.
The beam line details are as follows

- operational energy range: 4.5 keV to 74 keV.
- signal to noise ratio: 2×10^4
- beam dimensions: 1.0 mm to 0.2 mm

Monochromator:

In the beam line, depending upon the energy choice, any one or together of Si(111), Si(220), Si(311) and Si(511) crystal pairs can be used. For nickel K edge studies Si{111}crystal pairs were used to tune the X-ray energy, which have corresponding operational energy ranges of 4.5 keV to 24 keV. The intrinsic energy resolution was approximately 1×10^{-4} eV for the Si(111). This is well inside the core-hole lifetime broadening of the absorption edges within their operational energy ranges. The monochromator is equipped with a helium gas cooling system to minimize thermal perturbations to the energy of the monochromatic beam.

Detectors:

For transmission measurements ionization chambers were used (the typical setup was shown in figure 2.2). The ionization chamber consists of a parallel plate capacitor structure , and two electrodes were separated by a distance of 3 cm and operated at 1000 V. Depending on the operational energy range, nitrogen (low energy operation), argon (12 KeV to 30 KeV) were filled for detection. For fluorescence detection a 13-element germanium (Ge) fluorescence detector was used.

2.3 Raman scattering measurements

Raman Scattering measurements were carried out on Jobin-Yvon Confocal Micro Raman spectrometer. A schematic diagram of the Raman spectrometer is shown in the figure 2.5 and 2.6 below.

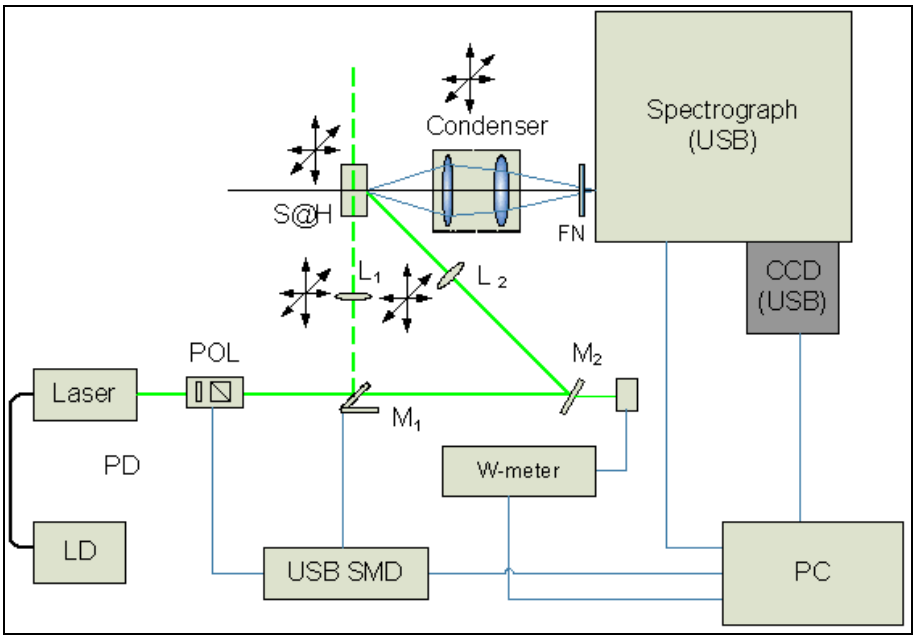

Figure 2.5 Schematic diagram of Raman Spectrometer

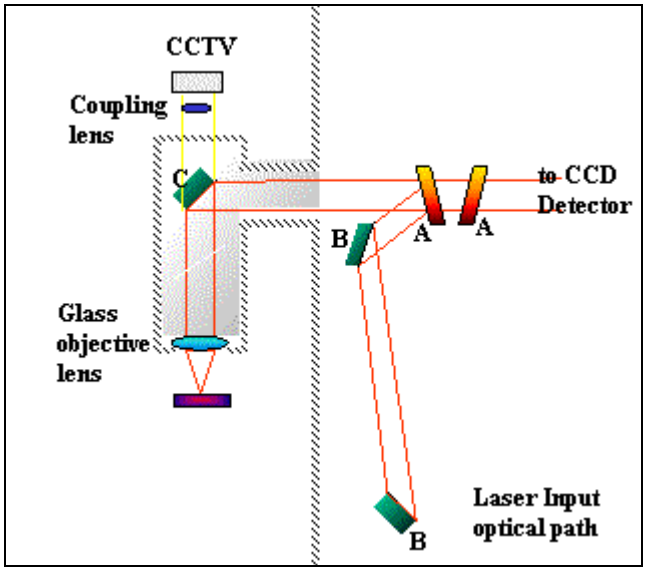

Figure 2.6 Schematic diagram of Raman Spectrometer equipped with Confocal objective arrangement

The Raman spectra were recorded in air using an argon ion laser in the back scattering geometry in a JY-ISA T64000 spectrometer equipped with an Olympus BX40 confocal microscope and 100X objective (1µm diameter focal spot size) with a liquid nitrogen cooled charge coupled device (CCD) detector. The spectral components coming from the amorphous and crystalline components are de-convoluted and related to Raman shifts and peak broadening. After correcting for the base line, a Voigt like function was used for curve fitting the Raman spectra. Care was taken to optimize the parameters of the He-Ne laser, so that it does not induce onset of crystallization in the sample. The phase content with in the samples was investigated in a spectral region 400 to 600 cm^{-1} with an irradiation time of 300 sec unless specified for particular measurement.

2.4 Optical spectral Transmission and specular Reflection measurements

The optical Spectrophotometric data of thin film samples investigated for this thesis work was collected in a dual-beam spectrophotometer (UV–Vis–NIR, model, Jasco V-570) having a resolution limit of ±0.2 nm and a sampling interval of 2 nm. Before and after annealing, the films were characterized for transmission and specular

reflectance in the wavelength range 190–2500 nm. All the samples were measured at the same incidence angle of 6.0 ^{o} ± 0.1 in order to avoid any fringe shift due to angular discrepancy. The transmitted intensities were measured to an accuracy of better than 0.3%.

Technical Specification of the Spectrometer

Optical system	Single monochromator 1200 lines/mm concave grating Modified Rowland mount
Light source	Deuterium lamp: 190 to 350 nm Halogen lamp: 330 to 2500 nm
Wavelength range	190 to 2500 nm
Detector	Silicon photodiode (S1337)
Photometric accuracy	±0.3 %T
Wavelength accuracy	±0.1 nm

The transmission spectrum of thin films was always recorded with respect to the air reference. In the case of specular reflectance, aluminum mirrors serve as reference.

2.5 Atomic Force Microscopy

In order to study the surface morphology of the a-Si thin films prepared by ion beam sputtering we have used Atomic Force Microscopy (AFM). We used Dynamic mode of operation (non-contact mode) where the probe tip will be set in vibration. The oscillation amplitude, phase and resonance frequency are modified by tip-sample interaction forces; these changes in oscillation with respect to the external reference oscillation provide information about the sample's characteristics. By analyzing a sample in stepwise fashion, the resolution limit set by diffraction is avoided. Current theories on the forces involved are based upon Born internuclear repulsion and Van

der Waals forces between atoms of the tip and the surface being scanned. The scan angle, set point (or operating force), feedback gains, and scan rate were optimized to obtain the clearest images possible without artifacts.

The machine and experimental specifications are as follows. The instrument is (SPA 400 of SII Inc. Japan) and settings for optimal imaging of silicon thin films were: 512 data samples per scan line; 26.5 Hertz; integral and proportional gain of approximately 1; and a set point of -1 to -2 volts and vibrational voltage of 1.97 V for dynamic mode of operation. No real-time filters are applied during data acquisition except for a plane fitting routine which removes image bow derived from the scanner moving out of the plane of the sample during scanning.

2.6 Optical Microscope

In the present thesis, the surface morphology of the a-Si thin films as-deposited and after annealing are studied under an optical microscope. The optical microscope was actually mounted on a confocal microscope from **Leica Micro systems** TCS SP2 ABOS type. The imaging has been carried out both in transmission mode and reflection mode depending on the requirement. Laser with wavelength λ=488 nm is the light source for all the imaging experiments.

Chapter 3

Data reduction and Analysis

Data reduction and Analysis

This chapter describes different procedures followed to analyze the experimental data collected in X ray absorption fine structure (EXAFS) and in optical absorption Spectroscopy. In EXAFS data analysis, the data reductions procedures, their merits and modeling the data using FEFF 6.0 code has been described in brief. The procedures to extract the optical constants of the films from single transmission spectra are introduced and emphasis has been placed on a computer code called PUMA through which the optical constants were extracted for all those films used in this thesis.

3.1 EXAFS Data Reduction

In this section different steps in the EXAFS data reduction are briefly described; taking a nickel foil's transmission data, recorded on the same machine (BM 29, ESRF, Grenoble, France.) where the further experiments were carried out as an example. The data reduction procedure is essentially same for both transmission mode of measurement and for fluorescence mode. First the raw data is reduced and that can be analyzed using the XAFS equation. The protocol to be followed is given in the following sections,

3.1.1 Conversion of measured data in to μ(E)

In EXAFS measurements the experimentally recorded data is intensity of the incident X-ray beam before and after passing through the sample. Thus, in transmission mode the total absorption coefficient μ(E) is given by

$$\mu(E)x = \ln\left(\frac{I_o}{I}\right) \qquad \text{……..…. (3.1)}$$

and in the case of fluorescence measurement, μ(E) is

$$\mu(E)x = \left(\frac{F}{I_o}\right) \qquad \text{…… (3.2)}$$

Where I_o, I and F are incident, transmitted, X-Ray fluorescence intensities respectively and X, is the sample thickness. Figure 3.1 shows the total absorption coefficient of nickel measured in transmittance mode and calculated using the equation Eq. (3.1).

3.1.2 Removing background

The interference (EXAFS) function χ(k) is defined as :

$$\chi(E) = \frac{\mu(E) - \mu_0(E)}{\mu_0(E)} \quad \text{..... (3.3)}$$

where μ_0 is the smooth background absorption coefficient due to the transition of interest; and μ is the observed absorbance. $\mu_0(E)$ is not known and is assumed as smooth part of the measured μ(E).

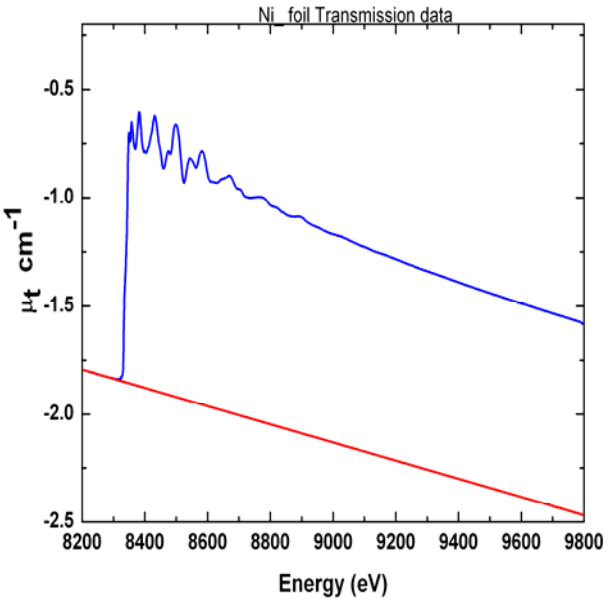

Figure 3.1. Shows the X-ray absorption coefficient measured at Ni K-edge, which arises from the absorption of a photon of energy above 8333 eV, promoting a 1s core electron to the continuum. This is measured in ESRF, Grenoble, France, on beam line BM 29.

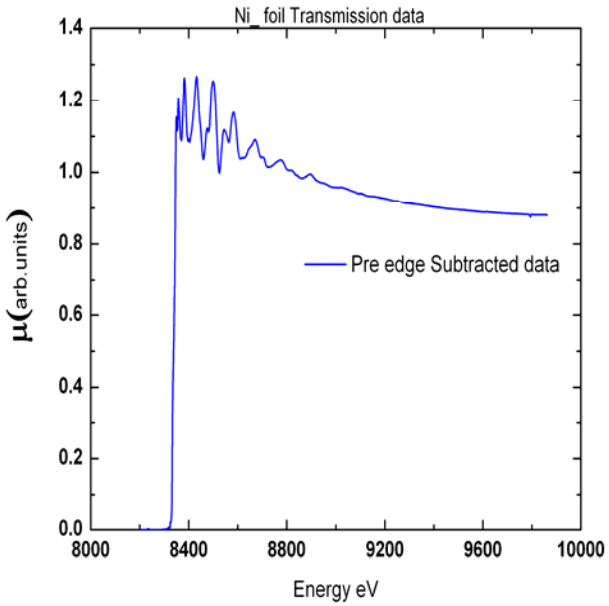

Figure 3.2 The Pre-edge subtracted transmission data of Ni foil. From 8200 eV to 8300 eV is fitted to linear function and extrapolated to the end of the data.

The background or "pre-edge" absorbance is estimated by fitting a polynomial function to the absorbance curve prior to the edge using a least-squares procedure and extrapolating to the end of the data. In the example of figure 3.1, the pre-edge curve was obtained by fitting a quadratic polynomial to the Ni absorbance between the energies 8200 eV and 8300 eV using EXTRA code[8].

3.1.3 Normalization

After subtraction of the pre-edge, the absorbance is scaled to an edge step of 1.0, so that the final EXAFS is relative to the edge (μ_0) as required by equation (3.3). The normalized data is shown in figure 3.3.

Ideally the $\mu_0(E)$ should be measured in the absence of neighbors but it is practically not possible. So, a hypothetical smooth background absorbance above the edge is estimated by fitting a polynomial spline function to the normalized absorbance. The polynomial spline curve consists of one or more polynomial segments. Adjacent segments are constrained to meet and to have the same first derivative, ensuring that the junctions are smooth. A least squares procedure is used to fit the spline curve to the normalized absorbance. The weight given to the data points is increased with

increasing energy as the fit has to be better at high energy due to the decreasing magnitude of the EXAFS oscillations.

The curve in figure 3.3 was obtained by fitting a 3-segment polynomial spline [9] to the normalized Ni absorbance. The polynomial coefficients were calculated to minimize $\Sigma[k3(\mu_{0normalized}(E)-\mu_{spline}(E))]^2$ for all points above $E0$, set arbitrarily to 9000 eV. To obtain the EXAFS, the difference between the normalized absorbance and the spline curve is divided by the normalized background absorbance due to the edge $\mu_{0\ normalized}$.

$\mu_{0\ normalized}$ is estimated using the expression:

$$\mu_{o(normalised)} = \lambda^3(C_a - C_b) - \lambda^4(D_a - D_b) \quad \text{..... (3.4)}$$

where λ is the X-ray wavelength and C_b and D_b and C_a and D_a are the Victoreen coefficients before and after the edge as tabulated in the International Tables for X-ray crystallography

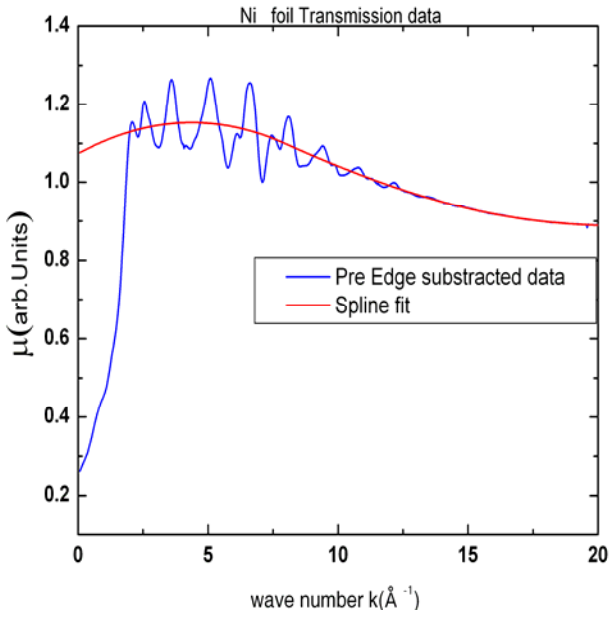

Figure 3.3 The subtracted pre-edge and the post edge is modeled to a smooth spline function in order to determine $\mu_0(E)$. The post edge is fitted to a spline of three polynomials of order [2, 2, 4] giving weights of 1,1,6 to the three polynomials .

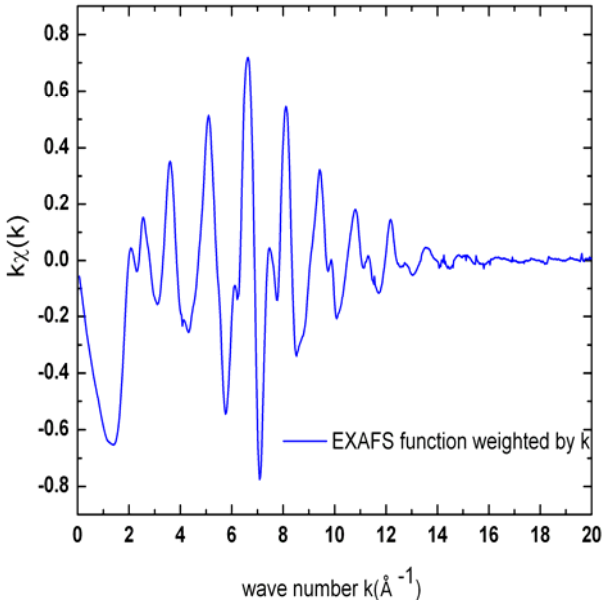

Figure 3.4 EXAFS signal weighted by k

The crucial step in EXAFS data reduction is the determination and removal of the post-edge background spline function. The isolated EXAFS signal appears as shown in figure 3.4. The k weighing is to give more weight to the high k range data which will have the low R(real) data. On Fourier transformation, low k data represents the high R where EXAFS is not sensitive and high k represents low R data, which is crucial for structural analysis. It should be noted that less than 2 $Å^{-1}$ in k space would result in less than 1 Å in R space, which is not a realistic distance between two atoms. The researcher has to be attentive towards this issue. EXAFS is sensitive up to 5Å rarely up to 10 Å, due to which the k- weighing scheme is more important.

Another crucial step and heart of the EXAFS analysis is the "Fourier transformation" [6, 7] and a few important points should be made about it. EXAFS signal of Nickel foil shown in figure 3.4. its Fourier transform is shown in Figure 3.5.Few significant points can be noted here. The first point to notice from Fig 3.5 is that four peaks are clearly visible – these correspond to the Ni-Ni and second nearest neighbor Ni-Ni distances in FCC Ni. Thus, the Fourier transformed EXAFS can be used to identify different coordination shells around the absorbing Ni atom and can be isolated.

Secondly, the first peak occurs at 2.2 Å , while the NI-Ni distance in FCC Ni is more like 2.43 Å

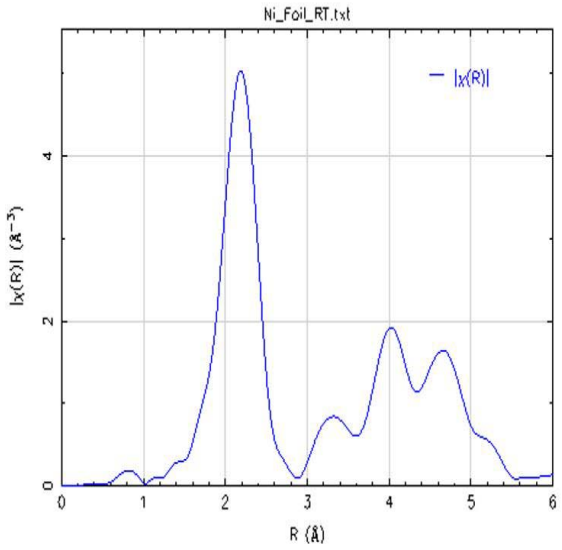

Figure 3.5 Forward Fourier transform of the EXAFS signal using the 2 to 14 $Å^{-1}$ of k-space data in figure 3.4

This is not an error, but is due to the scattering phase-shift, the term sin [2kR +δ] in the EXAFS equation. This phase-shift is typically 0.5 Å or so. The Fourier Transform is a complex function. It is common to display only the magnitude as shown on the left of fig 3.1.5. When modeling the EXAFS, it is important to keep in mind that it has both real and imaginary components.

3.1.4 k-weighing scheme

Oscillation amplitude will cease out as the photoelectron starts moving farther and farther. So at high k-space the amplitude will be small. In order to compensate that attenuation or loss of the EXAFS amplitude at high k values, $\chi(k)$ is often multiplied by some power of k to give $k^n\chi(k)$. This is equivalent to applying a weighing scheme which goes as k^n. This procedure is important in preventing the larger amplitude oscillations from dominating the smaller ones in the determination of inter atomic distances, which depend only on the frequencies and not the amplitude. In general, weighing schemes with n=1, 2 and 3 are in wide usage. Weighing schemes have a

significant effect on the peak heights and peak positions in the Fourier transformation as well as the fitting parameters in the curve fittings. It is therefore important to use the same weighing scheme when comparing unknowns with models.

3.1.5 EXAFS data modeling

In this section, the structural refinement of EXAFS data oscillations are described through an example of Nickel foil's transmission data. The Ni data shown in figure 3.1 will be analyzed here. Few structural details about Nickel are listed below.

Lattice constant :	3.5239 Å
Space group :	f m 3 m (face centered cubic lattice)
Distance first neighbor:	2.4395Å
Coordination:	12

Nickel occurs in the FCC structure, and is surrounded by 12 nickel atoms at a distance of 2.4395Å. Using this preliminary data a starting model can be selected and the scattering amplitude and phase shifts are calculated theoretically. The complete calculation is beyond the scope of this thesis. Here the FEFF 6.0 [10] program was used. The results of the FEFF calculation are stored in simple files containing the scattering factors and mean free-path for a given coordination shell.

These files will have the calculated scattering factors f(k) and phase shift $\delta(k)$ and also info about $\lambda(k)$. These data files can be loaded directly to computer programs to fit the EXAFS data for structural refinement. In this example and for this thesis work, IFEFFIT [11] EXAFS fitting program with ATHENA and ARTHEMIS [12] front ends were used. The details of these programs can be found in IFEFFIT manual. By allowing to vary the fitting parameters, which are usually R, N, and σ^2 and also allow E_0 best fit to the $\chi(k)$ can be attained. This fitting can be done in three different spaces. One in k-space, after Fourier transform in R-space and by back Fourier transform in Q-space. Each method has its own advantages. Working in R-space allows one to see clearly the coordination shells and can ignore the higher coordination shells. When analyzing the data in the R-space we should use complete complex EXAFS signal, not just the magnitude $|\chi(R)|$.

A typical fit to the first Ni-Ni shell is shown in Figure 3.6. The result from fit gives an Ni distance of R = 2.4877 ± 0.0048 Å, an Ni coordination number of N = 11.8 ± 1.8, a mean-square disorder of σ^2 = 0.006270 ± 0.005 $Å^2$, and a shift in E_O of = 7.86 ± 2.5 eV. The goodness of the fit for a unaided eye will be best to see in k-space. The k space fitting is shown in figure 3.6. The fit of the first shell in R space is shown in figure 3.7. It is evident that the higher shells have great effect on the in k-space fitting. However, we can add next shells also into the fit further. At this point the distance and number of second nearest neighbors can be known. The second Ni-Ni shell parameters R, N and σ^2 can be refined separately.

Fitting details

k-range	= 1.888 - 14.000
dk	= 2.000
k-window	= Kaiser-Bessel
k-weight	= 2
R-range	= 1.000 - 3.000
dR	= 0.100
R-window	= Kaiser-Bessel
fitting space	= R

R-factor for this data set = 0.00167

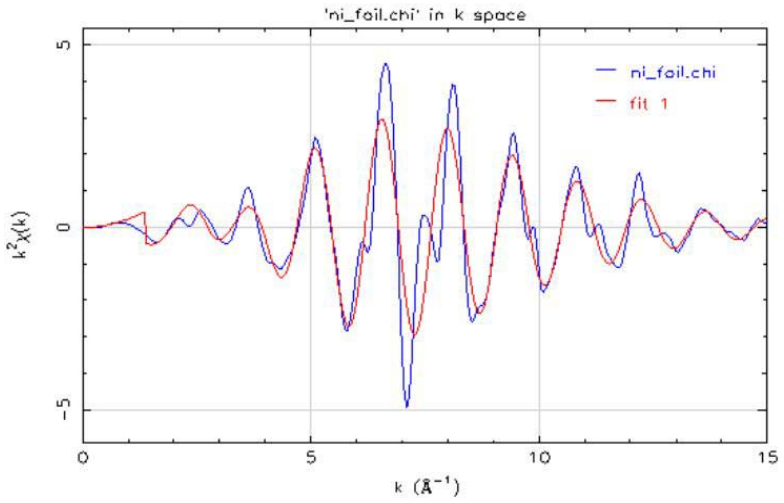

Figure 3.6 First shell fitting in k space .Ni-Ni first nearest neighbor is at 2.4877 Å

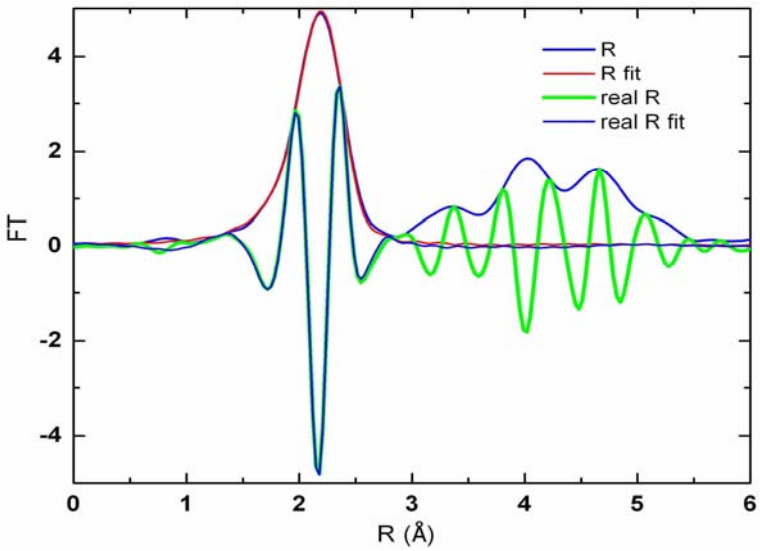

Figure 3.7 The first shell fitting in R space. Magnitude of R and real R and their fits are shown in figure.

For the second and third shells the R range is up to 4.5 Å. The second shell is at 3.557 ± 0.003 Å and coordinated with 5.5 ± 0.8 Ni atoms with $\sigma^2 = 0.0098$ Å^2. Figure 3.8 shows the second shell fitting in k space and 3.9 shows the fitting in R space

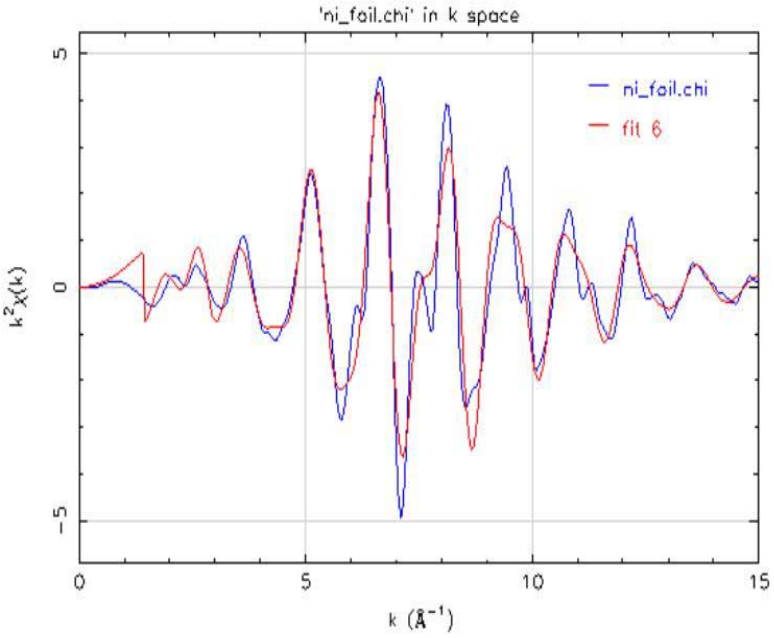

Figure 3.8 The first shell fitting in k-space .

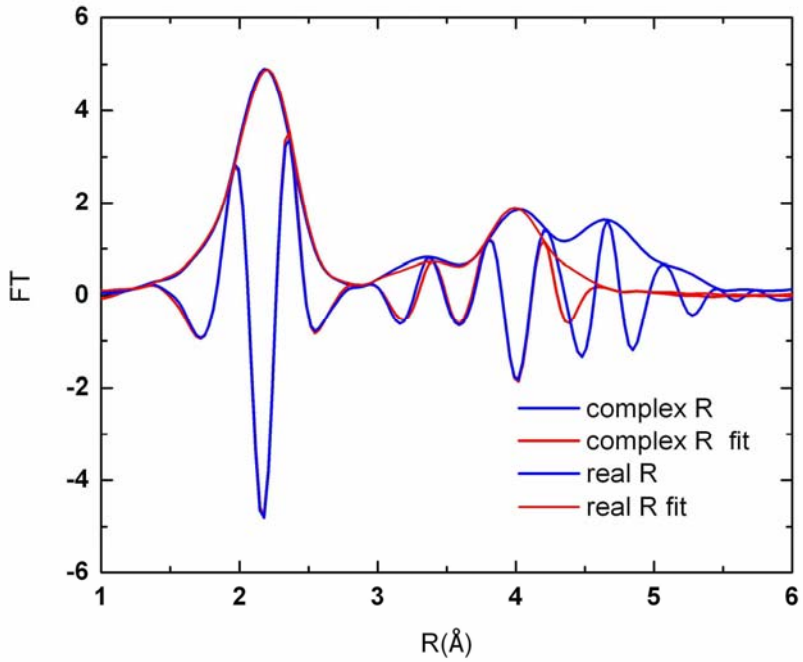

Figure3.9 The two shells fitting in R space. Magnitude of complex R and real R and their fits are shown in figure.

3.2 Optical Data Analysis

From a fundamental and a technological viewpoint, the knowledge of the spectral transmission behaviour of thin solid films is very important. It yields fundamental information on the dispersion behaviour of refractive index, optical absorption coefficient, optical energy gap (for semiconductors and insulators), defect levels, phonon and plasma frequencies and also microstructural evolution of the films. For the design and modelling of optical components and optical coatings such as interference filters the knowledge of refractive index is vital. The real and imaginary parts of the refractive index at each wavelength can be determined form a single optical transmission spectrum assuming that the thin film is isotropic, homogeneous and plane parallel to the substrate surface.

For the determination of optical constants usually optical spectral transmission curves are used. In this section an overview of the different methods of evaluating the transmission data to extract various optical constants is given with emphasis to methods, which have been used in this thesis work.

In general we can classify these into three different groups of methods

(1) Two independent optical measurements

(2) Fitting to dispersion relations

(3) Envelope method

Bringans, Denton *et al.* [13, 14] have suggested the combination of two independent measurements of near normal incidence transmittance and reflectance measurements. The method suffers from a few practical disadvantages; like measuring accurately the reflectance is always not possible. The guarantee of using the same selected area for both transmittance and reflectance measurements is small, which adds to the experimental errors. In the case of absorbing films where transmittance is nearly zero, we have to rely on the reflectivity only.

Another approach is to measure the transmittance of two thin films whose thickness are different [15] provided the refractive index is independent of thickness of the

film. Ellipsometric measurements have found vast applications in the microelectronics industry [16]. This technique is extremely sensitive to the surface of the film as the usual measurements are made in reflection mode. A very thin contamination of the surface will give completely erroneous optical constants. Later developments allowed the measurements to be performed in the transmission mode also [17]. Modeling of the Ellipsometric data yields most accurate optical properties of the materials. However, in this thesis work ellipsometry has not been employed so the analysis is limited to explain the analysis of spectrophotometric data.

3.2.1 Fitting with dispersion relations

i. Cauchy's equations

Cauchy's equations [18] are more empirical and best suited for transparent materials like SiO_2, Si_3N_4 and BK7 glass etc.

$$n(\lambda) = A_n + \frac{B_n}{\lambda^2} + \frac{C_n}{\lambda^4} + \ldots \qquad \ldots\ldots\ldots\ldots\ldots\ldots (3.5)$$

$$k(\lambda) = A_k + \frac{B_k}{\lambda^2} + \frac{C_k}{\lambda^4} + \ldots \qquad \ldots\ldots\ldots\ldots\ldots (3.6)$$

Where 'λ' is the wavelength, measured in μm, n and k are the refractive index and the extinction coefficient, function of wavelength. The A, B,C etc. are fitting parameters.

ii. Sellmeier equations

These equations [18] are generalization of Cauchy's equations and used for completely transparent materials (k=0), later extended to absorbing materials also with a new equation for 'k'.

$$n(\lambda) = \left(A_n + \frac{B_n \lambda^2}{\lambda^2 - C_n} \right)^{0.5} \qquad \ldots\ldots\ldots\ldots (3.7)$$

$$k(\lambda) = 0 \text{ or } k(\lambda) = \left[n(\lambda) \left(B_1 \lambda + \frac{B_2}{\lambda} + \frac{B_3}{\lambda^3} \right) \right]^{-1} \qquad \ldots\ldots\ldots\ldots (3.8)$$

Where A_n, B_n, C_n and B_1, B_2, B_3 are the fitting parameters.

iii. Lorentzian Oscillators

The optical spectra can also be modeled using oscillators [19]of the form given by

$$n^2 - k^2 = 1 + \frac{A\lambda^2}{\lambda^2 - \lambda_o + \frac{g\lambda^2}{\lambda^2 - \lambda_o}} \quad \text{..... (3.9)}$$

$$2nk = \frac{A\sqrt{g}\lambda^2}{\left(\lambda^2 - \lambda_o\right)^2 + g\lambda^2} \quad \text{.....(3.10)}$$

Where λ_o is the oscillator central wavelength, A the oscillator strength and g is the damping factor. These equations are consistent with the Kramers-Kronig equations where 'n' and 'k' are coupled.

iv. Forouhi–Bloomer dispersion relations

A more rigorous formulation was developed for determination of the complex refractive index of the semiconductors and dielectric materials [20, 21]. Essentially these equations are introduced to model the interband region of the materials.

$$k(E) = \sum_{i=1}^{q} \frac{A_i\left(E - E_g\right)^2}{E^2 - B_i E + C_i}$$

..... (3.11)

$$n(E) = n(\infty) + \sum_{i=1}^{q} \frac{B_{oi}E + C_{oi}}{E^2 - B_i E + C_i}$$

With

$$\left.\begin{aligned} B_{oi} &= \frac{A_i}{Q_i}\left(-\frac{Bi}{2} + E_g B_i - {E_g}^2 + C_i\right) \\ C_{oi} &= \frac{A_i}{Q_i}\left(\left({E^2}_g C_i\right)\frac{Bi}{2} + -2E_g C_i\right) \\ Q_i &= \frac{1}{2}\left(4C_i - {B_i}^2\right)^{\frac{1}{2}} \end{aligned}\right\} \quad \text{..... (3.12)}$$

Here, $n(\infty), A_i, B_i, C_i and E_g$ are the fitting parameters.

A correct set of n, k data will give a good fit to the transmission or reflectivity data. The simple relation between the refractive index, order of interference and thickness of the film enable to determine the correct set of n and k.

For the systems whose extinction coefficient is small, the transmission maxima and minima can be determined from the following two equations.

$$nd = \frac{m\lambda}{2} \qquad \text{.....(3.13)}$$

$$nd = \frac{(m+1)\lambda}{4} \qquad \text{..... (3.14)}$$

These equations will enable to calculate the refractive index accurately at one wavelength and simultaneously the thickness of the film. However this method is not suitable for very thin films where interference fringes are not present.

v. Unconstrained optimization (PUMA)

Point wise unconstrained optimization approach (PUMA) [22] assumes the following physical constraints, usually valid for semiconductors and insulators in the region of normal dispersion:

(1) $n(\lambda) \geq 1$ and $k(\lambda) \geq 0$ for all λ.

(2) $n(\lambda)$ and $k(\lambda)$ are decreasing functions of λ.

(3) $n(\lambda)$ is convex

(4) There is an inflexion point λ_{infl} such that $k(\lambda)$ is convex if $\lambda \geq \lambda_{infl}$ and concave if $\lambda < \lambda_{infl}$.

Then, a point wise optimization method can be developed for the least squares fitting of experimental transmission spectra against the spectra, calculated from $n(\lambda)$ and $k(\lambda)$, explicitly taking into account these constraints. A detailed mathematical treatment is given in the [22].

vi. Envelope method

Swanepoel developed this method in 1983[23]. The original idea was from Manifacier *et al* [24] in 1976.This method found its way into commercial thin film software [25,26]. The method is applicable to any transmission spectrum showing

appreciable interference fringes. From the transmission spectrum, envelopes around the transmission maxima and transmission minima are constructed. Then, the envelopes around the maxima and minima are considered as continuous varying functions of wavelength, T_M (λ) and T_m (λ), respectively. '*n'* and '*k'* can now be calculated from T_M and T_m at each wavelength. The envelope method is highly useful and very straightforward.

The transmission is defined as

$$T = \frac{Ax}{B - Cx\cos\phi + Dx^2} \qquad \text{……. (3.15)}$$

Where

$$A = 16n^2 s$$

$$B = (n+1)^3 (n+s)^2$$

$$C = 2(n^2 - 1)(n^2 - s^2)$$

$$D = (n-1)^3 (n - s^2)$$

$$\Phi = \frac{4\pi nd}{\lambda}$$

$$x = \exp(-\alpha d)$$

For such a system at the points of constructive and destructive interference the transmittance T_M and T_m, respectively are given by

$$T_M = \frac{Ax}{B - Cx + Dx^2} \qquad \text{…….(3.16)}$$

and

$$T_m = \frac{Ax}{B + Cx + Dx^2} \qquad \text{…….. (3.17)}$$

For simplicity it can be assumed that the transmission is continuously varying function of wavelength, which can be approximated by drawing the envelope around the spectrum, connecting all the maxima and minima

$$n = \left[N + \left(N^2 - n_s{}^2\right)^{1/2}\right]^{1/2} \qquad \text{..... (3.18)}$$

$$N = 2s\frac{T_M - T_m}{T_M T_m} + \frac{s^2 + 1}{2} \qquad \text{..... (3.19)}$$

And thickness of the thin film can be determined by

$$d = \frac{\lambda_1 \lambda_2}{2\left(n_1 \lambda_2 - n_2 \lambda_1\right)} \qquad \text{..... (3.20)}$$

A few pitfalls in Envelope method:

- There is no straight forward way to construct the envelopes between interference extremes. Usually, they are constructed using parabolic interpolation, but this is in fact an arbitrary choice.

- The envelopes should ideally be constructed from the tangent points touching the transmission curve, not from the interference extremes: it is easy to see that, especially in a region where the transmission is changing fast, connecting the extremes will yield T_M (λ) and T_m (λ) curves that are actually too close to each other. More recently, efforts have been undertaken to increase the accuracy of the envelope determination.

- At lower film thickness, the interference extremes are spaced further apart and interpolation between these extremes becomes more difficult and the accuracy of the method decreases with decreasing film thickness

- The method fails, when the thin film become more absorbing and the interference fringes are not visible and T_M (λ) and T_m (λ) curves coincide with each other.

The above two methods: unconstrained optimization (PUMA) and envelope method have been extensively used to model the optical transmission spectra. We have extracted the n and k from full profile fitting of the optical transmission spectra. An example transmission spectra and its fitting are shown the figure 3.10 below.

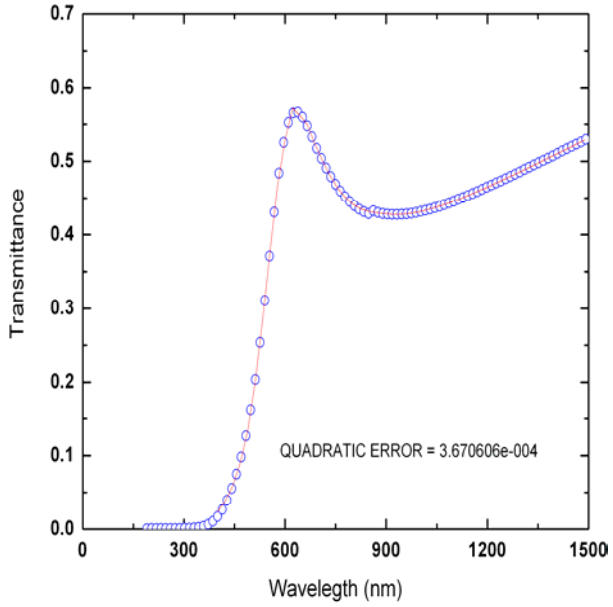

Figure 3.10 Puma fit for a75 nm thick a-Si thin film

Experimental data (*open circles*) and the PUMA fit (*solid line*)

References:

1. R Kronig. deL. Z. *Phys*, **70**,317,(1931)
2. R Kronig. deL. Z. *Phys*, **75**,468, ; ibid **76** 468 (1932)
3. E. A. Stern, D.E. Sayers, and F. W. Lytle, *Phys. Rev*. B **11**, 4836 (1975).
4. E. A. Stern, *Phys. Rev*. B **10**, 3027 (1974).
5. C A Ashely, S Doniah, *Phys. Rev* B, **11,** 1275 (1975).
6. L Lee P, J. B Prendy, *Phys. Rev*. B **11**, 2795 (1975).
7. L Lee P. , G Beni. *Phys. Rev*. B **15**, 2862 (1977).
8. P Fornasini, F Rocca. *EXTRA* code for EXAFS analysis, University of Trento, 1998.
9. J H Ahlberg E N Nilson JL Walsh "*The Theory of the Splines and Applications*," Acadamic, New York, 1967.
10. J.J. Rehr & R.C. Albers, *Rev. Mod. Phys.* **72**, 621,(2000)
11. M. Newville, *J. Synchrotron Rad*.. **8,** 322, (2001)
12. B. Ravel & M. Newville *J. Synchrotron Rad*., **12,**537, (2005).
13. R D Bringans *J. Phys. D: Appl. Phys.* **10** 1855 (1977)
14. R E Denton, R D Campbell and S G Tomlin *J. Phys. D: Appl. Phys.* **5** 852 (1972)
15. R A Hazelwood *Thin Solid Films* **6** 329 (1970)
16. E A Irene *Thin Solid Films* 233 **96** (1993)
17. G Bader, P V Ashrit and V V Truong *Appl. Opt*. **37** 1146 (1998)
18. F A Jenkins and H E White *Fundamentals of Optics* (Auckland: McGraw-Hill) pp 482 (1981)
19. E Hecht *Optics* 2nd edn (Reading MA: Addison-Wesley) pp 61 (1990)
20. A R Forouhi and I Bloomer *Phys. Rev. B* **34** 7018 (1986)
21. A R Forouhi and I Bloomer *Phys. Rev. B* **38** 1865 (1988)
22. E.G. Birgin, I. Chambouleyron, and J. M. Martínez, *Journal of Computational Physics* **151** 862. (1999)
23. R Swanepoel *J. Phys. E: Sci. Instrum.* **16** 1214 (1983)
24. J C Manifacier, J Gasiot and J P Fillard *J. Phys. E: Sci.Instrum*. **9** 1002 (1976)

25. Essential MacLeod, Thin Film Center Inc., Tucson, AZ, USA,http://www.thinfilmcenter.com/
26. FilmStar, FTG Software Associates, Princeton, NJ, USA, http://www.ftgsoftware.com/design.htm

Referred Books:

1. *Elements of Modern X-ray Physics*, J. Als-Nielsen and D. McMorrow JohnWiley & Sons, 2001.
2. *Xray Absorption: Principles, Applications, Techniques of EXAFS, SEXAFS, and XANES, in Chemical Analysis* 92, D. C. Koningsberger and R. Prins, ed., John Wiley & Sons, 1988.
3. *EXAFS : Basic Pricnciples and Data Anlaysis* by Boon K Teo, Springer,1986

Chapter 4

Results and Discussion

EXAFS Measurements on Ni doped a-Si thin films

EXAFS is a good tool to study the local structure and the dynamic behavior of the matter. The present study is aimed at understanding the Nickel (Ni) bonding behaviour in an amorphous Silicon (a-Si) matrix and consequently the nickel induced crystallization of a-Si. While exploiting the full potential of EXAFS, the metal (in this case Ni) environment inside an amorphous matrix has been determined. The knowledge of bond making and breaking nature of Ni inside the Silicon matrix will help in understanding the role of Ni, in rearranging the a-Si network after thermal annealing. Facts about the Ni environment and its distinctive bonding with silicon in as prepared sample and samples annealed at different temperatures are presented in this chapter in conjunction with Raman Spectroscopy.

4.1 EXAFS Measurements on Ni doped a-Si thin films

X-ray absorption coefficient $\mu(E)$, was measured at Ni *K*-edge (8333 eV), in fluorescence mode for the thin film samples with 45^{O} of X ray beam incident angle and the fluorescence yield was recorded on a liquid nitrogen cooled thirteen-element Ge detector. The $\mu(E)$ for reference compounds (Ni foil, Ni_2Si and $NiSi_2$ powders) was measured in transmission mode. The radiation source was the European Synchrotron Radiation Facility (ESRF); experimental beam line was BM29 with an average storage ring current of 180 mA. The EXAFS spectrum in this work represents the average of 5-6 repeated scans.

4.1.1 Data Reduction

The aligned and pre-edge subtracted X-ray absorption spectra of amorphous Silicon (a-Si) thin film samples with at wt. % of 0.5 of Ni are shown in figure 4.1.1.

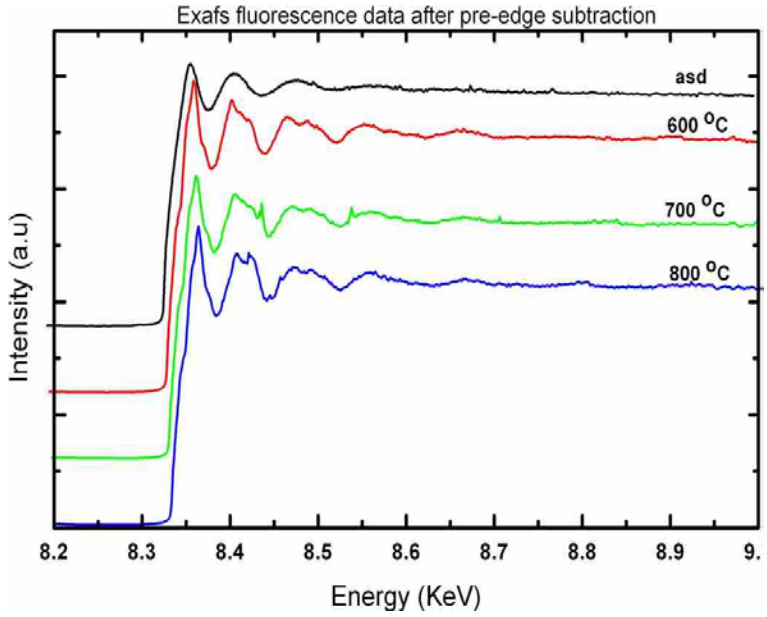

Figure 4.1.1 Pre edge subtracted X-ray absorption data of a-Si thin films doped with constant Nickel concentration of at .W 0.5 % and annealed at three different temperatures.

4.1.2 X-ray absorption near edge structure (XANES)

In the X-ray absorption spectrum, X ray absorption near edge structure (XANES) region occupies a 50 eV span from the edge jump. The interpretation of XANES is complicated by the fact that there is no simple analytic description of XANES. The main difficulty is that the EXAFS equation breaks down at low-k, due to the 1/k term and the increase in the mean free path at very low-k. In spite of the difficulty in interpretation of XANES spectra, chemical information like formal valence and coordination environment, often used as fingerprints of absorbing species. From a direct comparison between XANES spectra of unknown samples and reference some qualitative considerations can be drawn.

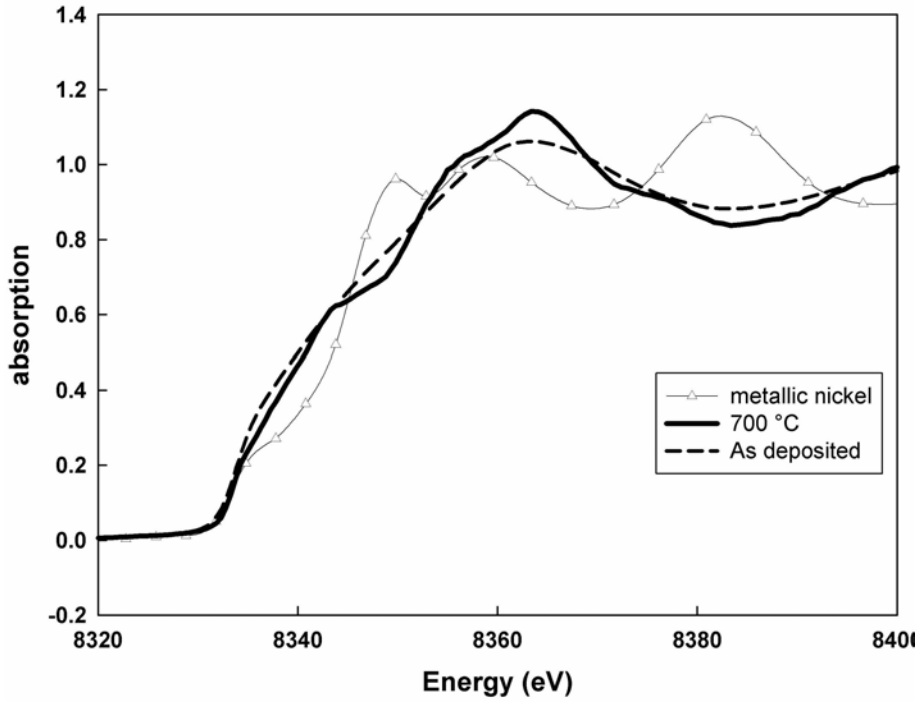

Figure 4.1.2 XANES measured at the Ni *K*-edge (8333 eV) showing the Ni absorption edge in the three different samples of the AD sample, crystallised (MIC induced) sample and the nickel foil due to various chemical and structural environment.

In figure 4.1.2 the XANES spectra at the Ni edge of the as- deposited sample (*dashed curve*) and the crystallized sample annealed at 700°C annealed (*solid curve*) are

compared with the XANES of the Ni foil's X-ray absorption. The environment around the Ni atom, in the three samples was seems to be different. In the Ni foil, Ni will always see only Ni atoms around, whereas in the as-deposited sample and in 700 °C annealed sample the Ni environment is different. From the strong difference between the spectra of Ni foil and the 700 °C annealed sample, it can be inferred that in the thin films case Ni have no Ni neighbours. This fact can be interpreted as neither in as-deposited and in annealed sample Ni clustering was ruled out. However, XANES spectra show no such behavior of Ni between in the a-Si thin films sample with 0.5 % of Ni. And the high diffusivity of Ni in the order of 10^{-4} cm^2/sec in c-Si and is expected not to be much lower in a-Si [1] Ni quickly bonds to silicon atoms instead of clustering (metal clustering).

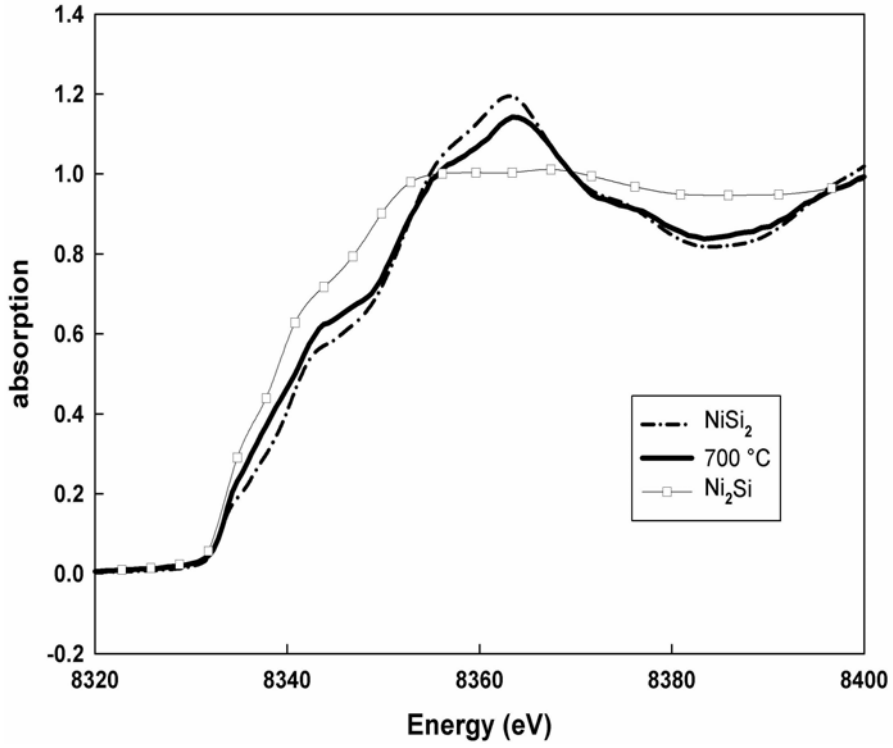

Figure 4.1.3 XANES of crystalline sample annealed at 700 °C compared with two crystalline reference samples: Ni_2Si and $NiSi_2$.

In figure 4.1.3 the XANES spectra of the crystallised sample at 700 °C (solid curve) is compared with the two reference compounds: $NiSi_2$ and Ni_2Si. It is evident that the $NiSi_2$ spectrum is closer to the spectrum of the thin film sample than the Ni_2Si. This

could be primary evidence for the fact that structure around Ni atoms in the silicon host films is more likely to be nickel disilicide ($NiSi_2$).

4.1.3 EXAFS spectra

Using AUTOBK algorithm [2] the EXAFS signal were extracted from raw data. The following three steps were common to extract EXAFS signal for the measure X-ray absorption.

- Determine the edge energy, E_O
- Determine the normalization constant, $\Delta\mu_o(E)$
- Determine the post-edge background function, $\mu_o(E)$

A piecewise polynomial was used to approximate the, $\mu_o(E)$, the atomic-like absorption coefficient past the edge, and $\Delta\mu_o(E)$ is the jump in the absorption coefficient at the edge step. After back-ground subtraction and normalization of the "wiggles" in the $\mu(E)$, the measured absorption data, is plotted in figure 4.1.4. From figure 4.1.4 it is evident that EXAFS of the samples gradually changed with annealing temperature while keeping the annealing time, constant at 15 minutes constant. The changes signify the local structural variation and structural ordering around Ni. Nickel, while reacting with Silicon forms different crystallographic phases, starting from monosilicide (NiSi) to metal rich phase Ni_3Si forms. [3]. As metal induced crystallization was believed to be an epitaxy on the (111) facet of the $NiSi_2$ nodules, in the thin film samples, where Si is crystalline, some cubic phase of nickel silicide is expected. Among all different nickel silicides, $NiSi_2$ and Ni_3Si are cubic in nature. In the light of the above considerations (about forming a disilicide), we have measured X-ray absorption coefficient of two bulk nickel silicides Nickel disilicide ($NiSi_2$) and the nickel rich phase Ni_2Si.

These samples were bulk powders, and X-ray absorption coefficient was measured in transmission mode.

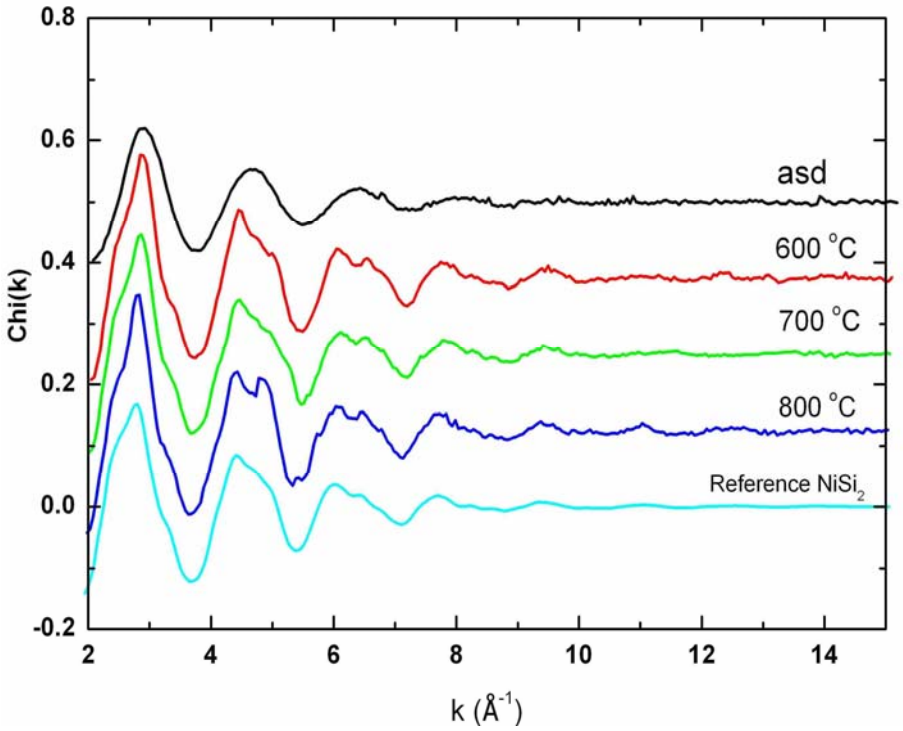

Figure 4.1.4 After background subtraction the EXAFS signals χ(k) of as-deposited (asd), 600, 700 and 800 ^{o}C annealed samples, along with reference sample $NiSi_2$ are shown.

For the as-deposited sample the EXAFS signals were smooth and amplitude of oscillations were small, whereas the 700 ^{o}C annealed sample shows sharp features in the oscillations. The sharpness in the fine structure was a distinct characteristic of long range order or in other words the crystallanity of the sample. Comparing the EXAFS spectra of the 700 ^{o}C sample with $NiSi_2$ bulk reference sample reveals similarity in the shape and amplitude of oscillations, which suggests that, the local environment around the Nickel in sample 700 ^{o}C annealed was similar to that of the local environment of Ni in $NiSi_2$ bulk sample.

The Ni K-edge EXAFS oscillations are Fourier Transformed to determine the radial distances of the Ni neighbors. The Fourier transformation (FT) details are listed below

- k-range for FT : 2 -- 10Å^{-1}
- Window : Kaiser-Bessel; dk = 2
- R range : 0 - 6 Å
- k-weighing : 2

As mentioned earlier after Fourier transformation, EXAFS oscillations represent the neighbouring atoms distances and number in the form of a one dimensional radial distribution function (RDF). For the first observation to such a RDF of $NiSi_2$ which is shown in figure 4.1.5, two peaks are clearly visible for the $NiSi_2$ bulk sample. These peaks correspond to the Ni-Si distance, the first peak is related to the nearest neighbor of the absorbing atom, Ni, (first coordination shell) and the second peak is comprised of two distance, Ni-Ni and Ni-Si. Thus, the Fourier transformed EXAFS can be used to isolate and identify different coordination spheres around the absorbing Ni atom. The next observation to notice is that the first peak occurs at approx. 1.8 Å, while the Ni-Si distance in $NiSi_2$ was more like 2.34 Å. This was not an error, but due to the fact that scattering phase-shift, in the EXAFS goes as sin (2kR + δ). This phase-shift will be typically about 0.5 Å. Even though the Fourier transform was a complex function it is common to display only the magnitude $|\chi(R)|$ as shown in the figure 4.1.5. When modeling the EXAFS, it is important that the signal have both real and imaginary components. The FT of all four samples is shown in figure 4.1.6.

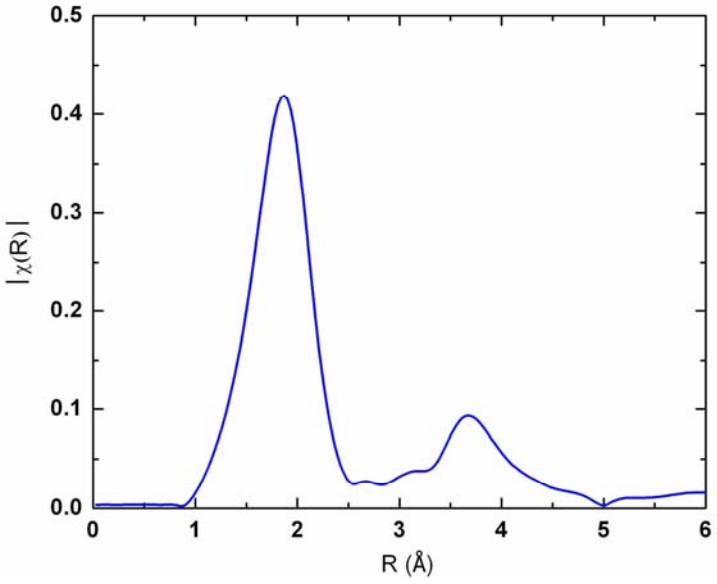

Figure 4.1.5 The magnitude of $|\chi(R)|$ of $NiSi_2$ bulk sample

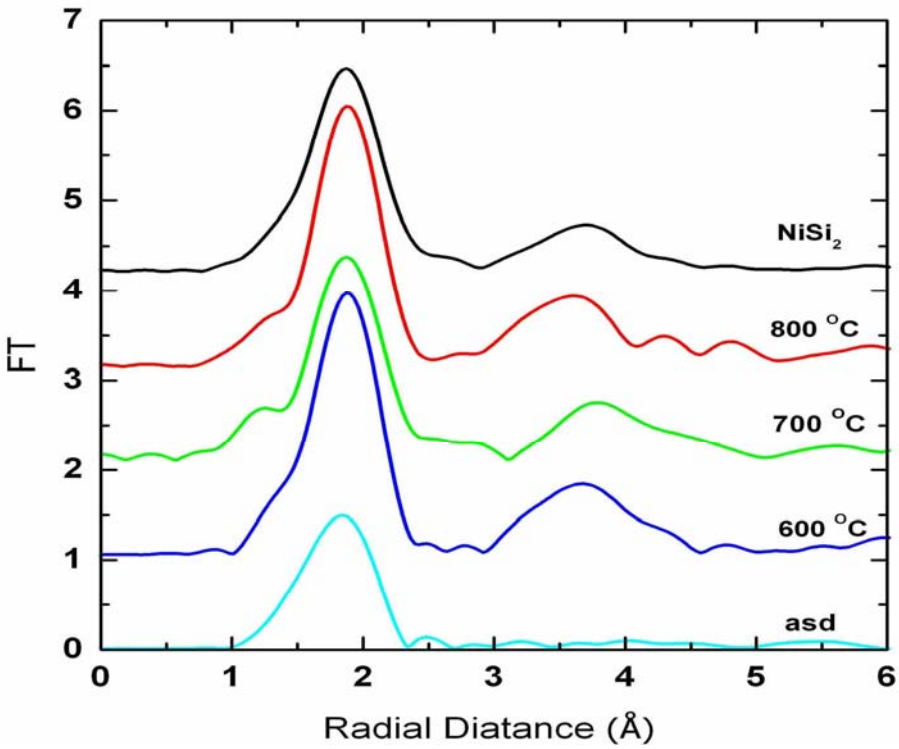

Figure 4.1.6 The direct Fourier transforms of the EXAFS spectra shown in figure 4.1.5 weighted by k^2: the spectra are vertically shifted for clarity.

FT of the EXAFS of thin film samples, while comparing with $NiSi_2$ bulk, shows that except in the as-deposited sample, after 15 minutes of annealing, the local structure

evolved around the nickel atom as similar to $NiSi_2$ structure. The as-deposited sample shows only one peak that belongs to first nearest neighbour Ni-Si distance at 2.31 Å and this peak shift towards right of higher values of R , as the bond length of Ni-Si relaxes after annealing and reaches a value of 2.33 ± 0.02 Å with a bulk Ni-Si bond length of 2.3409 Å. The peak height and width in the FT are related to the effective coordination number and degree of disorder respectively; these structural details and their evolution along with annealing temperature for all four samples will be discussed in consecutive sections.

4.1.4 EXAFS modeling: Starting model

Usually, in EXAFS structural refinement a crystallography based structural model is adopted to have starting guess values of R, the radial distance, N, the effective coordination number and σ^2, the Debye-Waller factor. Preliminary conclusion made from XANES and EXAFS suggest that the nickel di-silicide could be a viable structural model for this EXAFS signal analysis. However, other phases of nickle silicides were also considered as starting models, as mentioned in XANES part. The amplitude functions calculated from FEFF code for Ni_2Si and $NiSi_2$ compared with Ni amplitude functions are plotted in figure 4.1.7. The differences in the amplitude functions were due to the diverse amplitudes of back scattering efficiency of the neighbours or the pairs of atoms involved in. Ni-Ni pair in Ni foil and the Ni-Si pair in Ni_2Si and $NiSi_2$. Thus, these calculated amplitudes were compared to eliminate the possible number of starting models. The Nickel disilicide ($NiSi_2$) has the cubic CaF_2 structure represented by the space group F m 3 m with lattice parameters a=b=c=5.406 Å [4] and a FCC Bravais lattice lattice symmetry with 8 silicon atoms around Ni as its first nearest neighbours, at a distance of 2.34 Å. The schematic structure is shown in figure 4.1.8.

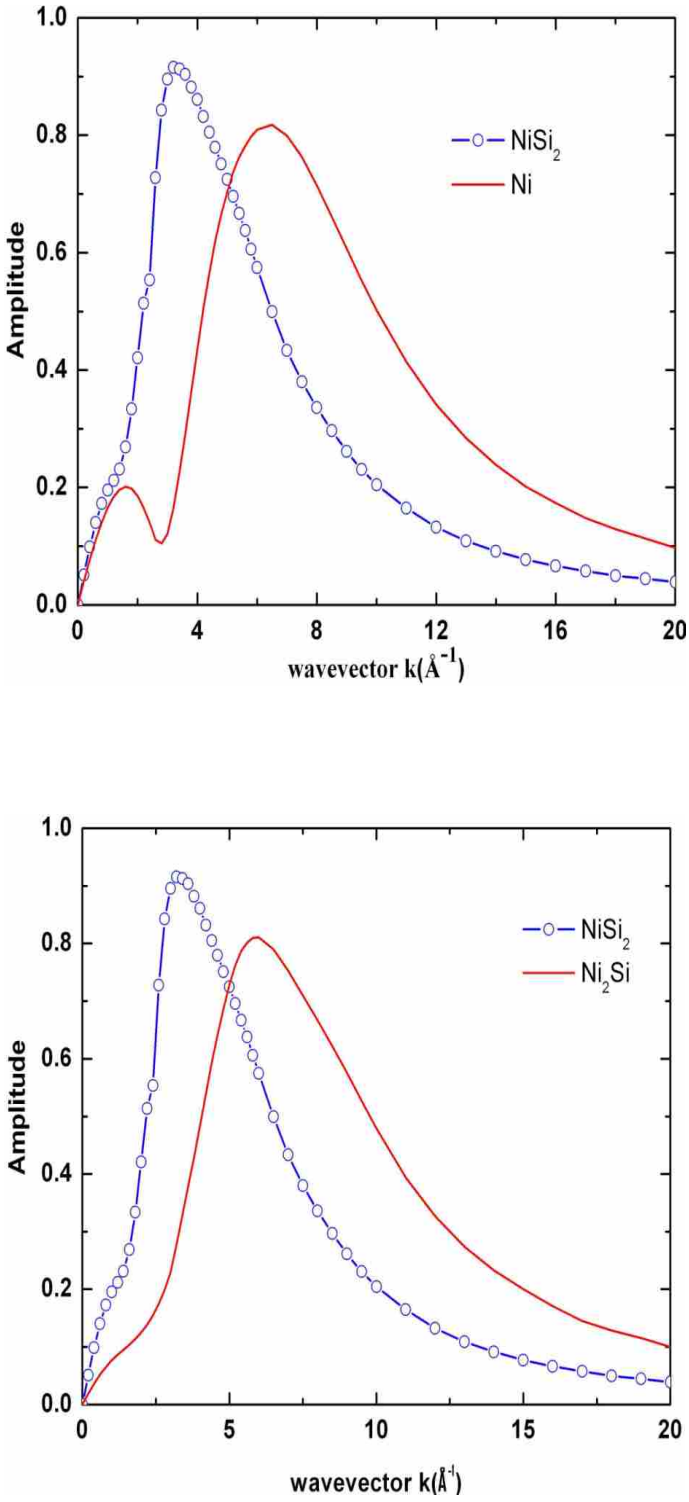

Figure 4.1.7 Back scattering amplitudes for
Top: Ni-Ni in Ni foil , Ni-Si pairs in $NiSi_2$,
Bottom: Ni-Si pairs in and Ni_2Si and $NiSi_2$

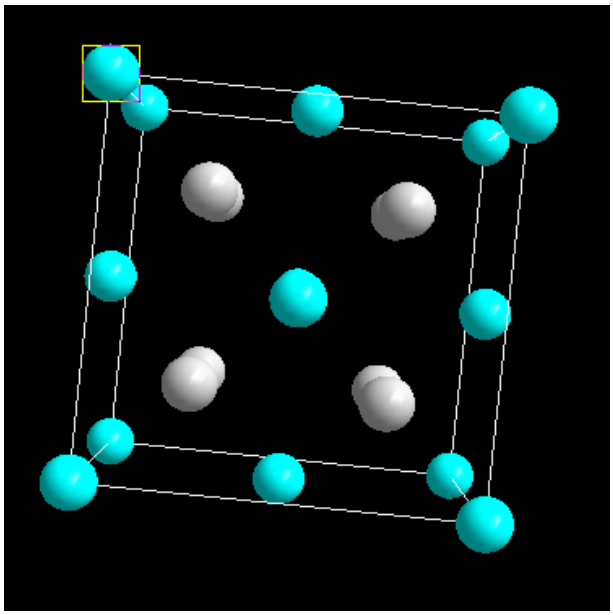

Neighbors of Ni

Ni-Si	8	2.3409 Å
Ni-Ni	12	3.8226 Å
Ni-Si	24	4.4824 Å

Green: Nickel
Grey : Silicon

Figure 4.1.8 Schematic diagram of $NiSi_2$ crystal structure and structural details of $NiSi_2$

The X-ray photon energy was tuned such that it ejects 1s (K shell) electron of Ni (8333 eV). Once the photoelectron starts as a spherical wave from the Nickel atom and travels over few angstroms of distances it encounters the nearest neighbours and comes back to the absorbing Ni atom after being back scattered from neighbouring atoms, brings the information about backscatterers. For a nickel atom in $NiSi_2$, nickel is bonded to 8 silicon atoms as shown in figure 4.1.9. In the figure 4.1.10 the EXAFS view of $NiSi_2$ is depicted.

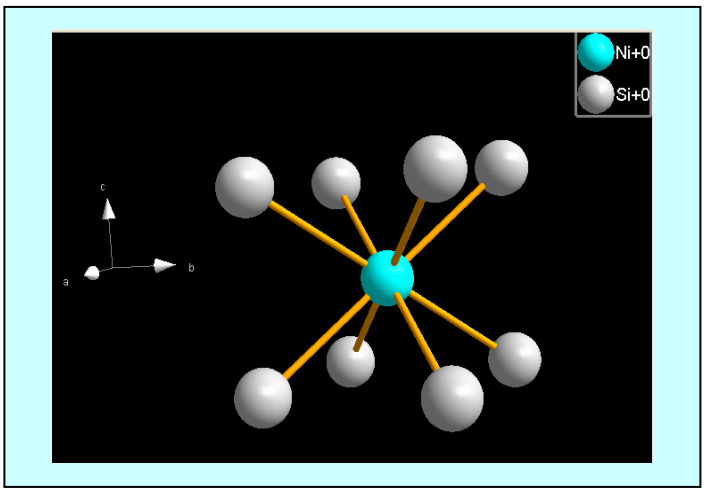

Figure 4.1.9 Ni is co-ordinate with 8 silicon atoms
at a distance of 2.3409 Å

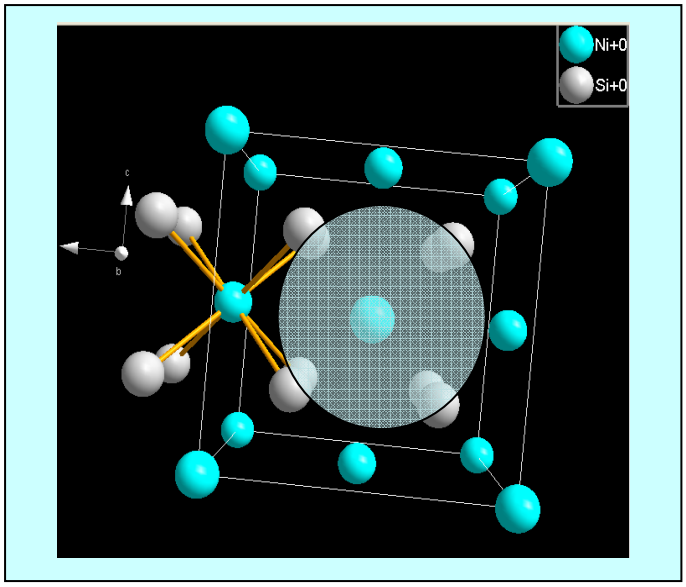

Ni-neighbor	**Distance Å**	**No. of neighbor**
Si	2.3409	8

Figure 4.1.10 The first nearest neighbours of Ni in $NiSi_2$ crystal structure
An EXAFS view of the so called "first shell"

4.1.5 Fitting strategy

The structural parameters Radial distance R, Effective coordination number, N and Debye-Waller factor, σ^2 were determined after curve fitting the EXAFS data using parameterized EXAFS equation. The EXAFS equation was

$$\chi(k) = \sum \frac{N_j f_j(k) e^{-2k^2 \sigma_j^{\,2}}}{kR_j^{\,2}} \sin\left[2kR_j + \delta_j(k)\right] \quad \text{..... (4.1.1)}$$

As described in section 1.2.1 and in section 1.2.6 the experimental data is modeled by using the Phase and Amplitudes of the scattering atomic species around the absorbing atom. These Phase and Amplitudes can be derived from standard sample or can be calculated theoretically using computer codes like FEFF 6.0 code. Based on earlier results [5] the samples are expected to contain Nickel di-silicide ($NiSi_2$) and best fit obtained with $NiSi_2$ structure, which will be presented in the preceding further sections.

Following the scenario, we have calculated the amplitudes and phases theoretically using FEFF 6.0; For curve fitting, a computer program called IFEFFIT was used, which takes the FEFF 6.0 calculated data as input and fits the EXAFS data to determine the local structural parameters around the absorbing atom.

Before going in to the details of model it is pertinent to briefly describe FEFF code. The FEFF code speaks in terms of scattering paths. The Scattering paths are represented by circles connected by arcing lines, as those shown Figure 4.1.11. They mean to suggest the path taken by a photoelectron as it propagates from the central atom to neighboring atom(s), scatters from the neighbor(s), and propagates back to the central atom.

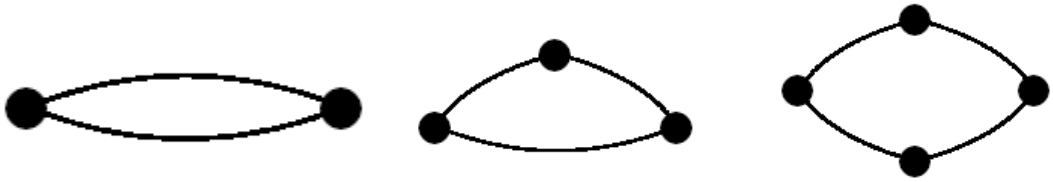

(a)Single scattering (b) double scattering (c) Triple scattering

Figure 4.1.11 Different scattering paths considered by FEFF while calculating the phase and amplitudes. Multiple scattering paths were not shown here.

When considering single scattering paths, the concepts of "paths" and "shells" are very similar. In the rest of the thesis we have used the term "shell".

To evaluate the total structure function $\chi(k)$, values for the various path parameters in the EXAFS equation (ΔR, σ^2, (N, S_o^2), E_o must be evaluated for each path.

ΔR = change in half-path length

σ^2 = Debye-Waller factor

N = Co-ordination number

S_o^2 = path amplitude (passive electron reduction factor)

E_o = energy reference shift for the path

In IFEFFIT the coordination number was held constant (adopted form the crystallography) and path amplitude has been refined. While refining this parameter we have to be more confident about the experimental errors in data collection. Otherwise amplitude reduction in the EXAFS signal may be because of many other factors like detector response sample inhomogeneity and so on. To avoid these problems we have determined the amplitude factor of the standard bulk sample and that value we have used for the thin films as amplitude factor is chemically transferable. Accordingly in FEFFIT the math expression has been modified.

$N*So^2$ * amp is the original expression that has been modified as 1 * So^2* CN1 where So^2 was set to a constant value of 0.85 and the coordination value N =1 and the new parameter defined as CN1 gives the coordination number directly.

As described above, the figure 4.1.6 shows the FT of the EXAFS signals. The bottom most curve belongs to as-deposited sample and is compared with the rest of the spectra. The as-deposited sample has only one maximum of Ni-Si bond, and for the rest, other peaks belonging to Ni-Ni and Ni-Si second shell are also observed.

4.1.6 EXAFS results of as-deposited sample

The Fourier transform of the as-deposited sample, compared with the $NiSi_2$ bulk sample is shown in figure 4.1.12

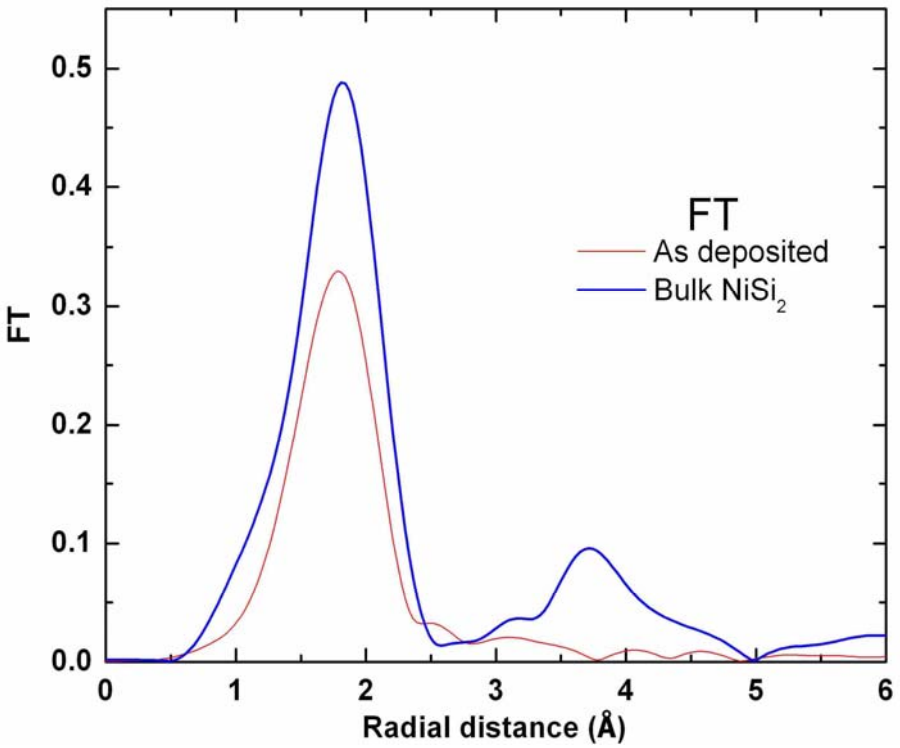

Figure 4.1.12 The first shell of as deposited sample compared with $NiSi_2$ is shown in figure.

The FT shows a single peak which depicts the absence of long range order in as-deposited sample. From Ni, as a first neighbour, Si is visible. This species recognition was carried out by scattering phases calculated by FEFF code for Ni-Si pairs. However, in the bulk $NiSi_2$ sample another peak is also observed signifying further ordering in the sample. The curve fitting to the first shell data of reference sample is

shown in figure 4.1.13 and for the as-deposited sample shown in figure 4.1.14; the fit results are tabulated in table 4.1

Table 4.1

Sample	Radial distance (Å)	Coordination number, N	Debye-Waller Factor ($Å^2$)
Reference	2.341 ± 0.005	7.73 ± 2.0	70 x 10^{-4}
As deposited	2.311 ± 0.002	4.32 ± 0.64	88 x 10^{-4}

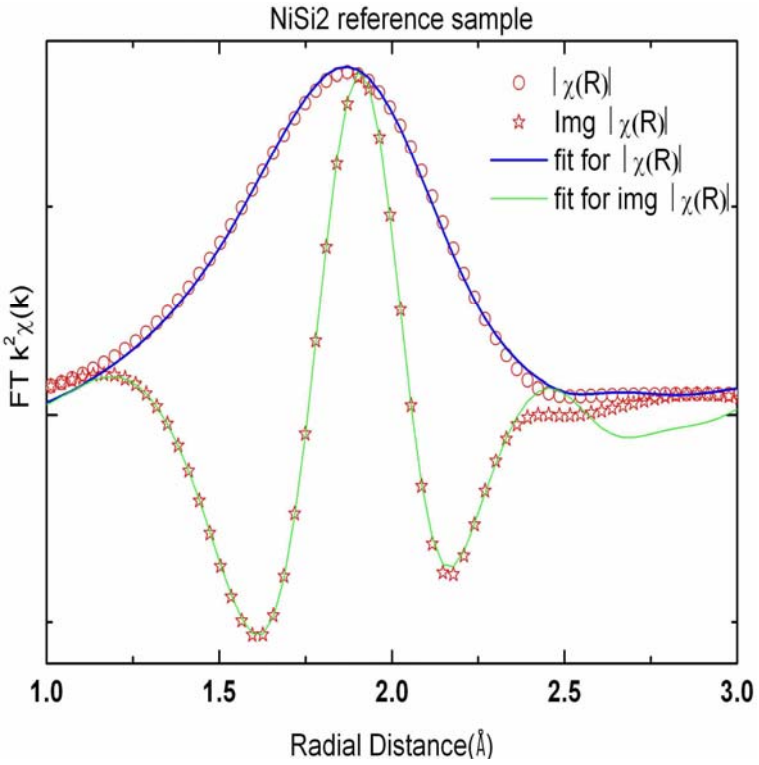

Figure 4.1.13 EXAFS first shell fit for $NiSi_2$ reference sample

The structural details of the two samples reveal that the as-deposited sample has its main peak shifted towards smaller R compared to the bulk sample. The Ni-Si distance was R =2.31 ± 0.002 Å; with coordination of N = 4.32 ± 0.64. Kawadzu *et al.*[5] prepared layered samples meaning that Ni thin film was deposited on the a-Si:H thin film as a blanket layer. Then these films were annealed at temperatures 150, 230 and

330 ^{o}C respectively. X-ray absorption coefficient was measure in fluorescence mode. These authors found that the Ni-Si distance was between 2.1 to 2.3Å with a coordination of N = 3.8. Even though we cannot make any direct comparison because of different preparation and annealing conditions, one important finding is worth noting here. The coordination number N is similar in both cases. In the report by Kawadzu *et al*, nickel interaction with a-Si is diffusion dependent but in our study the nickel atoms were buried inside the a-Si matrix because of co-sputtering. *Therefore, nickel diffusion kinetics seems to be similar in layered and co-sputtered Ni resulting in similar Ni-Si distances.*

EXAFS oscillations are resultant of a constructive interference of out going photo electron with the in coming photo electron wave after being back scattered from different neighbours. When all the neighbours are at a constant distance from the absorber in a imaginary sphere around the absorbing atom, the phase of the in coming electro wave will be with a certain path difference depending on the back scatter distance. If the back scattering atoms are at slightly different distances from the absorber the phase of the each back scattering atom will contribute individually to the interference function resulting in the different frequencies. Looking at the k space fitting shown in figure 4.1.14 (bottom) it is clearly evident that the whole EXAFS signal was a resultant of only one frequency, elucidating the fact that after the first nearest neighbour the disorder was so high that the photoelectron interference function ceases out, resulting in to one single shell i.e. is Ni-Si. However, in as-deposited sample the Ni-Si distance is larger than that reported by Kawadzu *et al.* The as-deposited sample is grown on a quartz substrate held at 200 ^{o}C during the deposition. This could be one of the reasons for having the Ni-Si distance almost similar to that of the bulk. Based on the distances and coordination numbers we obtained during the curve fitting few conclusions can be drawn.

- In thin film growth, Ni makes bonds which are more similar in nature to Ni bonds in $NiSi_2$ bulk. Kawadzu *et al.* after heat treatment at 150 and 180 ^{o}C also reported that the Ni-Si distances are ~ 0.2 Å, smaller than those in c-

$NiSi_2$. These small distances signify that Ni can be an interstitial as suggested by Tu [6]

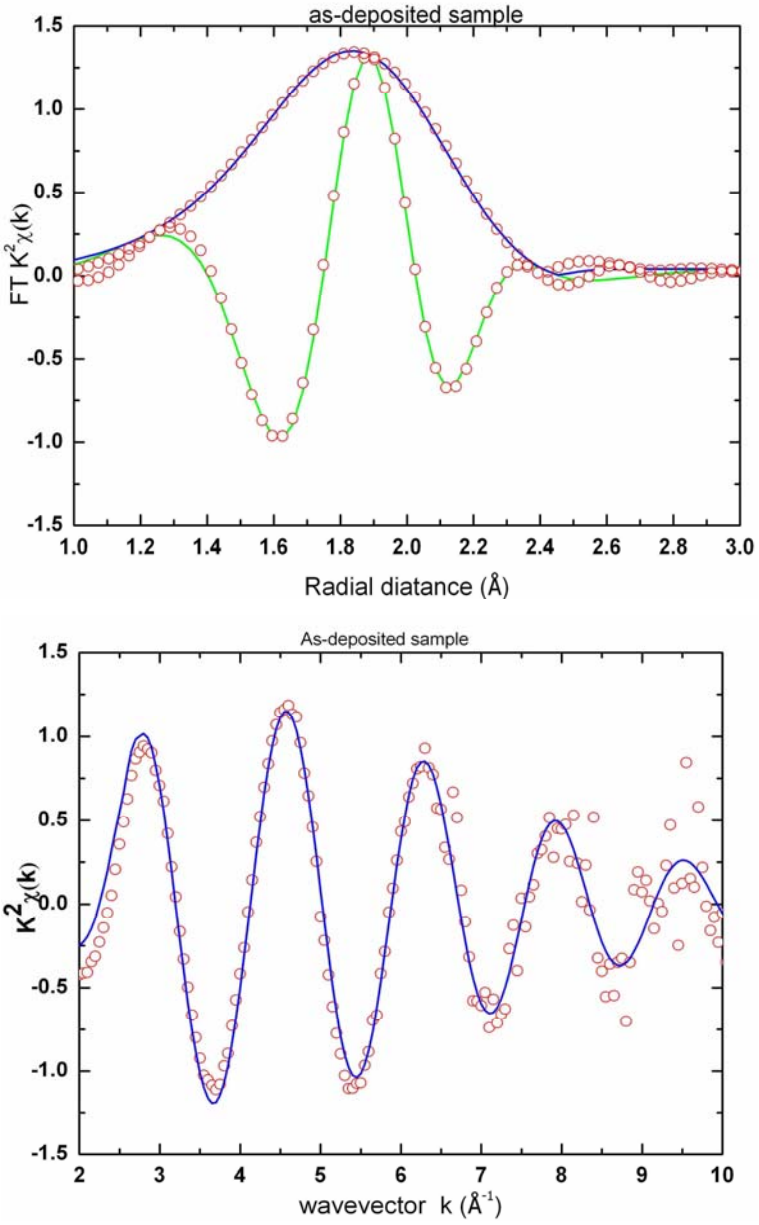

Figure 4.1.14 EXAFS first shell fit for as deposited sample in R space *(top) Top figure:* magnitude and imaginary part (*open circles*) their fit (*solid line*) and in k space: *Bottom figure* EXAFS signal (*open circles*) its fit (*solid line*)

- B T Williams *et al.* and Asal *et al.* [7, 8] showed that the Ni-Si distance is invariant with concentration of Nickel in the a-Si matrix. Thus, the Ni-Si

distance is diffusion dependent of Ni in a-Si matrix, annealing temperature and duration of annealing.

- Samples investigated by Comin *et al.* [9] were also similar to Kawadzu *et al.* but the measurements were SEXAFS, that is more confined to the surface. These authors found that as soon as Ni deposition started on the top of a-Si, Si-Ni-Si layer will form and excess Ni will diffuse in to the Silicon matrix as a substitute for the Si atoms.
- In this present work the coordination of Ni with Silicon in the as-deposited sample was N= 4.32 ± 0.64 suggesting that Ni becomes a constituent of the silicon tetrahedral network instead of remaining as an interstitial atom. Here one important point is worth mentioning; Ni is an interstitial atom in the case of the crystalline entities of silicon, but when the Silicon is amorphous, Ni is always inside the a-Si matrix. When Ni attains the co-ordination of four which is the inherent property of Silicon network we say that Ni is in side the a-Si network. Ni possessing large coordination number, N= 8, in its bulk form, it should attract more Silicon atoms resulting in to shrinkage of the Ni-Si distance observed by Kawadzu *et al*., Once Ni becomes part of the Silicon network Ni attains effective coordination number of four following Mott's "*8-N*" rule.

- According to Mott's "8-*N*" rule [10] and a modified *8-N* rule by Street [11], at the time of deposition the dopant becomes charged and takes the coordination of the host network. The same is evident in the case of nickel in the a-Si matrix, with an effective coordination of N = 4.3 ± 0.64. These results are in good agreement with SEXAFS studies of Comin *et.al*., and this once again reconfirm that Ni is a substitutional atom in the a-Si network not an interstitial.

4.1.7 EXAFS results of annealed samples

Three samples with 0.5% of Ni were annealed at three different temperatures 600, 700 and 800 ^{o}C for constant time of 15 minutes as described earlier in sample preparation. After annealing a-Si was expected to have structural relaxation and subsequent crystallization. Metal induced crystallization enhances the processes of relaxation and crystallization by several orders of magnitude. With a metal contact the crystallization time of semiconductors, now has been decreased from tens of hours to few minutes. The structural ordering, and eventual crystallization in a-Si after adding Ni, local atomic network rearranges in a-Si matrix and its qualitative changes were quantified by EXAFS measurements. Apart from the prominent first peak which belongs to Ni-Si that remains unaltered, another peak comprised of Ni-Ni and Ni-Si (next nearest neighbour) distances at 3.8 and 4.5 Å respectively, based on the $NiSi_2$ crystallographic structure shows up in the FT. However, the signal to noise ratio of fluorescence yield recorded was not sufficient to extract the second shell structural parameters with an acceptable accuracy. Thus, we confined the EXAFS signal analysis only up to the first nearest neighbour. The analysis was carried out by curve fitting using the theoretically calculated phase and amplitude functions from FEFF 6.0 code, which have been used to rule out the presence of Ni clustering and other nickel silicide compound with NiSi and Ni_2Si structures. The fits to the EXAFS data in R-space and in k-space for the all the three annealed sample are shown in figures 4.1.15 to 4.1.17. The bond lengths and effective coordination number of Ni in the as deposited sample and samples annealed at 600, 700 and 800 ^{O}C are tabulated below in table 4.2. **R-**factor denotes the goodness of the fit, the lowest R factor the best the fit . {*Instead of χ^2 for the goodness of the fit we have adopted the R factor, which was directly proportional to χ^2 and then scaled to the magnitude of the data itself, and any value greater than certain limit can not be a good fit.*} According to the FEFFIT manual R < 0.02 can be considered as very good fit.

Table 4.2

Sample	Distance (R) Ni-Si(Å)	Co-ordination number N	DW factor(Å)^2 X 10^{-4}	R-factor (from the fit)
$NiSi_2$	2.341 ± 0.005	7.73 ± 2.00	70	0.020
Asd	2.312 ± 0.002	4.32 ± 0.64	88	0.070
600	2.333 ± 0.002	7.68 ± 0.44	38	0.010
700	2.325 ± 0.003	6.00 ± 1.2	36	0.015
800	2.338 ± 0.002	7.74 ± 0.72	40	0.033

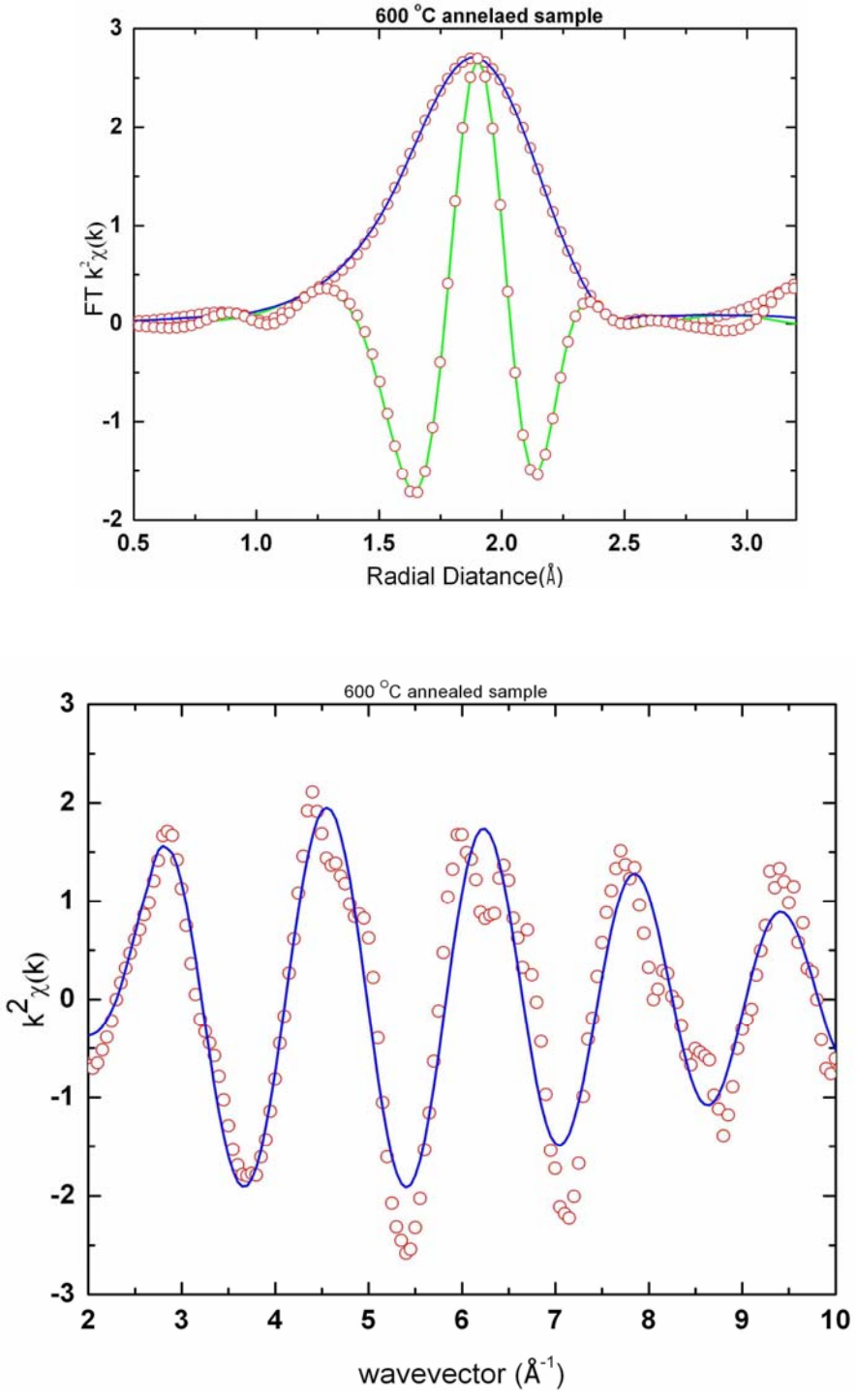

Figure 4.1.15 EXAFS first shell fit of 600 °C annealed sample in R space *Top figure:* magnitude and imaginary part (*open circles*) their fit (*solid line*) and in k space: *Bottom figure* EXAFS signal (*open circles*) its fit (*solid line*)

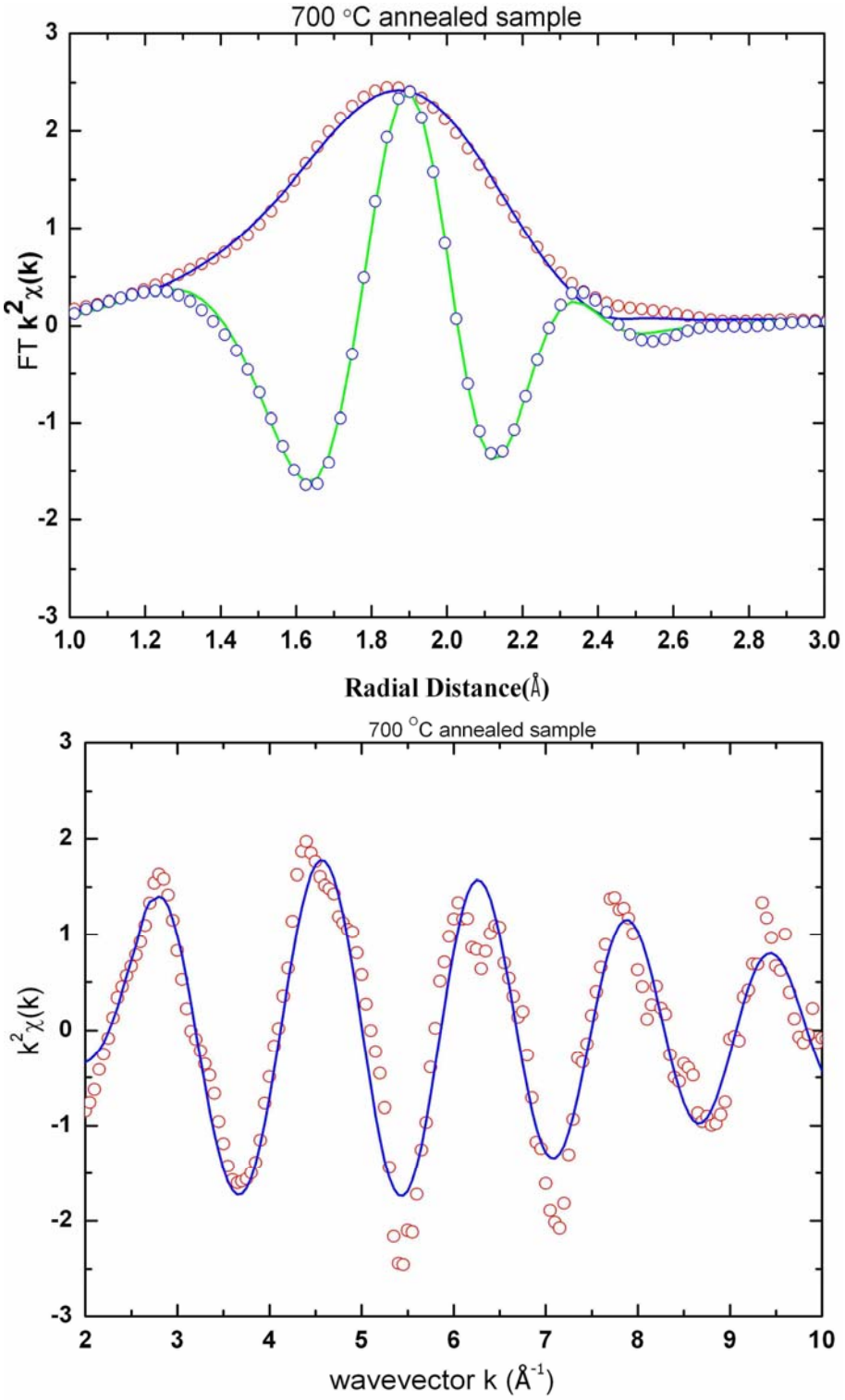

Figure 4.1.16 EXAFS first shell fit of 700 °C annealed sample in R space *Topfigure:* magnitude and imaginary part (*open circles*) their fit (*solid line*) and in k space: *Bottom figure* EXAFS signal (*open circles*) its fit (*solid line*)

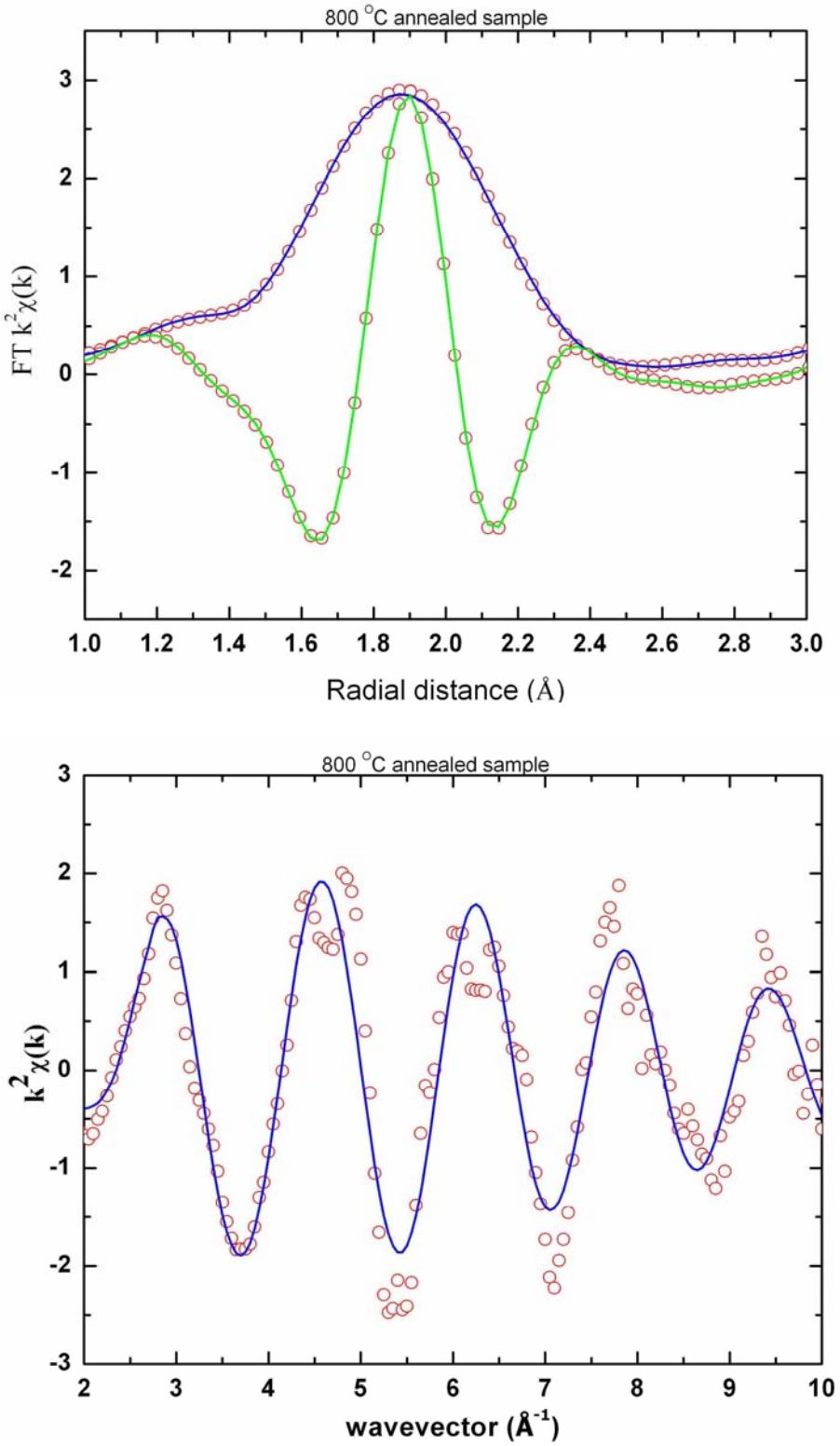

Figure 4.1.17 EXAFS first shell fit of 800 °C annealed sample in R space *Topfigure:* magnitude and imaginary part (*open circles*) their fit (*solid line*) and in k space: *Bottom figure* EXAFS signal (*open circles*) its fit (*solid line*)

In the previous section it was shown that in the as-deposited sample, around nickel four Silicon atoms were bonded at a distance of 2.31 ± 0.002 Å in a tetrahedral configuration, similar to the a-Si network. When the samples were annealed at 600 ^{o}C, the local structure first relaxes and then rearranges such that next nearest neighbour of Ni, as second shell, was observed at a distance of approximately 4.6 Å. The first nearest neighbour distance between Ni-Si increased to 2.333 ± 0.002 Å. With in the accuracy of the experiment and data analysis this value was almost similar to that of Ni-Si distance determined from X-ray diffraction in bulk $NiSi_2$. The radial distance R, coordination number N and Debye-Waller factor σ^2 are plotted as a function of annealing temperature in figure 4.1.18 to 4.1.20 respectively. {*It may be noted that 200 ^{O}C does not mean that sample was annealed at that temperature at 200 ^{O}C but that the substrate temperature was held at 200 ^{O}C while deposition*}.

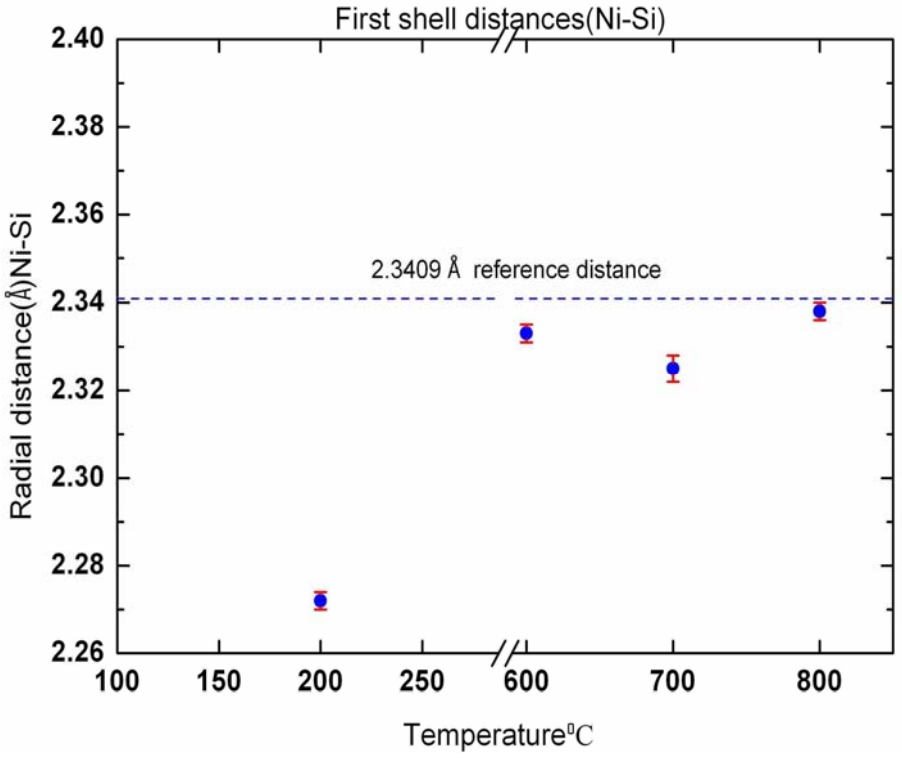

Figure 4.1.18 Radial distance of Ni-Si after EXAFS first shell fit.
(200 °C represents the as-deposited sample).

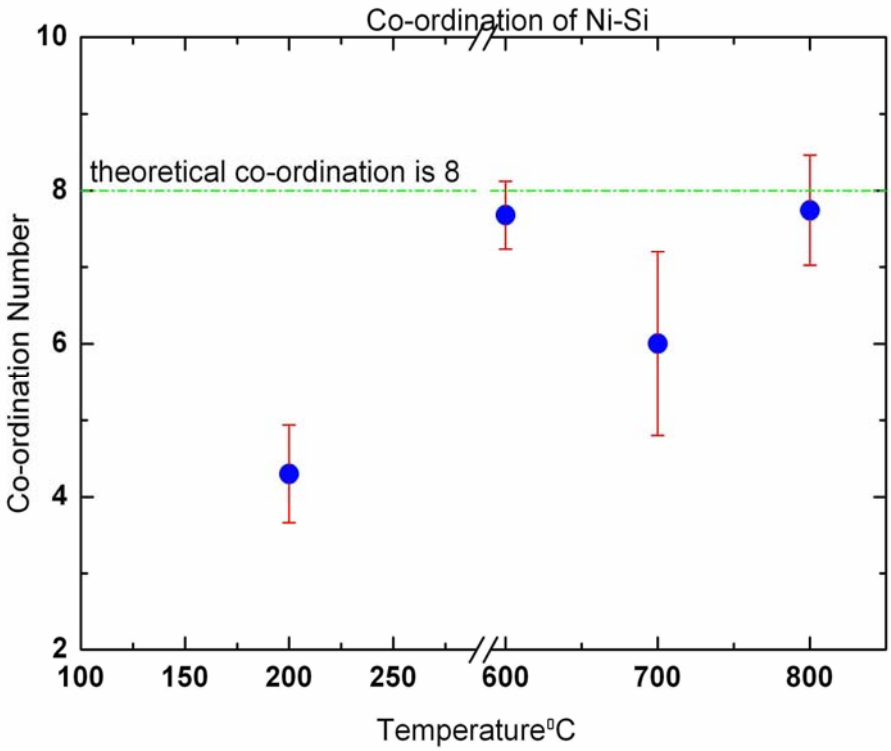

Figure 4.1.19 Coordination number of Ni after EXAFS first shell fit.
(200 °C represents the as-deposited sample).

The increase in the coordination number N= **7.68 ± 0.44** from 4 signifies the improvement in the Ni local environment after annealing i.e, 'new bonds were formed'. The Debye-Waller factor, the measure of disorder in the atomic distances; (static disorder) decrement in this parameter also depicts the same structural rearrangement around nickel atoms in the 600^{o}C annealed sample.

For 800 ^{o}C annealed sample the Ni-Si distance R= **2.338 ± 0.002** Å and the coordination number N= 7.74 ± 0.72 **with** $\sigma^2 = 40 \times 10^{-4}$ (Å)^2 **.** The Ni-Si bond lengths for the samples annealed at 600 ^{o}C and 800 ^{o}C, shows similar nature, whereas, for the 700 ^{o}C annealed sample, bond length and coordination decreases N= **6.00 ± 1.2**. This can be explained from the fact that while nickel reacting with a-Si, at 700 ^{o}C an amorphous phase formation as observed in bulk samples as $NiSi_2$ decomposes into NiSi and Si. Here the comparison of FT 700 ^{o}C and 600 ^{o}C gives a direct evidence for numerous facts found by Loomans *et al.*[12].

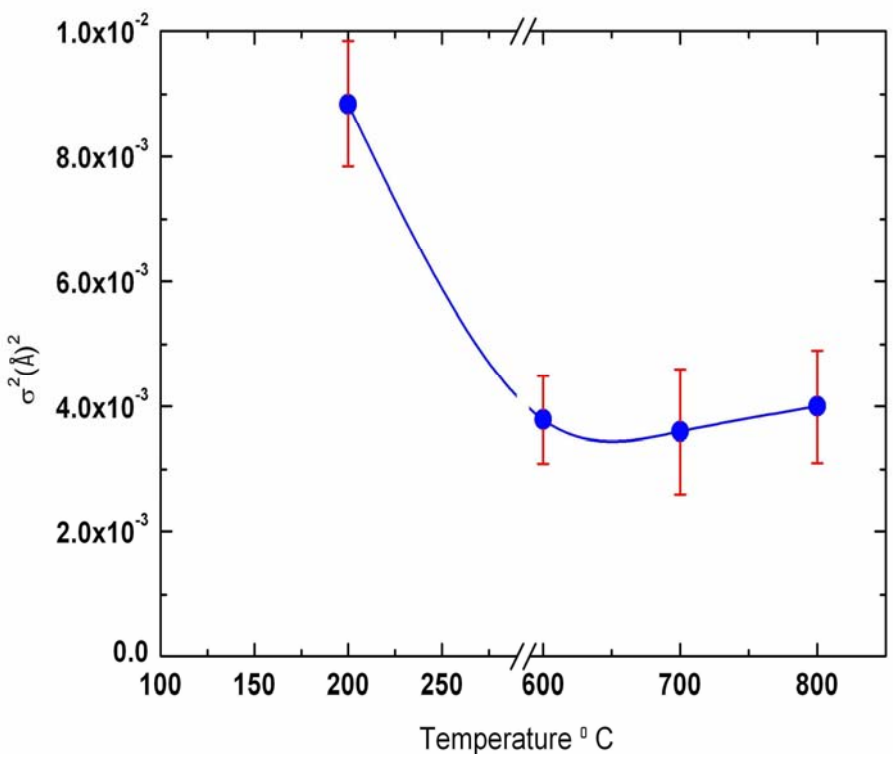

Figure 4.1.20 Radial distance of Ni-Si after EXAFS first shell fit.

(200 °C represents the as-deposited sample.)

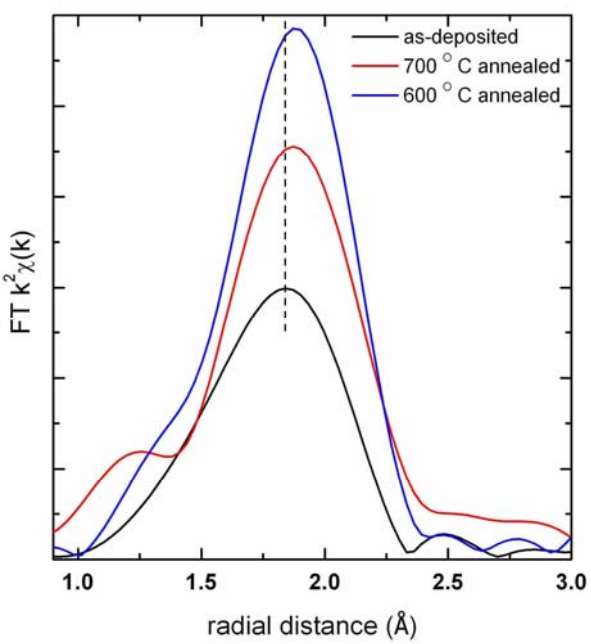

Figure 4.1.21 | χ(R) | of as-deposited and 600 °C and 700 °C annealed samples

The as-deposited sample has the lowest peak height consistent with its lower coordination and high disorder. Between 600 and 700 ^{o}C only, there is a discrepancy raising questions on the crystallanity of the samples. From Raman scattering experiments there was no evidence of crystalline Si in the 600 ^{o}C annealed sample, but a crystalline Si peak in the Raman spectra was observed at 700 ^{o}C annealed sample.

From the FT, the decrease in the peak intensity can, therefore be explained as follows

- Interstitial nickel atoms around the nickel atom inside the a-Si matrix were present in a typical geometry, which aids the Si-Si bond breaking at low energies.[6]
- This typical geometry was explained by Comin *et al.* [9]
- According to Looman *et al* the decomposition of $NiSi_2$ at 700 ^{o}C, follows

$$NiSi + Si \rightarrow NiSi_2$$

and

$$NiSi_2 \rightarrow NiSi + Si$$

These two factors, put together, were the principle factors for divergent behaviour of the 700 ^{o}C annealed sample. Though we have not observed any signs of NiSi but the possibility of formation, after a long annealing duration cannot be ruled out completely.

At this point it is necessary to present Raman scattering data to reinforce the EXAFS results in order to explain the role of Ni in metal induced crystallization of a-Si. Raman spectra of the substrate, which was crystalline quartz and the samples' are shown figure 4.1.22.

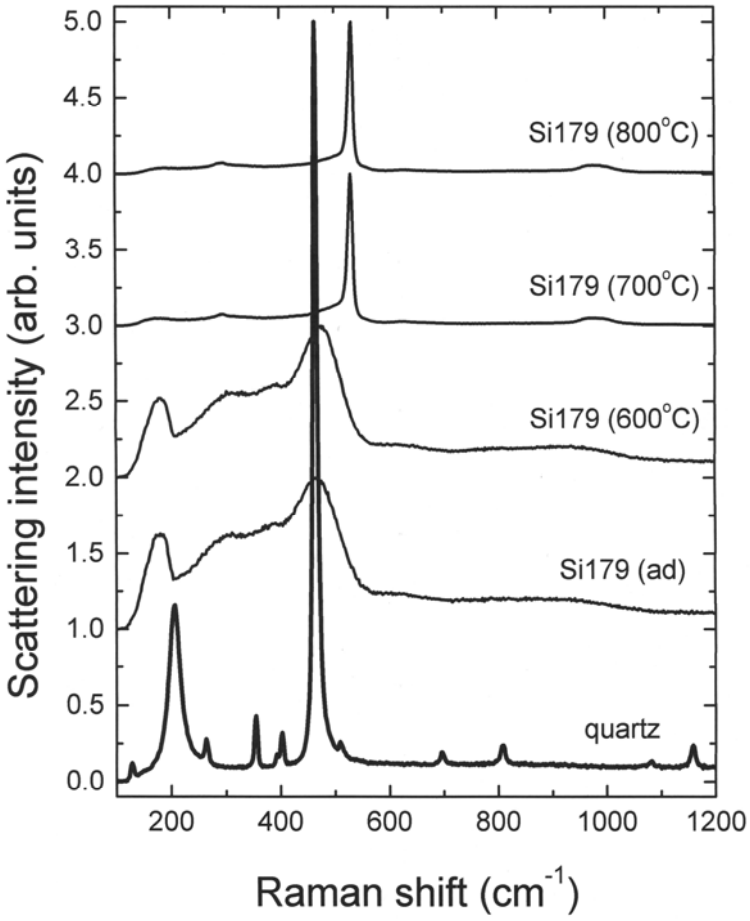

Figure 4.1.22 Raman spectra of the as-deposited and annealed sample along with the quartz substrate

Raman spectra of quartz shows a typical crystalline α-SiO_2 vibrational spectra with the Raman peaks centered at 207, 265, 356, 401, 450, 464, 509, 697, 807, 1085, 1163 cm^{-1} [13].When the samples are annealed at 600 ^oC the Ni-Si bond length attained a value of 2.333 ± 0.002 Å, which is similar to distance of Silicon atoms from Nickel in $NiSi_2$. At this stage no crystallinity was observed from Raman scattering experiments. Earlier work on Ni/a-Si systems, the MIC phenomenon has modeled as epitaxial growth of silicon on the (111) face of the $NiSi_2$ crystallites (termed as nodules) present in the sample. In the 600 ^oC sample $NiSi_2$ nodules were present according to EXAFS results. Though the second shell details were not decipherable, the more likely structure around nickel was $NiSi_2$. At this stage partial crystallization is

expected, this lack of crystallization can be explained as a consequence of the shorter duration of annealing compared with entire literature. When the samples are annealed at 700 ^{o}C, Raman spectra shows a crystalline Silicon peak centered at 519 cm^{-1}. But at this temperature the nickel environment was a bit distorted with low Ni-Si bond length compared to 600 ^{o}C and 800 ^{o}C annealed samples, with in the limits of experimental error in determining the distances. The cause for this peculiar behaviour was explained as $NiSi_2$ decomposition in to NiSi and Si at a temperature of 700 ^{o}C. As the growth models about the silicon epitaxy suggested, Silicon epitaxial growth is more likely on (111) plane of $NiSi_2$, where Ni-Si distance is 2.34 Å. In 700 ^{o}C annealed sample the Ni-Si distance is found to be 2.325 ± 0.003 Å and large disorder parameter value suggesting interstitial nickel. In the figure 4.22 the peak height of the FT of 600 ^{o}C and 700 ^{o}C are shown. The 700 ^{o}C annealed sample's peaks height is smaller than that of 600 ^{o}C. This is formation of Ni substitution of Si position in a-Si matrix. The phase shift of Ni-Ni pair and Ni-Si pairs were shown in figure 4.1.8. It is evident that the difference between the Ni-Ni and Ni-Si phase shifts should lead to a destructive interference reduction in the EXAFS amplitude, evidenced in the present study. The above conclusion gives evidence from EXAFS that Ni-Si facets offers more localized free energy for Silicon epitaxial growth on $NiSi_2$. Growth of silicon on this facet will be more strained, originated when Ni starts breaking the Si-Si bonds in its way of diffusion. It is true that nickel silicide is formed, but the role of silicide in the crystallization of Si is still not clear.

While Ni on the lattice site of Silicon is unsaturated with only four covalent bonds instead of eight, Silicon has a tetrahedral bonding structure with four other Silicon atoms. As a-Si can also have the same tetrahedral bonding nature but its long range characteristics were lost. Therefore, few unsaturated bonds due to dangling and void structures will occupy certain volume of the a-Si thin film decreasing the density of the a-Si to 0.98 of the c-Si. When Ni enters such a network, being charged, various set of events may occur in the a-Si matrix.

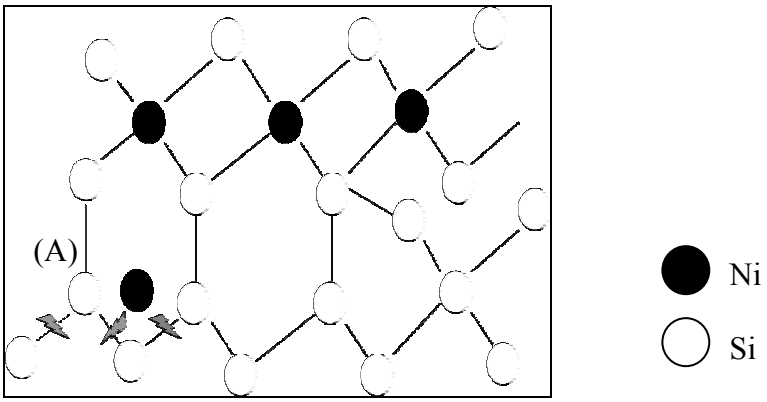

Figure 4.1.23 Schematic diagram depicting bond breaking and making nature of the Ni inside a-Si matrix.

- Ni can attract the dangling bonds in a-Si thus bonding with three Silicon atoms to form a Si tetrahedral. Here Ni will be a substitutional atom for Si. This has been observed in as deposited samples where Ni has four neighbours.
- With diffusion, Ni weakens the Si-Si bonds at site 'A', since Ni has more valence electrons to attract silicon atoms. A schematic of this picture is drawn in figure 4.1.23
- Silicon atoms will take the bond to the Ni atoms and take the structure that looks similar to the $NiSi_2$ structure.
- In TEM experiments it is difficult to distinguish between $NiSi_2$ and Si because both have same lattice constant. This has been pointed out by Camarata *et al*. and Camapisi *et al*. [14, 15]
- All the earlier studies on MIC and proposed models are based on the TEM results only.
- For the first time MIC has been studied using EXAFS.

The EXAFS results, in conjunction with Raman spectroscopy reveals the atomic scale mechanism which plays an important role in metal induced crystallization in a-

Si. Taking the analogy of hydrogen induced crystallization in silicon as explained by Saravarapriyan Sriraman *et al.* [16]; "Hydrogen exposure first relaxes the strained Si-Si bond, while making a Si-H-Si bond formation. After H moves away from the bond center the Si-Si bond either breaks or relaxes resulting in to the local structural rearrangement and that bond lengths and angles were found to be more similar to the c-Si". Based on the experimental observations in the present study and also the earlier works like Comin *et al*.[9] a similar kind of phenomenon appears to be responsible in the case of Ni induced crystallization of a-Si. Ni enters the a-Si network as a substitute of Silicon atoms and relaxes the silicon network. It forms the bonds Si-Ni-Si similar to hydrogen. This kind of bond formation was observed experimentally by Comin et al . When Ni leaves the Si-Si bond, the bond has to relax or it has to break, resulting in the changes and rearrangement of local structural order. The relaxation of the amorphous network has been observed from the decrease in the σ^2 values for as deposited and annealed samples. The concentration of Ni was 0.5 at wt%. This concentration was not sufficient for the complete formation of $NiSi_2$ nodule in the thin films. Amorphous to crystalline phase transformation requires the creation of dangling bonds or breaking bonds, migration of these bonds and their rearrangement in to new bonds. This has been achieved by using small amount of metal in a-Si matrix and this is metal induced crystallization.

4.1.8 Summary

The EXAFS results can be briefly summarized here

- Ni in a-Si matrix acquires the coordination of a-Si (N= 4). This is consistent with Mott's *8-N* rule.
- Ni is a substitutional atom in the a-Si network not an interstitial.
- After annealing, structural rearrangement takes place around nickel in Silicon matrix and the local environment of Ni is similar to the case of $NiSi_2$
- Annealing at 600 °C, the a-Si network relaxes and the bond length of Ni-Si reaches 2.34 Å almost similar distance of bulk $NiSi_2$.

- When the samples were annealed at 700 °C a-Si starts crystallizing as observed in Raman spectra.
- At a temperature of 800 °C annealing there is no further effect on the structural parameters.
- The bond length and co-ordination remained almost unaltered at 600 °C and 800 °C.
- Small variation in distance and reduction in the coordination was observed when samples were annealed at 700 °C. These variations were explained by possible decomposition of $NiSi_2$ in to NiSi and Si.
- Taking the analogy of hydrogen induced crystallization, a phenomenological model for Metal induced crystallization was proposed. According to this model Ni plays the major role rather than nickel silicide after interpreting the EXAFS results. This model is an experimental confirmation of theoretical models proposed by Khait *et al*. and M Walutelet [17, 18].

References

1. Kuznetzov, B. Svensson, *Appl. Phys. Lett*. 66, 2229, (1995)
2. M. Newville, P. Livins, Y. Yacoby, E. A. Stern, and J. J. Rehr, *Phys. Rev. B*,**47**,14126, (1993)
3. K N Tu in *Advances in Electronic materials* edited by B Wessels and G V Chin (American society for Metals, Metals Park, Ohio 1986).
4. K Schubert and H Pfisterer, *Zeitschrift fuer Metallkunde* 41, 433 (1950)
5. Yousuke Kawadzu, Mitsuru Iioka, Americo Fuji, Hiroyuki Oyannagi and Toshihiro Arai, *Applied Surface Science* **41-42,** 296 (1989)
6. K N Tu *Appl. Phys. Letters,* **27,** 221 (1975)
7. B T Williams, S J Gurman, S C Bayliss and E A Davis *J. Phys: Condens. Matter* **12 ,**5971, (2000).
8. R Asal, S H Baker, S J Gurman, S C Bayliss and E A Davis *J. Phys: Condens. Matter* **4,**7169, (1992)
9. F Comin, J E Rowe and P H Citrin, *Phys.Rev.Lett*. **51**, 2402, (1983).
10. N F Mott, *Adv. Phys.**16*** 49 (1967)

Optical Characterization

Amorphous Silicon thin films

Optical Characterization

This chapter presents the details of optical characterization of silicon thin films by Raman spectroscopy, spectral transmission and specular reflectance by UV-Vis-NIR spectrophotometry. The silicon films crystallized by MIC have been characterized by these methods to determine their properties such as phase sensitive vibrational frequencies, refractive index, optical absorption coefficient and optical band gap. A clear and complete knowledge of optical properties is an important component to establish the suitability of the Si films being studied for technological applications. The main motivation for studying the optical properties in great detail is that they provide a simple tool to understand the fundamental mechanisms of growth of films, their crystallization as well as the local electronic structure. These are important from both technological and physics points of view.

In particular, the optical properties of the pure/intrinsic and Ni, Cr metal doped a-Si thin films are presented. The content emphasizes on the metal induced crystallization (MIC) and its effects on the linear optical properties of MIC crystallized Silicon thin films. Thus, the entire chapter has three subsections, each devoted to amorphous Silicon thin films, Ni induced crystallization and the final section is about Cr induced crystallization in a-Si thin films.

4.2 Amorphous Silicon thin films

4.2.1 Raman spectroscopy of a-Si

The Raman central frequency for a-Si varies from 460 cm^{-1} to 480 cm^{-1} depending on the local order of the a-Si. The substrate effects have already been ruled out by Iqbal *et al.* [1]. The Raman spectrum of a-Si thin films evaporated on to glass substrates is shown in figure 4.2.1. The Raman signal from 400 to 600 cm^{-1} was modeled using a Voigt like function in order to find the central Raman frequency and peak width as they have correlation with structural properties.

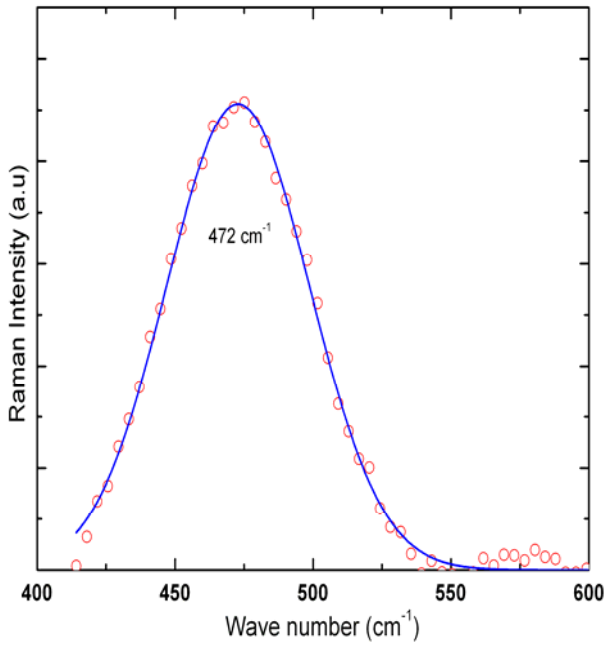

Figure 4.2.1 Raman Shift of evaporated a-Si (*Open circles*) Voigt fit (*Solid line*)

Amorphous Si thin film of 100 nm thickness deposited by thermal evaporation on glass showed a Raman frequency, centered at 472 cm^{-1} and whose peak width 61 cm^{-1}. This position of frequency signifies the presence of amorphous clusters comprised of approximately 200 silicon atoms [2]. The Raman spectrum of ion beam sputtered Silicon thin film, again on glass held at room temperature with the incident beam energy of 600 eV is shown in figure 4.2.2. The central Raman frequency shifts towards higher wave numbers of 483 cm^{-1}, which is close to the 512 cm^{-1} of bulk Silicon. On increasing the

incident ion energy to 700 eV the Raman spectrum shows entirely different features. The Raman spectra shown in figure 4.2.3, depicts the different contributions de-convoluted from the original Raman signal. The primary peak at 472 cm^{-1} can be assigned to amorphous Silicon and 503 cm^{-1} to cubic/wurzite nanocrystalline Silicon embedded in a-Si matrix. It is a very well known fact that amorphous Si network consists of wurzite like micro crystallites as predicted by *microcrystallite* theory. [3]

In Raman spectroscopy, few of the peak parameters are correlated to the structural parameters like, the Raman peak position (ω_{TO}) and FWHM (Γ) are related to the root mean square variation in the bond angle '$\Delta\theta$' of a-Si by the relations given below, [4]

$$\frac{\Gamma}{2} = 3.2\Delta\theta + 9.2 \qquad \text{..... (4.2.1)}$$

$$\omega_{TO} = -2.5\Delta\theta + 505.5 \qquad \text{.....(4.2.2)}$$

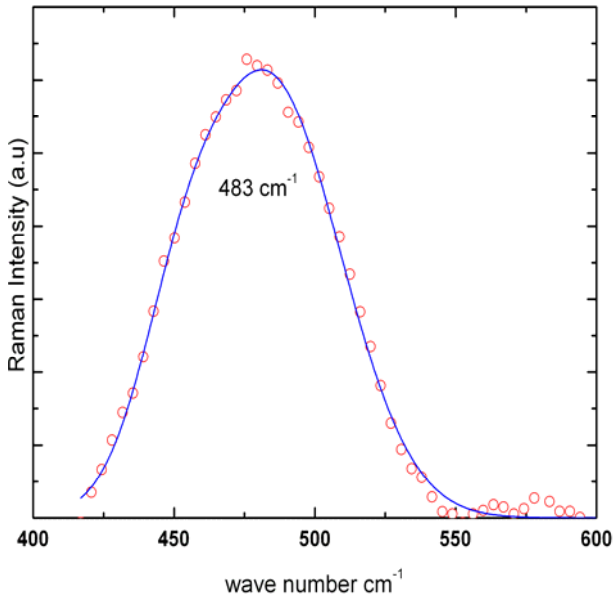

Figure 4.2.2 Raman shift of ion beam sputtered a-Si thin film with incident ion energy of 600 eV (*Open circles*) Voigt fit (*Solid line*)

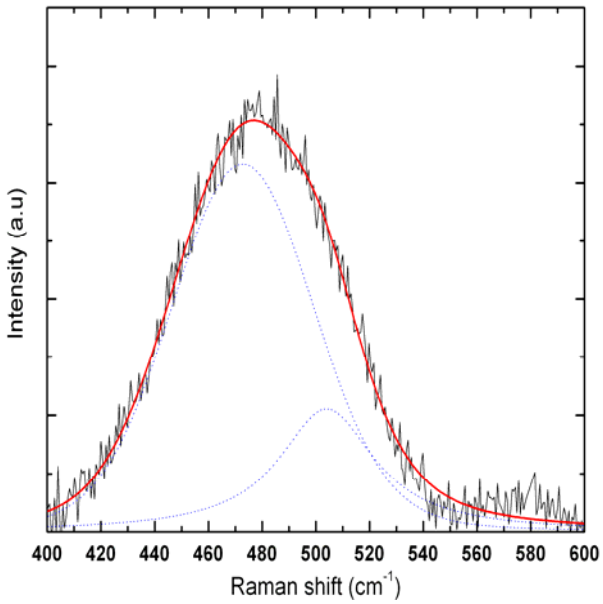

Figure 4.2.3 Raman shift of ion beam sputtered a-Si thin film with incident ion energy of 700 eV Shows two contributions belongs to amorphous silicon and nanocrystalline (*details in the text*)

Raman Peak (ω) cm^{-1}	FWHM(Γ cm^{-1})	Δθ in degrees From peak broadening	Δθ in degrees From peak position
472(evap)	61.37	6.51061	13.4
472 (IBS@700 eV)	54.19	5.42273	13.4
483(IBS@600 eV)	60.08	6.31515	9
504(IBS@700 eV)	43.55	3.81061	0.6

It is evident that as the central frequency of Raman peak moves towards the bulk Silicon value of 520 cm^{-1}, the 'Δθ' values decreases. The decrease in the Δθ values signifies the improvement in the structural order. The Raman central frequency of evaporated Silicon at 472 cm^{-1}, has FWHM of 61.37 cm^{-1} and Δθ value of 6.5°. At the same central frequency of 472 cm^{-1}, ion beam sputtered Silicon possess only 54 cm^{-1} of broadening and the bond angle variation of 5.4° only. For the peak at 504 cm^{-1} the Δθ value is 0.6°, which means that the bond angle variation of the nanocrystalline Silicon is very small and comparable to that of the single crystal value.

In conclusion, this section presented the Raman spectra of a-Si samples prepared by evaporation and ion beam sputtering. All the samples regardless of thickness show a Raman peak that centers between 460 and 480 cm^{-1}. The Raman spectra of ion beam

sputtered a-Si thin films with two different incident ion energies exhibit traces of nanocrystallization at 700 eV of incident ion energy. The FWFM and Raman peak positions are correlated to the 'Δθ' root mean square variation the bond angle, and the 'Δθ' values suggests that ion beam sputtering is a preferable deposition process to prepare low defect density a-Si on glass.

4.2.2 Morphology

An optical micrograph of a-Si thin film grown on glass by thermal evaporation is shown in figure 4.2.4. The observed microstructures are very familiar features in MBE grown epitaxial Silicon thin films and are known as shallow saucer pits (S-pits) [5]. These structures have also been interpreted as point defects or clustered crystallographic imperfections. The Silicon thin films shown in these images were X ray amorphous and hence the saucer pits seen in our samples cannot be due to crystallographic imperfections. The possible reasons for this kind of growth in MBE grown silicon thin films were attributed to poor vacuum conditions ($<10^{-7}$ Torr) and low substrate temperatures during deposition (< 700 ^{o}C). According to Pearce *et al.* metal contamination will also cause S-pits [6].

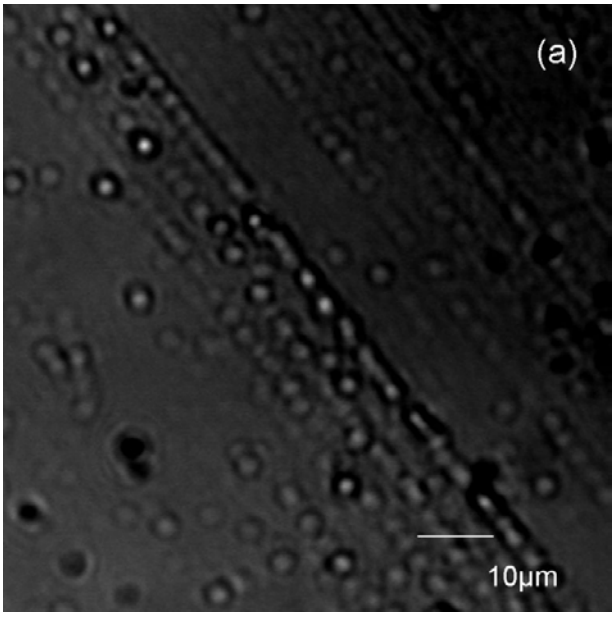

Figure 4.2.4 Optical micrograph shows lines of saucer pits formed on the surface of the a-Si thin films deposited on glass.

In our case, the films were deposited on substrates held at ambient temperature during deposition and in vacuum of 10^{-6} Torr and these can be the causes for the formation of the S-pits. In ion beam deposited Silicon thin films, optical microscopy does not show any morphological features and we believe that the surface features are much smaller than that of the wavelength of the light we have used (488 nm). Hence Atomic force microscopy, through which in the non contact dynamic mode of operation was used, to observe the growth states of the thin films described by cone model as shown in figure 4.2.5

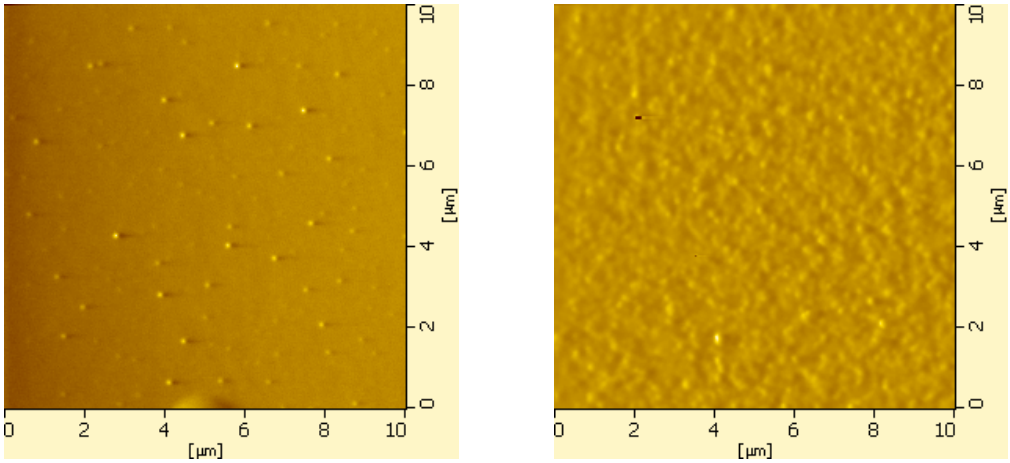

(a) (b)

Figure 4.2.5 The surface morphology of a-Si thin films grown by ion beam deposition (a) 30 nm thick and (b) 70 nm thick

4.2.3 Optical Properties of evaporated Si thin films

Thin films of Silicon were grown on the glass and quartz substrates by thermal evaporation from a tantalum boat. A detailed sample preparation was described in the section (2.1). The optical constants of these films were determined using the envelope technique [7] method from measured spectral transmission curves. When the film thickness is less than a quarter wavelength or of the order of 100 nm, the interference fringes due to multiple reflections between the film and the substrate are absent and the envelope technique is no longer valid. Hence, a computer code "PUMA" [8] was used to determine the optical constants of thinner films.

The optical transmission spectra in of the Silicon thin films grown on the glass substrate are shown in Figure 4.2.6. For substrates held at ambient temperature. For all the samples used for optical studies of this thesis, unless otherwise mentioned, the distance between the source and the substrate D_{s-s} = 8 cm kept, constant. This particular distance has been chosen for the following reasons

- A uniform thickness of the film over an area of 1.0 Sq inch was achieved.
- The substrate temperature does not increase more than 80 ^{o}C through out the deposition process.
- No crystallization should occur while deposition.
- Very low distance of 3 and 5 cm of D_{s-s} causes the films to peel off from the glass as well as from quartz substrates.

On glass, as deposited a-Si thin films, were X-ray amorphous. Even after annealing at 600 ^{o}C also the films were found to be amorphous. The optical properties of a-Si thin films grown on quartz substrate are found similar to those deposited on glass. Even after 48 hrs of annealing at 600 ^{o}C no traces of crystallization was found in silicon thin films and the optical properties remain unchanged. In a normal furnace atmosphere it is more likely that films get oxidized. The oxidation effect has been observed on films that are annealed for 1 or 2 mins and after 5 mins of annealing, the oxidation effects do not show much difference in optical transmission spectra. It is a well known fact that the oxide layer on the top of the film does not allow any more oxygen atoms to penetrate in to the film.

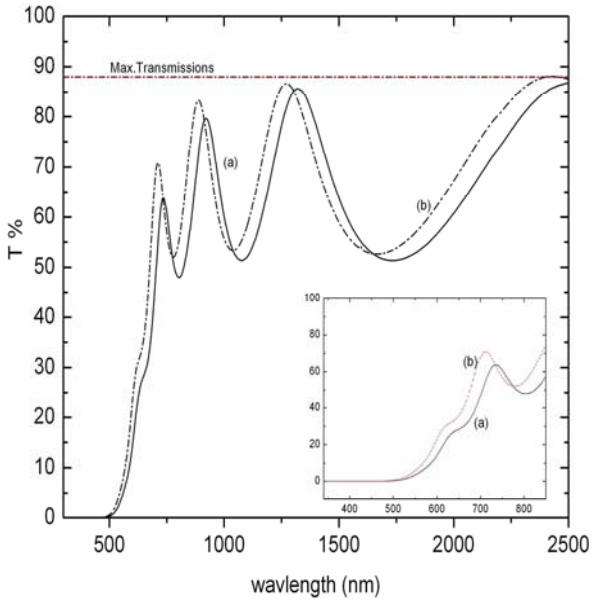

Figure 4.2.6. Optical transmission spectra of 460 nm thick sample (a) as deposited a-Si thin film (solid line), (b) after annealing at 600 ^{O}C for 5 minutes.

Therefore, the thickness of oxide layer will be confined to 2 to 5 nm. No surface analysis for the determination of oxygen content was attempted, as this oxide layer has no effect in metal induced crystallization.

Due to annealing, the absorption edge shifts towards lower wavelengths manifesting the increase in the band gap. The effect of annealing can be observed profoundly when the refractive index of the films was determined. The refractive index and the structure of the material are related by a simple empirical relation, as defined by S H Wemple *et al*. [9, 10]. According to Wemple *et al.* "*Apart from density differences associated with voids and inefficient packing of disordered atoms, the main quantity of interest turns out to be the coordination number*". The behavior of the refractive index was measured by a quantity called dispersion energy, E_d, which is not significantly affected by lack of long range order.

4.2.3.1 Behaviour of Refractive index

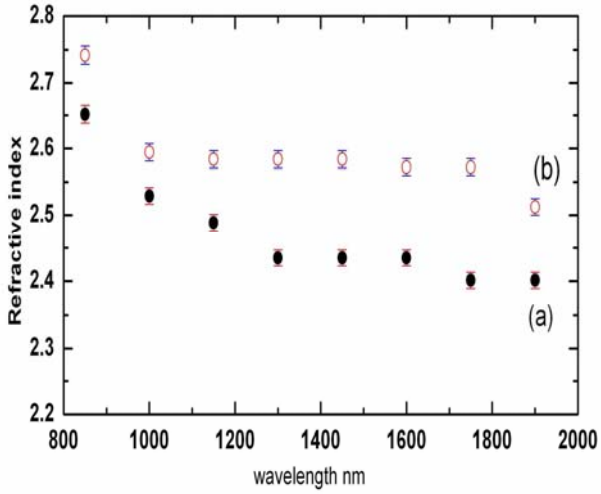

Figure 4.2.7 The refractive index of 460 nm thick, a-Si thin film on glass as deposited (*solid circles*) and annealed (*open circles*)

The dispersion in the refractive index as a function of wavelength is shown in Figure 4.2.7 for the as deposited and annealed films. It is evident that, with in the error of the measurement, the refractive index did not change considerably even after annealing; and the values of refractive index were 2.89 at 800 nm and 2.73 at 1800 nm respectively for as deposited sample and 2.92 at 800 nm and 2.71 at 1800 nm for annealed sample. Brodsky *et al.* [11] observed a decrease in the refractive index up on annealing. These values were less than the values reported for polycrystalline Silicon at respective wavelengths, the refractive index value was 3.6[12]. This manifests the empirical law proposed by Wemple *et al.* [9] that the refractive index is dependent on the coordination number and a-Si has lower coordination when compared to polycrystalline Silicon. Generally, the films grown on glass by simple thermal evaporation will have certain void volume apart from the lower coordination, in the case of Silicon < 4, which will eventually result in low values of refractive index.

Effect of thickness and substrate temperature on the behavior of the refractive index is shown in figure 4.2.8 and figure 4.2.9 respectively. As shown in figure 4.2.9 When the films were deposited on a substrate which was held at room temperature the refractive index remained at lower value of 2.45 @ 1250 nm for the 100 nm thick film and it

increases to 2.6 @1250 nm when the thickness was increased to 350 nm. The behaviour was as expected; refractive index *decreases* at elevated substrate temperature [11]. This behaviour can be explained in terms of Penn gap [11,13] variations .

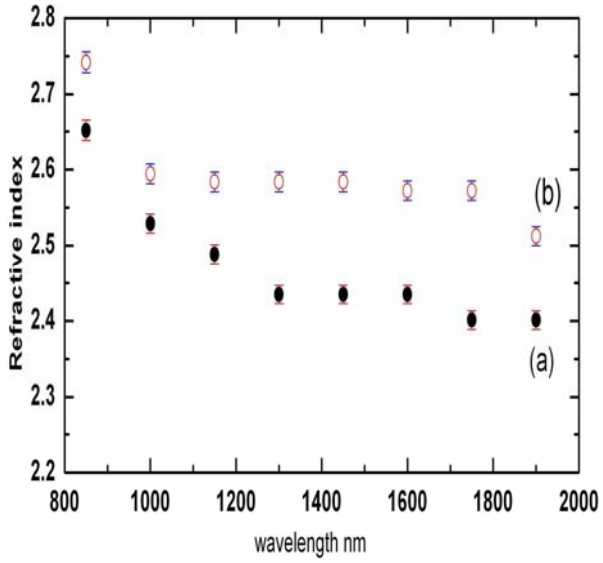

Figure 4.2.8 The refractive index of the a-Si thin films grown on glass substrate held at room temperature and thickness of (a) 100 nm and (b) 350 nm

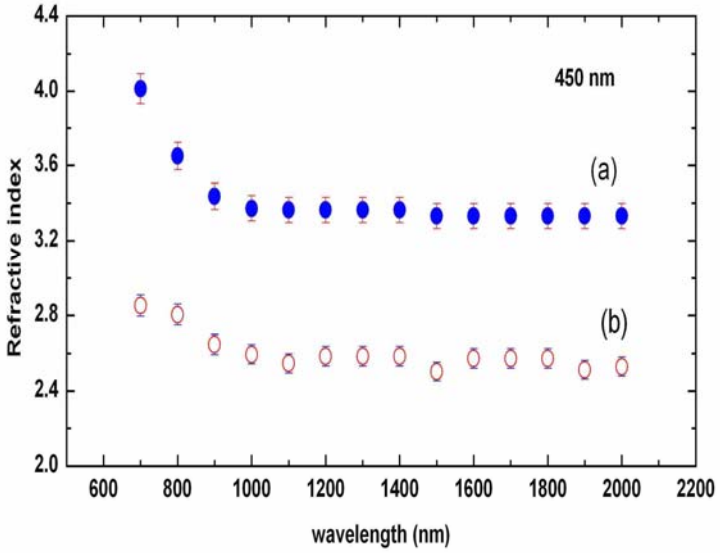

Figure 4.2.9 The refractive index of the 450 nm thick a-Si thin film grown on glass substrates held at two temperatures (a) room temperature and (b) 350 ^{o}C

in the films under investigation. When thin films are grown at elevated substrate temperatures, the films density is increases with close atomic packing resulting in greater Si-Si bond strength. The Penn gap is related to the bond strength, bond angle and coordination number in a-Si. Once the Si-Si bond strength increases, the Penn gap increases, resulting in the decrease of the refractive index. However, independent of substrate temperature, the refractive index has been observed to be increasing with the film thickness. When the films were grown on a substrate held at room/ambient temperature the impinging atoms of the evaporated substance do not possess enough energy to hop around in order to find a suitable place on the substrate in terms of free energy minima.

The energy, supplied by heating the substrate prior to the deposition and maintained through out the experiment covers the energy deficiency for the impinging atom to hop on the substrate. At a substrate temperature of 350 ^{o}C the silicon thin films grown on glass shows considerable increase in the refractive index. This can be attributed to the near tetrahedral coordination of a-Si and not because of the Penn gap increase, as it attains the bulk refractive index of 3.4 at 1200 nm [12].

4.2.3.2 Optical Absorption edges

The optical absorption coefficient, α of a-Si thin film evaporated onto a glass substrate held at room temperature is shown in Figure 4.2.10. The absorption coefficient is derived from optical transmission spectra after correcting for reflectivity. The absorption coefficient spectrum consists of three regions distinguished as (a) a power law regime (b) Urbach edge, where absorption coefficient depends exponentially on photon energy and (c) an absorption tail ascribed to the optical excitations from defects and disorder network.

The position and shape of the absorption spectra were found be dependent on the preparation methods and conditions. The power law regime is above 2.6 eV, where the $\alpha \propto (E\text{-}E_g)^r$, here E the photon energy E_g, is the band gap of the thin film and 'r' is an integer that represents the power. Below that we have the so-called Urbach edge regime, between ~1.95 and 2.75 eV. An absorption tail below 1.9 eV is ascribed to deep defect

states in the gap. The spectrum is similar to that of the a-Si: H except the energy region of the above mentioned three regions occur at comparatively low energies.

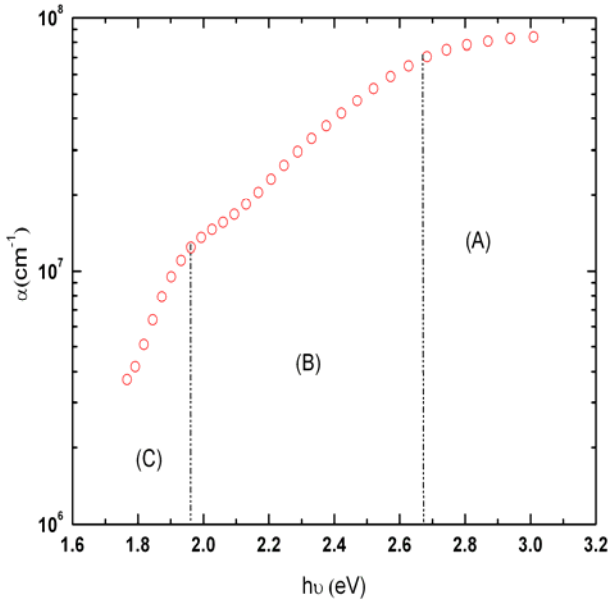

Figure 4.2.10 Absorption edge spectrum of evaporated a-Si thin film prepared at T_s =RT

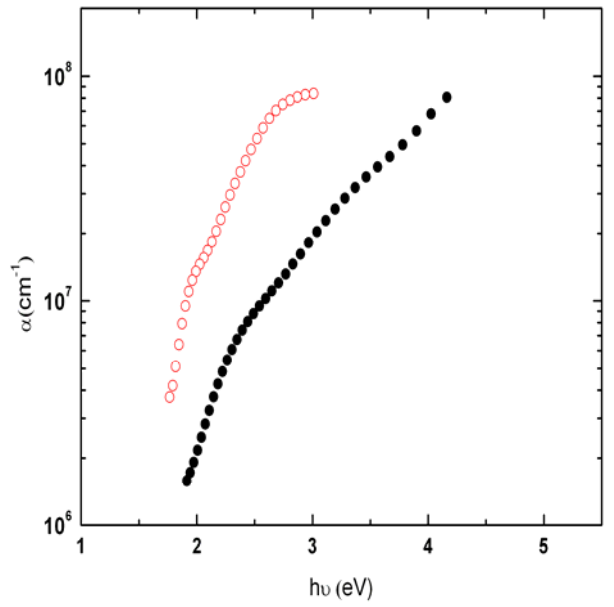

Figure 4.2.11 Absorption edge spectrum of evaporated a-Si thin film prepared at T_s =RT (*solid circles*) and T_s = 350 ^oC (*open circles*)

The optical absorption coefficient of a-Si films of thickness of 450 nm, deposited on a glass substrate held at room temperature and another held at 350 ^{o}C is shown in figure 4.2.11. The power law region starts above 4 eV for the film deposited on the substrate which was held at room temperature, whereas the other films shows the power law region at lower energies of 2.8 eV. This signifies the changes in the transition matrix element. The slope of the absorption coefficient is a measure of disorder. There are different kinds of disorders, which can broaden the absorption coefficient by creating energy levels deep into the forbidden gap.

4.2.3.3 Band gap Energy (E_g)

The optical band gap E_g, is defined as the energy difference between the bottom of the conduction band and the top of the valence band. A physically significant way to define the band gap was first given by Tauc *et al*. [14]. When we plot $(\alpha h\upsilon)^r$ vs hυ yields a curve whose linear part is extrapolated to the zero of absorption coefficient. Where, the extrapolated line meets the energy axis that determines the band gap energy. The integer 'r' is an indication about the nature of the transactions. Based on the 'r' value the nature of the transitions are determined.

Nature of the transition	**'r'**
Direct Allowed	1/2
Direct forbidden	3/2
Indirect allowed	2
Indirect forbidden	3

The absorption coefficient plotted in the form suggested by Tauc *et al* is shown in figure 4.2.12. The E_g obtained from this method depends on the energy region considered for the extrapolation [15, 16]. When the value of 'r' is 2 and 3 the transitions are known to be indirect allowed and forbidden transitions respectively. In the figure (10a) the transitions are assumed to be allowed indirect which is the usual nature found in the materials like Si which has indirect band gap.

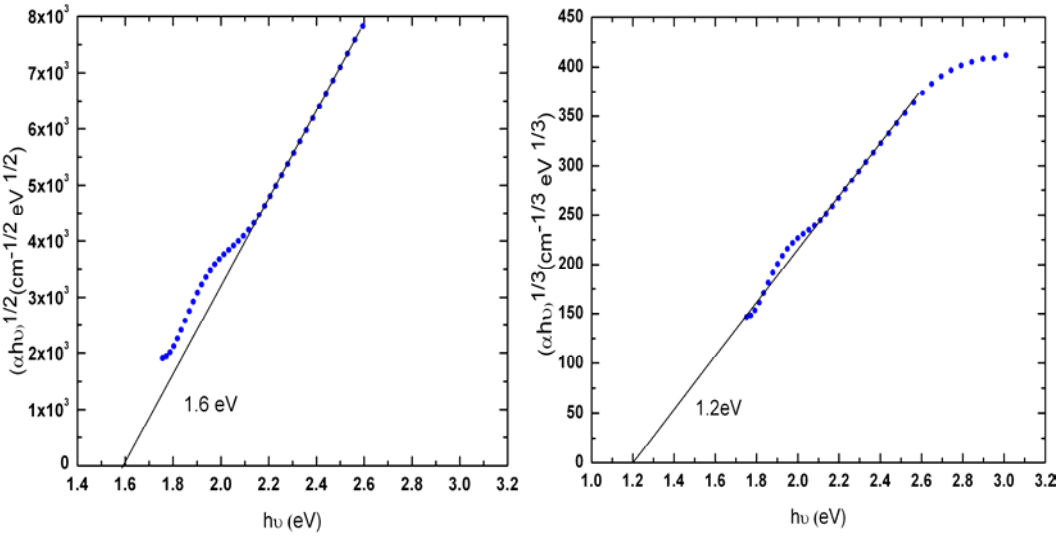

(a) (b)

Figure 4.2.12 The Tauc plots for values of r being 2 and 3.

The linear region in the plot $(\alpha h\upsilon)^{\frac{1}{3}}$ against hυ is small compared to the plot of $(\alpha h\upsilon)^{\frac{1}{2}}$. So the transitions are considered as allowed indirect. In our case the band gap value is 1.6 eV and when (b) the transitions are forbidden then the band gap is 1.2 eV. The list of the samples used for this study is given in the table 1 below. In our study all energy gap values quoted, correspond to r=2.

Table 1

Sample thickness (nm)	**Band gap (eV) r = 2**	**Band gap(eV) r = 3**
100	1.64	1.0
120	1.90	1.3
180	1.50	1.0
190	1.90	1.3
275	1.60	1.2
280	1.74	1.1
335	1.60	1.3
450	1.88	1.4

The figure 4.2.13 shows the band gap variation in a-Si thin film with substrate temperature effect.

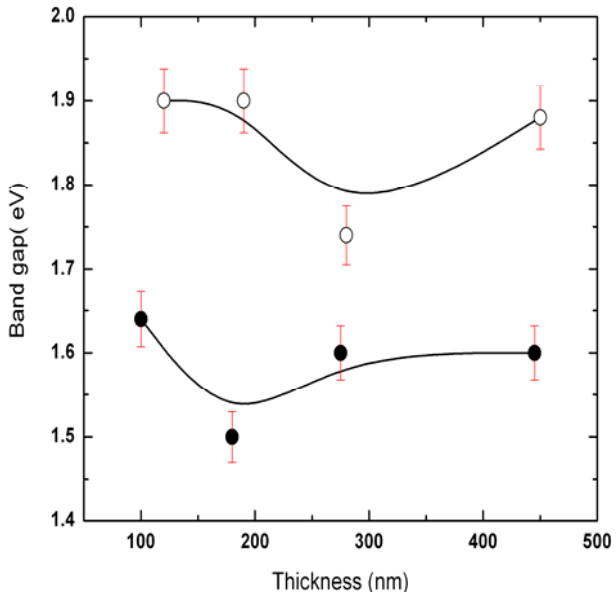

Figure.4.2.13 Band gap Variation of evaporated a-Si thin as a function of thickness deposited at Substrate temperature, T_s =RT (*closed circles*) and T_s = 350 ^{O}C (*open circles*)

We observed an increase in the band gap, with substrate temperature. When a-Si thin films are deposited on a substrate held at room temperature the band gap was 1.65 eV and at elevated substrate temperature it was 1.9 eV at a thickness of 100 nm. This increase in the band gap can be attributed to the quantum confinement of charge carriers in amorphous Silicon clusters. The presence of a-Si clusters is evidenced by Raman spectroscopy where the peak centered at 477cm^{-1} represents the a-Si cluster comprised of 200 atoms [2]. These amorphous clusters confine the charge carriers and in turn we observe an increase of 0.2 to 0.4 eV of band gap energy in a-Si. The over all increase of band gap in a-Si to 1.4 eV instead of 1.1 eV of crystalline Si is explained by *Skettrup* model [17].

4.2.4 *Optical properties of a-Si prepared by Ion beam sputtering*

Amorphous Silicon thin films were prepared by single ion beam sputtering using Ar^+ ions at 600 and 700 eV. The experimental details are given in the sample preparation section.

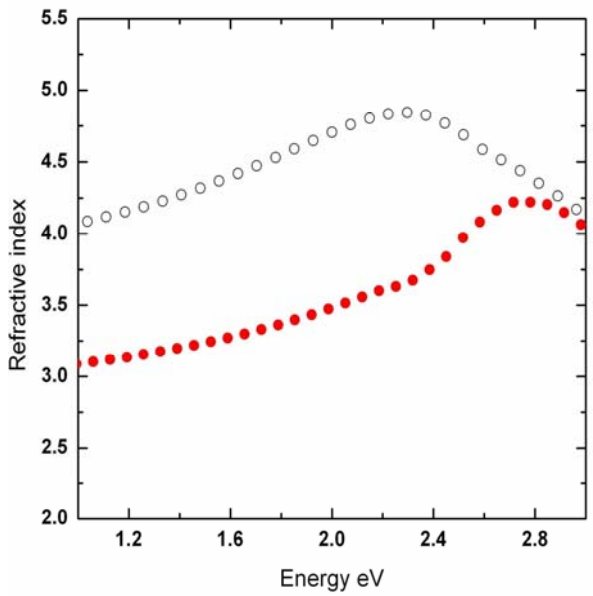

Figure 4.2.14 The refractive index behaviour of a-Si thin film of 100 nm thickness deposited at 700 eV (*open circles*) and 600 eV(*solid circles*) of incident ion beam energy

4.2.4.1 *Refractive index of Ion beam Sputtered a-Si*

The index of refraction, n of the a-Si thin film on glass deposited by ion beam sputtering exhibits a decrease with thickness. This decrease can be attributed to the increase in the Penn gap and with relaxation [11] of the strained amorphous network because, the deposition process involves, high energy ions. Typically, with an increase in the thickness, the deficiency in density will reduce resulting in bulk like refractive index values. When the thickness is increased from 30 nm to 130 nm the refractive index varied from 4.4 to 3.7 determined at 1.4 eV whereas bulk silicon possesses a value of 3.4 at 1.4 eV in the dispersion free region. The reported values of refractive index in unhydrogenated a-Si varies from 3.4 to 4.1[11,18]. The deviations in the values of n, are solely dependent on the method of preparation and conditions of the thin films and their thermal history. The refractive index was found to depend on the incident ion beam energy as shown in figure 4.2.14 for two films of the same thickness deposited at 700 and 600 eV indicating that there is increase in the refractive index with the beam energy.

These results are in good agreement with a-Si sputter deposited by Richards *et al.* [19]. The refractive index values reaches a maximum of 4.8 at 2.3 eV for the film deposited at 700 eV and 4.2 at 2.7 eV of the film deposited at 600 eV. The higher refractive index values than the crystalline Silicon (c-Si, n=3.41) for these films can be explained in terms of Penn gap. The Penn gap is a measure of average bond strength which in c-Si is 4.8 eV whereas in a-Si it decreases to ~3.7 eV due to the weakening of Si-Si bonds [20]. The reduced Penn gap values due to the amorphous nature of the silicon thin films results in the higher refractive index than the c-Si.

4.2.4.2 Optical Absorption edges

The optical absorption coefficient,α, of 30 nm thin film exhibits a small shoulder between 1.3 and 1.6 eV. This has been interpreted as rising from the maximum in the density of states [21]. This maximum in the density of states at such low energy is due to the divacancies [22] in a-Si that might correspond to the donor or acceptor levels of such divacancy defects. Once the thickness increases, defects might be saturated or the increase in the absorption coefficient shields these effects from being shown up in optical investigations.

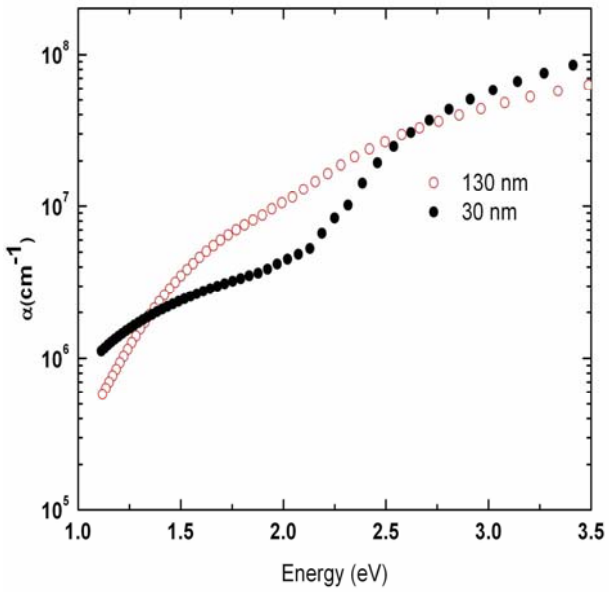

Figure 4.2.15 Optical absorption coefficient of ion beam sputtered a-Si thin films

Table 2.

Thickness nm	Band gap (eV)	E_U (meV)	ΔE_o (eV)	Refractive index
30	2	57	0	4.35
60	1.5	46	0.03	3.85
80	1.67	48	0.37	3.83
100	1.33	47	0.46	3.95
130	1.25	47	0.23	3.52

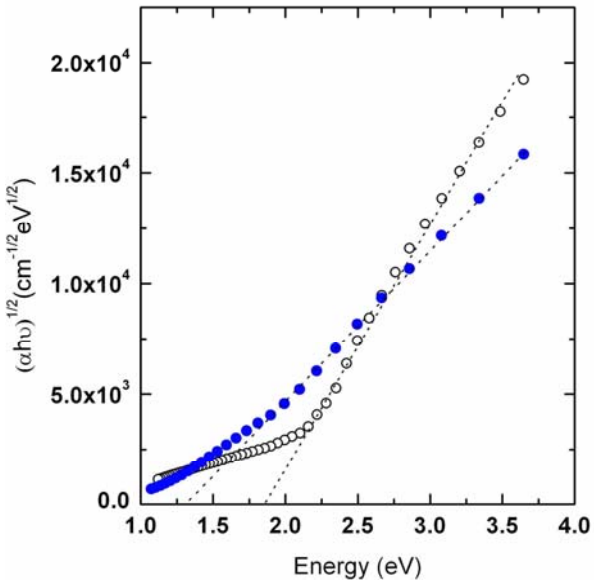

Figure4.2.16 Tauc gap of ion beam sputtered a-Si thin films of thickness 30 and 130 nm

4.2.4.3 Band gap Energy

The optical-absorption coefficient 'α' as a function of the photon energy for films of different thickness is shown in figure 4.2.15 and figure 4.2.16 depicts the plot of $(\alpha h\upsilon)^{1/2}$ vs. *E* in the absorption edge range. Extrapolating the linear region of the curve on to the x-axis gives the optical energy gap for the film thicknesses 30 nm and 130 nm, the band gap is 1.3 and 1.8 eV respectively. The so-deduced values of energy gap are reported in Table .2 as a function of thickness. The band gap decreases linearly with thickness and the thickest film of 130 nm reaches the band gap value of 1.3 eV.

With the increasing thickness of the film, the band gap energy decreases from 1.8 to 1.3 eV. This suggests that the density of the states is increasing with thickness resulting in decrease of band gap. The plot of ε_2 Vs photon energy for thin films of thickness 100 nm and 50 nm are shown in figure 4.2.17. These spectra are typical of amorphous Silicon. The variation of ε_2 as a function of photon energy is proportional to the convolution of density of valence and conduction band states separated by the band gap. In the figure, the dependence of ε_2 on energy is similar in both the films. But there are key differences in the magnitude and the peak position of ε_2 maxima. The magnitude of decrease is from 23 to 17 as the thickness decreased from 100 nm to 50 nm along with a red shift of ~0.6 eV in the peak maxima of ε_2. These changes and the increase of the area under the curve suggest an increase of density of states (DOS) with thickness. Assuming the conduction band states were constant, the increase in the density of states will result in redistribution of valence band states. In turn, the increase in DOS will decrease the band gap or vice versa. This fact is very well manifested in the figure 4.2.18 which shows that as the thickness increased, the band gap decreased monotonically.

Thus, before we study the metal induced crystallization in a-Si thin films we have studied the optical properties of a-Si thin films and was aimed to determine how they differ from the films reported in the literature. Amorphous Silicon prepared by thermal evaporation and ion beam sputtering, show similar optical properties in good agreement with available literature. Evaporated films suffer from low packing density and thus the optical properties when deposited on substrates held at elevated temperatures exhibit substantial improvement.

Being a high energy process, ion beam sputtered a-Si films display fundamental optical constants close to bulk silicon. The optical band gap of 1.2 eV for 130 nm thick films makes this material ideal for Solar cell applications. Thus, ion beam sputtered a-Si shows promise for the preparation of defect free a-Si for a variety of device applications where hydrogenated a-Si fails over a period of time due to degradation.

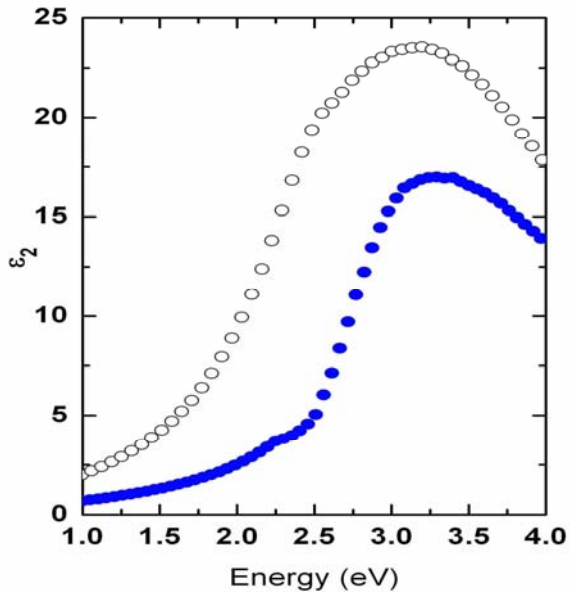

Figure 4.2.17 The plot of ε_2 Vs photon energy for a-Si thin films of thickness 50 nm (Solid circles) and 100 nm (open circles).

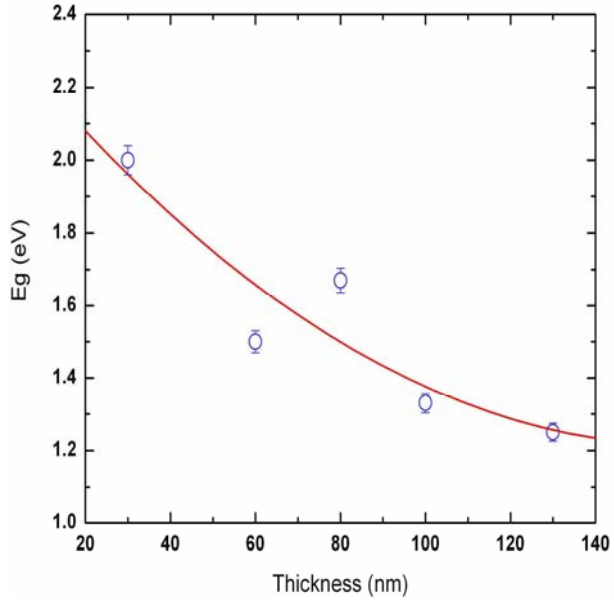

Figure 4.2.18 Variation of band gap with film thickness

4.2.5 Summary

In conclusion we have presented the fundamental optical properties of the a-Si prior to the crystallization and confirmed that the optical properties were comparable to the data available in the literature. Amorphous Silicon thin films prepared by ion beam sputtering

have lower defect density than the evaporated thin films. Therefore, we propose that ion beam sputtering can be a viable method to produce "ideal a-Si" for solar cell applications.

Reference:

1. A Iqbal and S Veprek *J. Phys. C: Solid state Phys*. **15** 377 (1982)
2. P. Melinon, P. Keghelian, B. Prevel, V. Dupuis, A. Perez, B. Champagnon, Y. Guyot, M. Pellarin, J. Lerme, M. Broyer, J. L. Rousset, and P. Delichere, *J. Chem. Phys.* **108**, 4607 (1998)
3. R. J Kobliska, and S. A Solin, *Phys. Rev. B* **8** 3799 (1973)
4. R. L. C. Vink, G. T Barkema, and W F van der Weg *Phys. Rev B* **63** 115210 (2001)
5. D. Pomerantz, *J. Appl. Phys.* **38** 5020 (1967)
6. C W Pearce and R G McMahon *J Vac. Sci. Technol.* **14** 40 (1977)
7. R Swanepoel, *J Phps E: Sci Instrum*, **16,**1214, (1983)
8. E G Birgin, I Chambouleyron, and J M Martínez, *Journal of Computational Physics* **151** 862. (1999)
9. S H Wemple, *Phys Rev B*. **7** 3767. (1973)
10. S H Wemple, and M DiDomenico *Phys Rev B* **3** 1338. (1971)
11. M H Brodsky R S Title K Weiser G D Pettit *Phys. Rev B* **1** 2632. (1970)
12. M A Green, and M Keevers, *Progress in Photovoltaics* **3** 189. (1995)
13. E C Freeman, William and Paul, *Phys. Rev B* **20** 716(1979)
14. J Tauc, R grigorrovichi, A Vancu *Phys. Stat. Sol* **15** 627. (1966)
15. G D Cody, B Abeles, C R Wrosnki, RB Stephens and B Brooks *Sol. Cells* **2** 227. (1980)
16. G K M Thutupalli and S G Tomlin *J Phys. C* **10** 467. (1977)
17. T Skettrup *Phys. Rev* B **18** 2622 . **(**1978)
18. E C Freeman W Paul *Phys. Rev B* **20** 716. (1979)
19. BS Richards A Lambertz AB Sproul *Thin Solid Films **460** 247* (2004)
20. JC Phillips *Rev.Mod.Phys.* **42** 290. (1970)
21. R J Loveland, W E Spear, A Al-Sharbaty *J. non. Cryst. Solids **13** 55* (1973/74)
22. J. W.Corbett, and G. D Watkins, *Phys. Rev* **138** A555(1965)

Optical Characterization

Nickel induced Crystallization in a-Si thin films

4.3 Nickel induced crystallization

4.3.1 Raman Spectroscopy of NIC

In this section the results of the Raman spectroscopy studies on the a-Si thin films crystallized by Ni induced crystallization are discussed. As described in the sample preparation section (Section 2.1), a-Si thin films were grown on glass substrates by thermal evaporation. An over layer of Ni of 50 nm thickness was evaporated on to the a-Si thin film. A schematic of the Ni/a-Si/glass stacks is shown in figure 4.3.1. These stacks were annealed at 600 ^{O}C for 15 minutes. A confocal micro Raman spectrometer is employed to investigate the structural properties of the film along with presence of different phases.

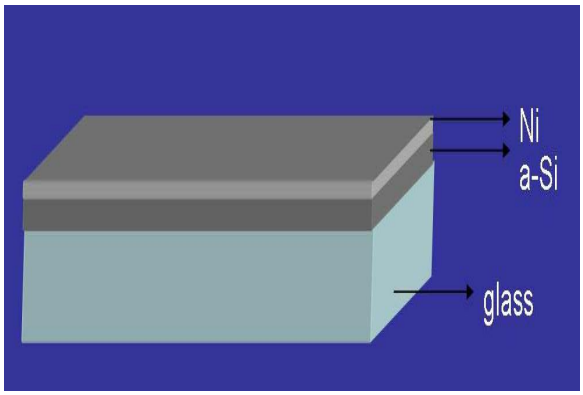

Figure 4.3.1. Schematic diagram of Ni/a-Si/glass thin film stack

Micro-Raman spectrometer with a confocal microscopic objective allows the recording of selected area Raman spectra with 1μm laser spot size illuminating the sample. The concentration of Ni inside the a-Si thin film was varied by varying the thickness of the a-Si thin film. The thickness of the Si films was varied from 100 to 1100 nm, which resulted in variation of the relative concentration of Ni from 50% to 4.5 %. Raman spectra recorded using a micro-Raman spectrometer with a laser wavelength of 514 nm, in the back scattering geometry, are shown in figure 4.3.2. The peak at 474 cm^{-1} was assigned to be due to transverse optical (TO) phonons of amorphous silicon [1]. After conventional furnace annealing at 600 ^{o}C for 15 min, Raman peak with central frequency at 514 cm^{-1} was observed for the Ni doped Si films with a relative Ni concentration of

4.5%. It is well known that a-Si and crystalline silicon (c-Si) have their Raman frequencies centered at 475 and 520 cm^{-1} . The Raman central frequency at 520 cm^{-1} is the silicon's first direct transition, $\Gamma'_{25} - \Gamma_{15}$ at 3.3 eV, a feature that has also been observed in specular reflectance curves shown later. A significantly downshifted and asymmetrically broadened Raman peak centered at 514 cm^{-1} was attributed to the nanocrystalline silicon having a crystallite size of 6 ± 2 nm.

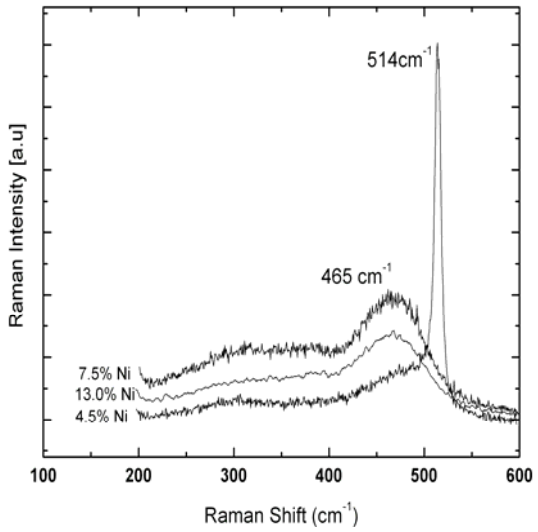

Figure 4.3.2 Raman Shift of the a-Si thin films annealed at 600 ^{O}C for 15 minutes with varied Ni concentration from 4.5 to 13%.

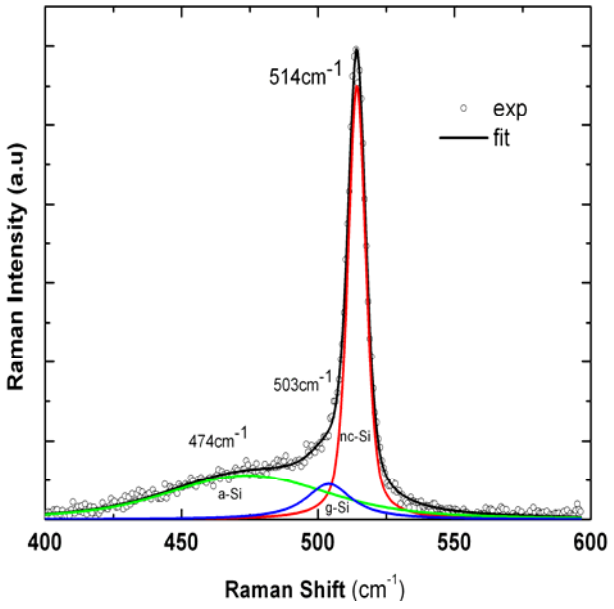

Figure 4.3.3. Raman spectra from a-Si thin film containing nc-Si after annealing at T = 600 ◦C with 4.5% of Ni. Individual components from amorphous (474 cm^{-1}), nanocrystalline (514 cm^{-1}) and grain boundaries (503 cm^{-1}) are deconvoluted.

The onset of crystallization of a-Si occurs at 4.5 % of Ni concentration. Nanocrystallinity and quantum confinement have been reported in silicon of many forms, such as Si nanowires, quantum dots and in systems where the lateral dimensions are down to 15 nm [2, 3]. Ritcher *et al* proposed a model for quantum confinement, and Campbell *et al* [4, 5] developed it further. This model has come to be known as the RCF model or phonon confinement model. Pisanec *et al* [6] further improved the model by accounting for the Raman peak position and width to the size and morphology of the nanocrystalline material. According to Schubert *et al* [7], the measured line shape of the Raman signal comprises four different contributions, namely from amorphous, polycrystalline, grain boundaries and nanocrystalline components present in the sample. The whole signal is deconvoluted into individual contributions as shown in figure 4.3.3. It is evident from figure 4.3.1 that in the Ni induced crystalline sample the contributions from three components can easily be identified. It should be noted that films annealed at temperatures < 600 ^{o}C and higher concentrations of Ni did not show any evidence for crystallinity in the Raman spectra.

Apart from the Si characteristic Raman peaks, the samples consist of silicide compounds when the Ni concentration reaches the level of alloy. However, metal silicides have Raman active vibrations at very low frequencies, near 200 cm^{-1}. The vibrations are relatively weak in intensity to be observed at room temperature. Figure 4.3.4 shows some silicide signatures in our films. $NiSi_2$ formed in a-Si thin film with 50 % of Ni. Other phases of nickel silicides are not observable in our films. The nickel silicides move towards the bottom of the film while annealing. Therefore the more intense peak belonging to $NiSi_2$ could not be observed even at 50 % of Ni in the Si thin film. This $NiSi_2$ layer formation and its drift towards the substrate is evidenced during the study of optical properties. The refractive index shows an anomalous dispersion because of the $NiSi_2$ phase near to the substrate. This particular behavior of refractive index is explained later in the chapter in section 4.3.6.

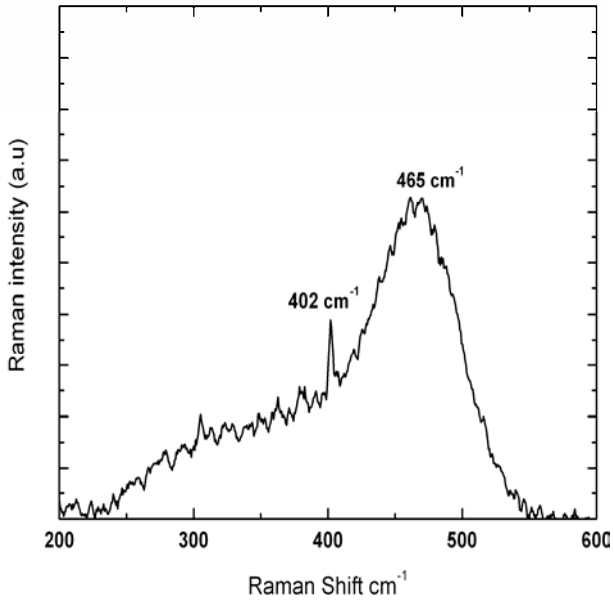

Figure 4.3.4. Raman spectra of $NiSi_2$ formed at 600 ^oC on glass substrate.

While reacting with Silicon, Ni forms many crystallographic phases, among them nickel rich phase Ni_2Si is and high resistivity phase. The Ni_2Si phase will form at temperatures around 200 ^oC. At 350 ^oC, a low resistivity phase NiSi will form and at elevated temperatures of 750 ^oC, $NiSi_2$, again a high resistivity phase will form. However, Cammarata [9] suggested that $NiSi_2$ is the only phase of nickel silicide formed by annealing if Ni is within, instead of at the top of a-Si thin film. Instead, we have observed $NiSi_2$ phase formation, when Ni blanketed the a-Si thin film. Lee and co-workers, [10, 11] have used micro Raman Spectroscopy successfully in the characterization of Ni silicides for the purpose of identifying the Ni_2Si, NiSi, and $NiSi_2$ phases.

Nickel silicide	**Active Raman frequency**
NiSi	195, 214 cm^{-1}
$NiSi_2$	232, 297, 320, **402** cm^{-1}

The Raman frequency at 402 cm^{-1} [12] is the signature of the $NiSi_2$ phase in side the film. But at the 50% of Ni concentration, the a-Si thin film remained amorphous in spite of silicide formation. This is contrary to the argument that in Ni induced crystallization; $NiSi_2$ seeds the nucleation for a-Si to recrystallize. From the above observation it seems

that the $NiSi_2$ role in a-Si crystallization is not really clear. However, at low concentrations of Ni, (4.5%) it crystallizes the a-Si thin film. The nanocrystallization was observed as shown in figure 4.3.3. ***This observation supports and strengthens our argument that crystallization is not mediated by silicides alone, instead the major role is played by Ni metal atoms.*** Optical microscopy reveals the surface morphology of these films after annealing at 600 ^{o}C for 15 mints. The surface morphology of the a-Si which becomes nanocrystalline after annealing is shown in the figure 4.3.5.

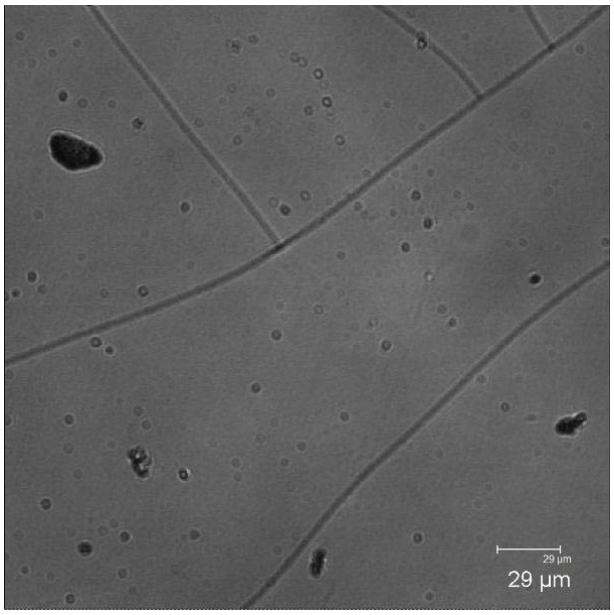

Figure 4.3.5 Optical micrograph of nanocrystalline Silicon

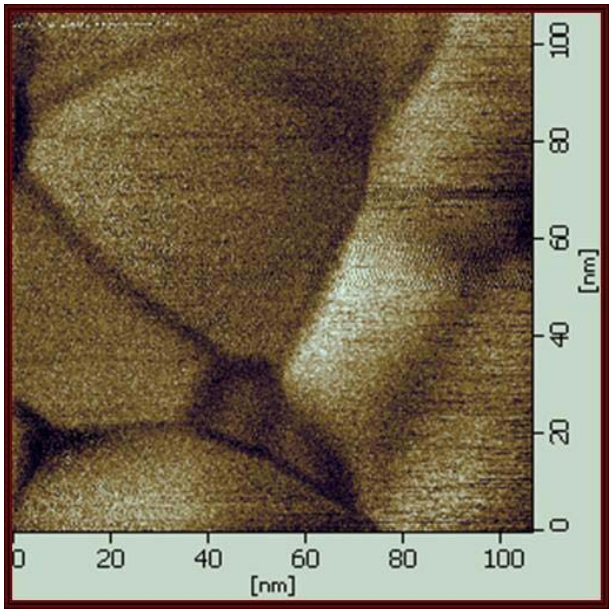

Figure 4.3.6 AFM phase image of nanocrystalline Silicon
Crystallized by NIC at 600 ^{o}C .

From the figure 4.3.5 the surface of the film looks quite smooth at optical wavelengths. This smoothness will be a positive feature for application of MIC crystallized Si in to solar cell applications. Further in this chapter, we have shown the optical absorption coefficients measure up to an order of 10^{6} cm^{-1}. Though the film shows some cracks and saucer pits, the optical properties are promising at this stage. Further studies on electrical properties will give a complete idea of the scenario.

In order to understand deeply the morphological features we have used atomic force microscopy (AFM). AFM measurements are made in air with a silicon tip of force constant 3.0 N/m. An average grain size of ≈ 60 nm was observed for the nanocrystalline Silicon thin film, the same film shown in the figure 4.3.5, its AFM image is shown in figure 4.3.6. The AFM image again shows smooth surface with grain sizes on average 60 nm with well defined grain boundaries.

In conclusion, we have observed nanocrystallization in a-Si thin films with 4.5% of Ni, annealed at 600 ^{o}C for 15 minutes. From Raman spectroscopy it is evident that, with in 15 minutes of annealing Si thin films crystallizes but still certain amorphous component remains un-crystallized. The Raman peaks are modeled with Voigt like function and the

contribution of a-Si, nanocrystalline and grain boundary scattering to the Raman spectra has been clearly established. The crystallite size was 6 ± 2 nm estimated by Zi model. Only $NiSi_2$ silicide phase was observed in the thin films where the Ni concentration is nearly 50%.

4.3.2 Optical properties of Ni/a-Si/glass systems

A survey of literature shows that a detailed study of the optical properties of Ni doped crystalline Si by the MIC process is lacking. The refractive indices of the Ni doped Si films are not known and it is also not very well understood whether the optical band gap is affected due to the MIC process. Furthermore, it is not clear whether the diffusion of Ni in to Si causes optical inhomogeneities. The variation in band structure due to the MIC process has also not been studied in detail. It is important to understand these properties of MIC-Si since most of the applications envisaged are photonic or opto-electronic in nature. The motivation of the current work is, therefore, to understand the evolution of optical properties such as spectral transmission, specular reflectance, refractive index and band gap as a function of processing parameters and thickness of a-Si films doped with Ni during crystallization

4.3.3 Spectral transmission

The spectral transmission spectra of undoped a-Si thin film and doped annealed at 600 ^{o}C for 15 minutes are shown in Figure 4.3.7. Before and after annealing the transmittance of the films in the dispersion free region at the wavelength range of 1000 to 2500 nm remained at approximately 90 %. However, the refractive index seems to be more affected due to Ni inclusions near the absorption edge. A detailed study of refractive index behavior of Ni doped a-Si thin films is given in further sections.

4.3.4 Optical absorption coefficient

The optical absorption edge as a function of thickness and substrate temperature is shifted towards longer wavelengths or lower energies with a small variation in the refractive index. The shift can be due to small amorphous Si clusters, oxygen bonds on the surface formed during annealing and may also depend on the micro voids formed during growth. However, for a constant thickness of 450 nm of a-Si thin film, the shape of absorption edge, apart from a small increase in the absorption coefficient, is similar both for the films deposited on substrates maintained at ambient temperature and at 350 °C during deposition as shown in Figure 4.3.8. Also shown in the same figure is the absorption coefficient for a sample doped with 10 % of nickel and annealed to 600 ^{o}C after deposition. The a-Si film (fig. 4.3.8(a)) deposited at ambient temperature showed a broad edge, with absorption coefficient about 10^6 to 10^7 cm^{-1}. The undoped a-Si deposited at 350 °C (fig. 4.3.8(b)) of substrate temperature also displayed a similar broadening in the absorption edge but with larger absorption coefficient, which might be attributed to the changes in the transition matrix element. The sample doped with nickel (fig. 4.3.8 (c)) had a relatively sharp edge, with a three orders of magnitude increase in its absorption coefficient. The increase in the absorption coefficient can be attributed to the Ni metal component present in the sample but the slope of the edges signifying the role of Ni in catalyzing the crystallization in silicon is quantified by Urbach energies.

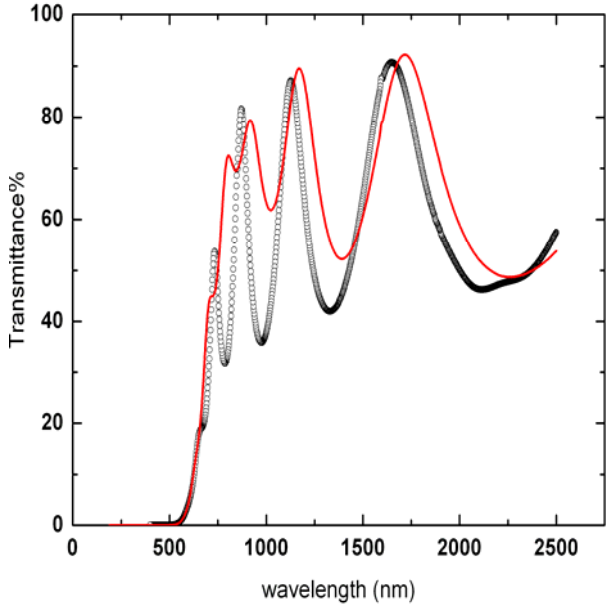

Figure 4.3.7 Spectral transmission of 650 nm a-Si thin film undoped (*open circles*) annealed at 600^{O}C for 15 minutes with a 50nm of Ni top layer (*solid line*)

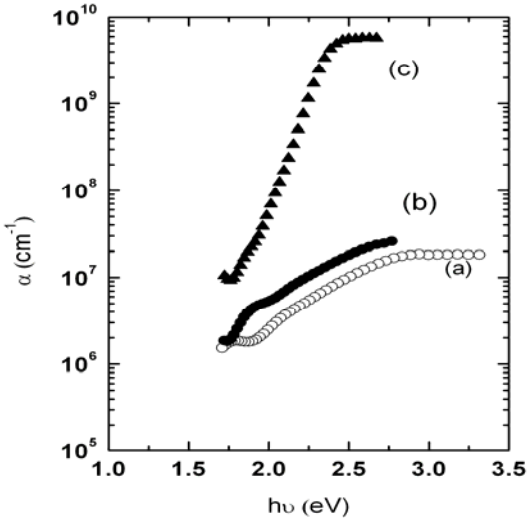

Figure 4.3.8 Absorption Coefficient of 450 nm thick sample deposited at (a)RT and (b) at Ts=350 °C along with (c) thickest sample of thickness of 1100 nm with Ni doped and annealed.

4.3.5 Band gap Energy

The appropriate parts of the absorption coefficient were fitted to the following equations.

$$(\alpha \hbar \upsilon)^{\frac{1}{2}} = B^{\frac{1}{2}}(\hbar \upsilon - E_{tauc}) \qquad \ldots\ldots\ldots\ldots\ldots\ldots (4.3.1)$$

$$\alpha = \alpha_o \exp\left(\frac{E_o - \hbar \upsilon}{E_u}\right) \qquad \ldots\ldots\ldots\ldots\ldots\ldots (4.3.2)$$

Where, E_U is Urbach energy, and $B^{1/2}$ is Tauc parameter. Assuming parabolic valence band and conduction band, the Tauc gap (E_g) is determined by plotting $(\alpha h\upsilon)^{1/2}$ against ($h\upsilon$) and extrapolating the linear region of the curve. The dependence of Urbach energy, E_U, on different concentrations of Ni is plotted in figure 4.3.9. The Urbach slope increases with introduction of Ni metal in to the a-Si film, both in the doping and alloy regime and up to 4.5 % of Ni doping the E_U increased without affecting the E_{Tauc}. The slope of the absorption edge measures the degree of order and clearly the degree of order is dependent on the Ni concentration in the films.

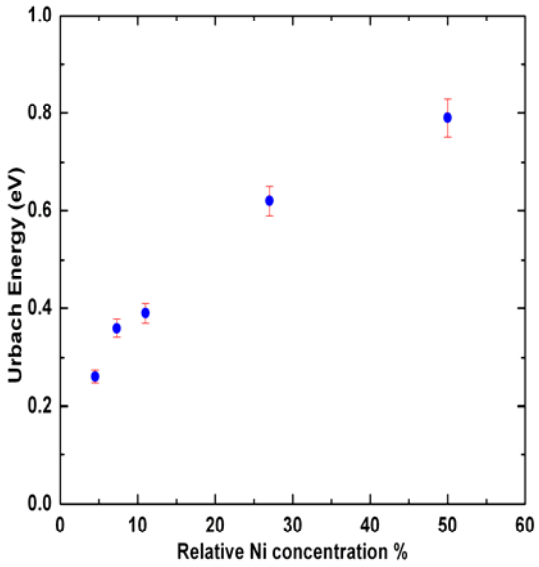

Figure 4.3.9 Urbach slope as a function of Ni concentration

Urbach edge energy increases with Ni concentration as shown in figure 4.3.9 and these results are in agreement with Al doped a-Si :H system [13] where 12 % of Al in a-Si:H

was investigated. However no crystallization was reported. At lowest Ni concentration of 4.5 %, the a-Si films, crystallizes and show small Urbach energies, which is a manifestation of the definition of Urbach edge that is as a measure of disorder. The films showed a variation in the band gap from 1.6 to 1.89 eV. These values demonstrate the possibility of tailoring the band gap of MIC silicon over a wide range of values. Another interesting feature is that the band gap of the annealed undoped and doped Si films displays very little variation in their values in spite of the annealing process.

In the high absorption region α can be represented by the relation, given by Eq 4.3.1. Where B is constant depending on the transition probability, E_g is the band gap and p is an index that characterizes the optical absorption process and is theoretically equal to 2, 1/2, 3 or 3/2 for indirect allowed, direct allowed, indirect forbidden and direct forbidden transitions respectively. The usual method for determining the value of the band gap, Eg , involves plotting a graph of $(\alpha h\upsilon)^{1/p}$ versus photon energy, E, in accordance to Eq (4.3.1). If an appropriate value of p is used to obtain linear plot, the value of Eg will be given by the intercept on the E axis. To apply this relation for the sample under investigation, $(\alpha h\upsilon)^{1/2}$, $(\alpha h\upsilon)^{2}$, $(\alpha h\upsilon)^{1/3}$ and $(\alpha h\upsilon)^{2/3}$ as function of E are plotted and illustrated in Fig. 4.3.10 (a), (b), (c) and (d), respectively. As could be seen from the figure, the best plot that covers the widest range of data is obtained for the $(\alpha h\upsilon)^{1/3}$ – E dependence . The hυ axis interception being ~1.93 eV indicates the indirect forbidden transitions domination in amorphous Si thin films. The figure 4.3.10 sheds light on the various probable transitions in Silicon thin films. If we take a closer look at plots (a) and (b), the linear portion of absorption edge coves almost similar energy range of 1.7 to 2.5 eV. Thus, in these particular films the optical transitions are indirect allowed and forbidden respectively. Intrinsic Silicon is an indirect band gap material and thus posseses $(\alpha h\upsilon)^{1/2}$ dependence. Klazes et al. [14] suggested a dependence of $(\alpha h\upsilon)^{1/3}$ for a-Si films. But this 1/3 dependence, in majority of cases gives small band gap value for Si. Our findings are in good agreements with Naggar et al. [13] in the case of Al doped a-Si :H.

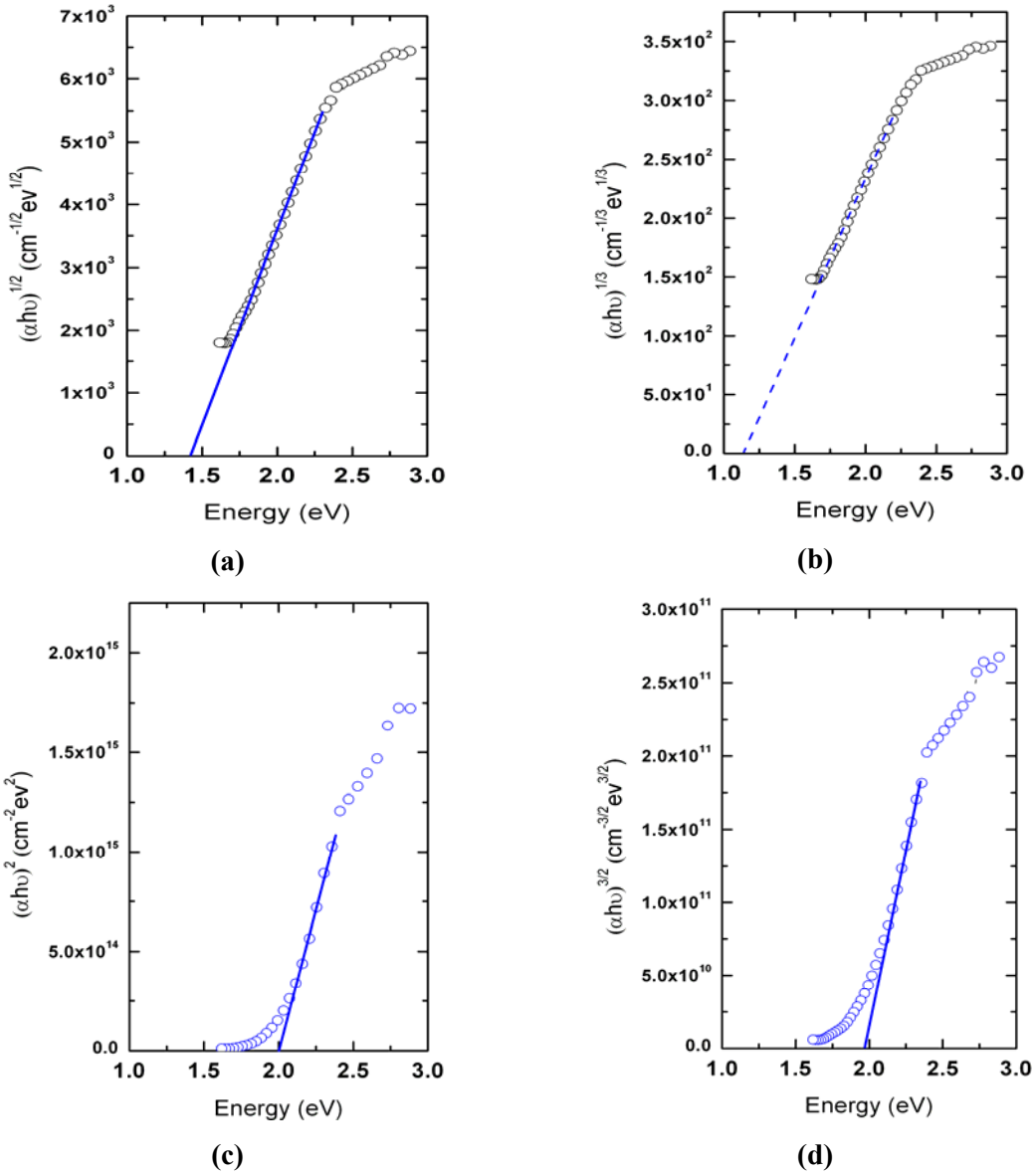

Figure 4.3.10 Plots of $(\alpha h\upsilon)^{1/p}$ as function of $h\upsilon$ for p values being 2, 1/2, 3 and 3/2 for a-Si thin films.

Rogachev *et al.* [15] have noticed a decrease in the band gap after addition of 5% atomic percentage of Ni. We have studied Ni percentages up to 50% and no band gap variation with Ni inclusions was noticed.

4.3.6 Refractive index behaviour

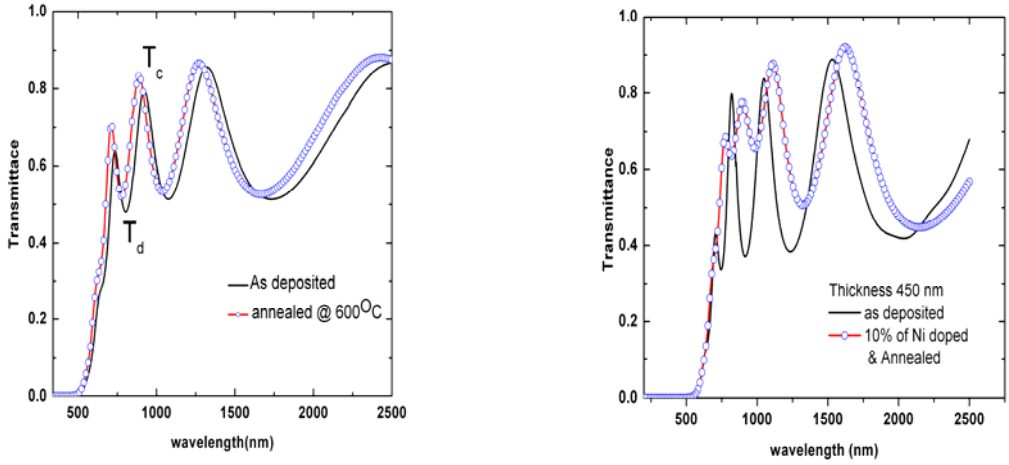

(a) (b)

Figure 4.3.11 Spectral transmission spectra of As-deposited a-Si thin films along with annealed at 600 ^{o}C (a) with out Ni (b) with a Ni over layer of 50 nm

The effect of Ni doping on the system has also been studied using the spectral transmission curves as shown in figure 4.3.11. The spectral transmittance of the pure a-Si films as deposited and those annealed at 600 °C are shown in figures 4.3.11(a). The spectral transmittance for the films doped with a Ni concentration of 11 % and annealed is shown in figure 4.3.11(b). It is evident from the figures that while the positions and the absolute values of transmittance at points of constructive and destructive interference (indicated by T_c and T_d respectively in the figure 4.3.11(a) do not vary significantly as a result of annealing in the undoped Si films, for the Ni doped films there is a significant change in the features of the transmittance spectra. The first significant deviation in behavior is that the T_d values in the case of the doped films are wavelength dependent. For a completely optically homogeneous film, the T_d and T_c values remain constant in the dispersion free region of refractive index, as observed in figure 4.3.11(a) [8]. However, for optically inhomogeneous films both the values and the wavelengths at which T_c and T_d occur will differ from that of the corresponding homogeneous film. Optically homogeneous films are those that possess thickness and wavelength independent

refractive indices in the dispersion free region of the spectrum. The origin of inhomogeneity can be traced to the structural, microstructural and chemical inhomogeneities along the thickness (i.e. the cross-section) of the film. Such a film is modeled as having a wedge shape rather than the flat parallel faces that is assumed for homogeneous films. A schematic of this is shown in figure 4.3.12.

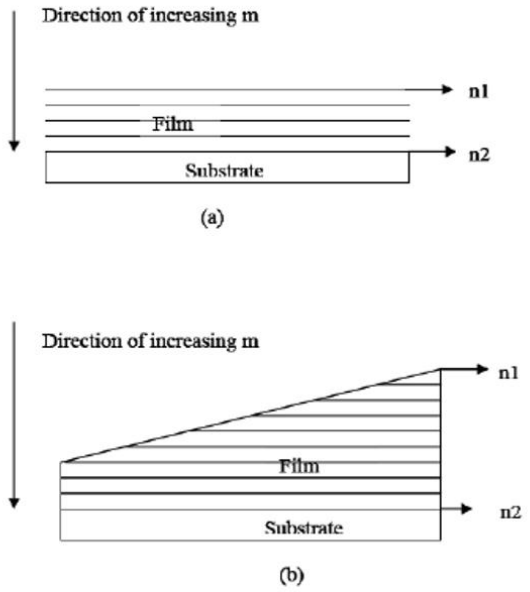

Figure 4.3.12 (a) Schematic of a optically homogeneous thin film showing the increasing order of interference, m, and refractive indices n1 and n2 at the film-air and film substrate interfaces respectively. Here n1 = n2. (b) Schematic of a optically inhomogeneous thin film showing the increasing order of interference, m, and refractive indices n1 and n2 at the film-air and film substrate interfaces respectively. Here $n1 \neq n2$.

The inhomogeneous film can then be further modeled as a multilayered structure consisting of several interfaces each of which has a different refractive index at a given wavelength. This leads to a film with a gradient in refractive index across its cross-section of thickness rather than a single refractive index for the entire cross-section at a given wavelength as is the case for homogeneous films.

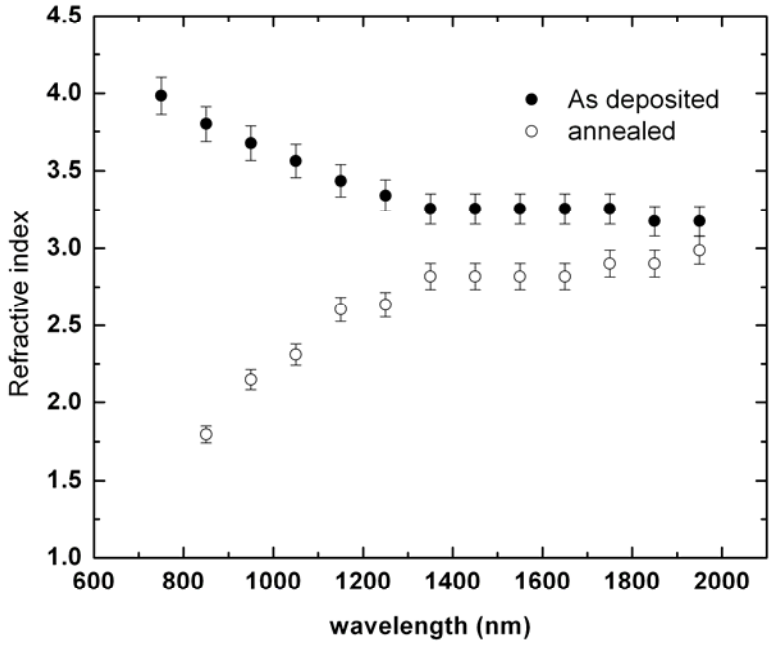

Figure 4.3.13 Variation in the refractive index due to Ni content and annealing as a function of wavelength (λ).

The calculated dispersion in refractive index 'n' for the a-Si films with and with out Ni is shown in figure 4.3.8. The dispersion for the annealed undoped Si film shows the idealized behavior with increase in refractive index in the region of the band gap and constant value in the dispersion free region between 1200 to 2500 nm. The nickel doped film, on the other hand, shows anomalous behavior in the dispersion of refractive index. It exhibits a decreasing refractive index in the region of the band gap while remaining constant in the dispersion free region. The decrease in refractive index is accompanied by an increase in absorption coefficient, which indicates that the contribution to the refractive index in this region is from the other component of the films such as metal or metal silicides.

Since, in the dispersion free region, the refractive indices of the undoped and doped films are 3.4 and 3.2 respectively, these values originate from the un reacted Si components of the film. The value compares favorably with that of crystalline Si films and can therefore be attributed to the unreacted nanocrystalline Si component of the film. The contribution

of the metal silicide clearly affects the region of the band gap and therefore the band structure. That this is a consequence of the diffusion process can also be inferred from the condition for constructive interference

$$2nd = m\lambda \qquad \text{..... (4.3.3)}$$

where 'n' is the refractive index of film of thickness 'd' at a wavelength 'λ' and 'm' is the order of interference. The left hand side of Eq (4.3.3) is also known as the optical thickness. The order of interference, m, increases with decrease in wavelength and more importantly the interference at higher values of m originates closer to the substrate-film interface than the film air interface. Based on this argument, from the spectral transmission curves in figure 4.3.11 and the dispersion curve in figure 4.3.13, it is clear that Ni diffusion occurs from the surface in to the bulk of the film. During the process of diffusion, the Ni catalyzes the crystallization process as Si atoms migrate to the surface. As a consequence, there is optical inhomogeneity in the film characterized by anomalous dispersion in the refractive index. It would thus appear that most of the crystalline Si is on the surface of the film and that the majority of the Ni diffuses in to the bulk. This would also explain the lack of crystallinity in films doped with relatively larger concentrations of Ni (>5%). Secondly, it would appear that in the case of the evaporated films the crystallization is driven by the rate of reaction at the interface rather than the diffusion process and hence the crystallization occurs within the first 15-20 minutes of the annealing process. The diffusion process dominates thereafter, since further annealing does not improve the crystallanity in the current case.

4.3.7 *Summary*

In conclusion, we have presented the a-Si-Ni thin film system optical properties while varying the Ni concentration from 4.5 to 50%. The refractive index varies substantially after annealing. The variation in the refractive index as a function of wavelength was explained in terms of in- homogeneity developed in the film due to nickel silicide, $NiSi_2$ formation and its movement towards the substrate was evidenced in figure 4.3.12. These thin films will find application wherever a gradient of refractive index is necessary. The band gap is found to be unaltered after 50% of Ni has been added to Silicon thin film. After annealing at 600 ^{O}C Silicon thin films were nanocrystalline. Our experiments have

opened a new possibility to tune the crystallite size and optical band gap with the aid of Ni concentration and annealing.

Reference:

1. M H Brodsky, M Cardona and J J Cuomo *Phys. Rev.* B **16** 3556 (1977)
2. Z Iqbal and S Veprec *J. Phys. C: Solid State Phys.* **15** 377 (1982)
3. P Mishra and K P Jain *Phys. Rev. B* **64** 073304(2001)
4. H Richter and L Ley *J. Appl. Phys*. **52** 7281(1981)
5. I H Campbell and P M Fauchet *Solid State Commun.* **58** 739(1986)
6. S Pisanec, M Contoro, A C Ferrari, J A Zapien, Y Lifshitz, S T Lee, S Hofmann and J Robertson *Phys. Rev. B* **68** 241312(R) (2003)
7. E Schubert, J Fahlteich, B Rauschenbach, M Schubert, M Lorenz, M Grudmann and G Wagner *J. Appl. Phys.* **100** 016107 (2006)
8. Uma Mahendra Kumar, Brahma, M Ghanashyam Krishna, A K Bhatnagar and G Dalba *J. Phys.: Condens. Matter* **19** 496208 (2007)
9. R C Cammarata, C V Thomson, K N Tu *Appl. Phys. Lett* **51** 1106(1987)
10. P. S. Lee, D. Mangelinck, K. L. Pey, Z. X. Shen, J. Ding, T. Osipowicz, and A. K. See, *Electrochem. Solid-State Lett*. **3**, 153 (2000)
11. P. S. Lee, K. L. Key, D. Mangelinck, J. Ding, D. Z. Chi, J. Y. Dai, and L. Chan, *J. Electrochem. Soc*. **149**, G331 (2002)
12. F. F. Zhao, S. Y. Chen, Z. X. Shen, X. S. Gao, J. Z. Zheng, A. K. See, and L. H. Chan, *J. Vac. Sci. Technol. B* **21**, 862 (2003)
13. Ahmed H El-Naggar and Assem M Bakry *J. Phys.: Condens. Matter* **11** 9619(1999)
14. R H Klazes, M H Van Den Broek, J Bezemer and S Radelaar *Phil. Mag. B* **45** 377(1982)
15. N A Rogachev, V Smid, J J Mares and J Kristofik *J. Non-Cryst. Solids* **97/98** 955 (1987)

Optical Characterization:

Chromium Induced Crystallization in a-Si thin films

4.4 Chromium Induced Crystallization

Apart from the cubic form, there are 12 other known polymorphs of Silicon. Among them a few are stable only at high pressure and high temperatures. Hexagonal-wurtzite Silicon is one such structure and there have been very few reports in literature on its stabilization either in bulk or thin form at ambient pressure and temperature conditions. Very little is known about the optical properties such as transmission, refractive index and optical band gap of the wurtzite structured Si films. Chromium induced nanocrystallization of Silicon has been very sparsely reported previously although crystallization induced by metals such as Al and Ni have been extensively reported. It is known that in many silicides the metal-silicon bond length is very similar to that of Si-Si bond lengths in the wurtzite structure. Furthermore, in the process of metal induced crystallization of Si, both the metal and metal silicides that form as a consequence of the thermal treatment, act as nucleating agents for the crystallization of Si. The eventual structure of the Si nanocrystals, then, closely mimics that of the metal silicide. The choice of Cr was, therefore based on the premise that its silicides under favourable thermodynamic conditions could result in the formation of the wurtzite structure.

The objectives of this part of the work are therefore to study the possibility of stabilizing the wurtzite structure of Si in thin film form by the metal induced nanocrystallization route. To the best of our knowledge, this is the first experimental evidence of metal induced crystallization of Si into the wurzite structure. A further objective is to study the optical properties such as spectral transmission, refractive index and optical band gap of the wurtzite form of Silicon thin films.

4.4.1 *Raman Spectroscopy of CrIC*

Different structural studies on chromium silicides have reported the occurrence of crystallization of a-Si. In 1980, in their studies of compound formation between a-Si and chromium, Yacobi *et al.* have observed formation of $CrSi_2$ and subsequent crystallization of a-Si. [1]. Phillips *et al.* have also observed Si crystallization [2] in their studies of degradation of $CrSi_2$ micro lines. As in the case of Ni induced crystallization, the Silicide offers a seed for a-Si crystallization, it can be reasonably expected that the same

phenomenon would occur in the Cr case also. Furthermore, from the structural point of view $CrSi_2$ has hexagonal structure with the lattice parameters a = 0.4428 nm and c = 0.6363 nm and the lattice mismatch between $CrSi_2$ (0001) and Si (111) is only 0.14%. This property has earlier been exploited to grow $CrSi_2$ epitaxially on Si. However, in the current study, this would lead to an understanding of MIC and illustrating the competition between the role of silicides and metals atoms in the crystallization process. In the case of Ni induced crystallization EXAFS results gives support to the idea that metal atoms play the dominant role, but still more insight is necessary. However, comments by Lee *et al.* [3] on the lateral crystallization of a-Si aided by electric field give support to the argument that diffusing metal species is responsible for the crystallization of a-Si. In the Cr case the diffusing species is not the metal, instead [4] Silicon itself. In either case metal atoms mediate the bond breaking and making between Si-Si atoms. The metal silicides are an unavoidable by-product of the diffusion process.

In these studies, varying the a-Si film thickness from 80 nm to 600 nm varied the relative concentration of Cr metal from 37 % to 5 %. After annealing the Cr/a-Si/glass stack at 500 ^{O}C for 20 minutes, crystallization of a-Si started. The crystallization was followed by observing the Raman shift. The phase identification was solely performed with the Raman spectra as $CrSi_2$ and crystalline Si have similar Bragg positions causing ambiguity in determining the phase from X ray diffraction. All the samples show Raman peaks belonging to Cr_2O_3 and $CrSi_2$ peaks. Raman shift of the 10 % chromium doped a-Si thin films after annealing is shown in figure 4.4.1.

The spectral components are de-convoluted into four parts that belong to (a) amorphous Silicon (468 cm^{-1}), (b) hexagonal Silicon (496 cm^{-1}), (c) cubic Silicon (512 cm^{-1}) and (d) Cr_2O_3 (548 cm^{-1}). Once the concentration of Cr was decreased to 5 %, the silicon started crystallizing in wurzite structure. The Raman shift of the wurzite silicon is shown in figure 4.4.2. The presence of the wurtzite structure, in the current case, is confirmed by the prominent Γ_5' resonance peak at 496 cm^{-1}. However, the theoretically predicted resonance peak occurs at 498 cm^{-1} [5]. The downward shift of 2 cm^{-1} can be attributed to the strain or small crystallite size of wurzite silicon. The peak at 548 cm^{-1} belongs to

Cr_2O_3 [6] (Oxide formation is not avoidable in a furnace working in ambient atmosphere). Metal silicide ($CrSi_2$) peaks at 307 and 350 cm^{-1} are also observed in the low frequency part of the Raman spectra [7] shown in the inset of figure 4.4.1.

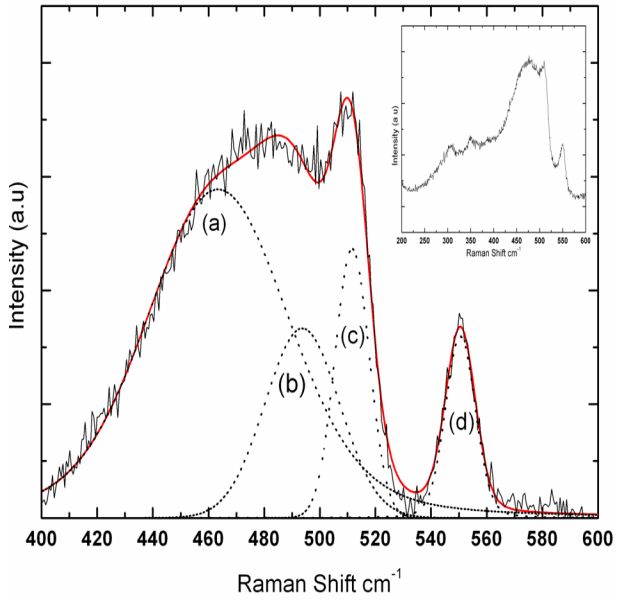

Figure 4.4.1. The Raman spectral components are de-convoluted into four parts that belong to (a) amorphous Silicon, (b) hexagonal Silicon, (c) cubic Silicon and (d) Cr2O3.

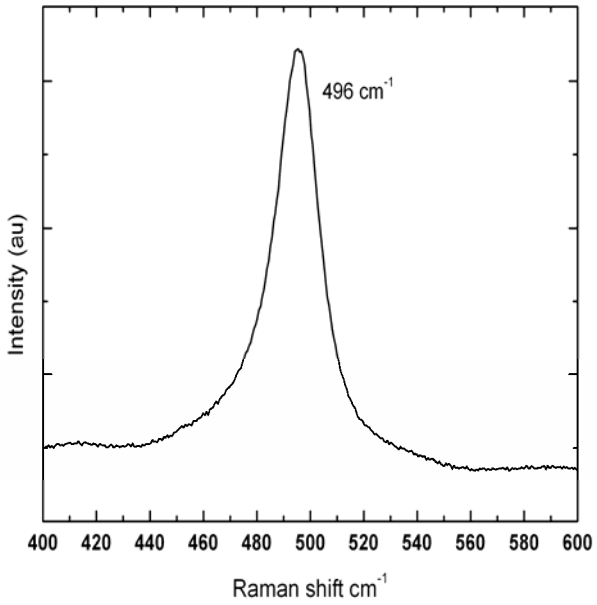

Figure 4.4.2 The Raman shift of the wurzite silicon centered at 496 cm^{-1} due to Γ'_5 resonances.

The morphology of these films is entirely different from that of the Ni induced crystallized Si films.

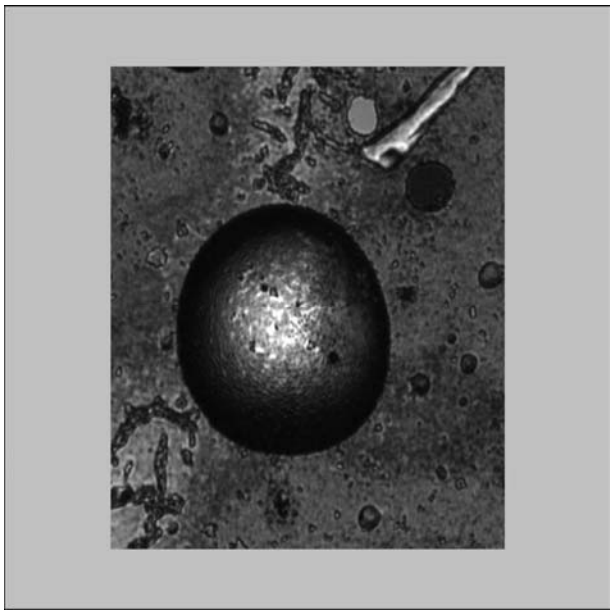

Figure 4.4.3 Wurzite Silicon disc like structures grown on glass

The optical micrograph of Si thin films crystallized in to wurzite Silicon is shown in figure 4.4.3. A disc like structure is the main feature. In degradation studies of $CrSi_2$ lines, Phillips *et al.* [3] have reported the formation of "hillocks" along the edges of the $CrSi_2$ lines. In this particular study the Cr layer is on the top of the a-Si layer. The Si has to come out of the Cr layer, in which there are cracks because of the heat treatment, oxide and silicide formations. Silicon will utilize these openings, and emerge out as hillocks as shown in the figure 4.4.3. These kinds of structures were present through out the sample surface possessing different sizes. The above figure corresponds to the sample with lowest Cr concentration of 5%. As the Cr concentration increases there are morphological changes along with Raman Shift as discussed below. As shown in figure 4.4.1 Cr concentration of 10%, crystallizes the a-Si in two phases Cubic and hexagonal. The optical micrograph is show in figure 4.4.4. The morphological features look similar to those at 5% Cr, but there are still unreacted Cr patches that can be seen as bright spots.

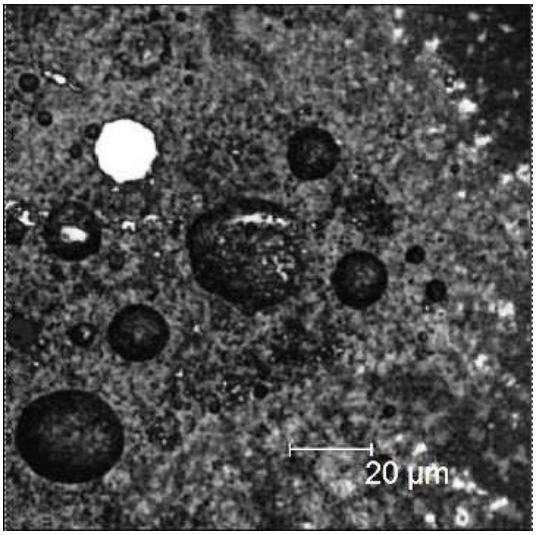

Figure 4.4.4 Optical Micrograph of W-Si on glass crystallized with 10% of Cr.

At higher concentrations of Cr, of 37%, no crystallization of a-Si was observed but $CrSi_2$ and oxide Raman peaks are present. At 12 % of Cr, the Raman spectrum of the w-Si thin films is shown in figure 4.4.5.

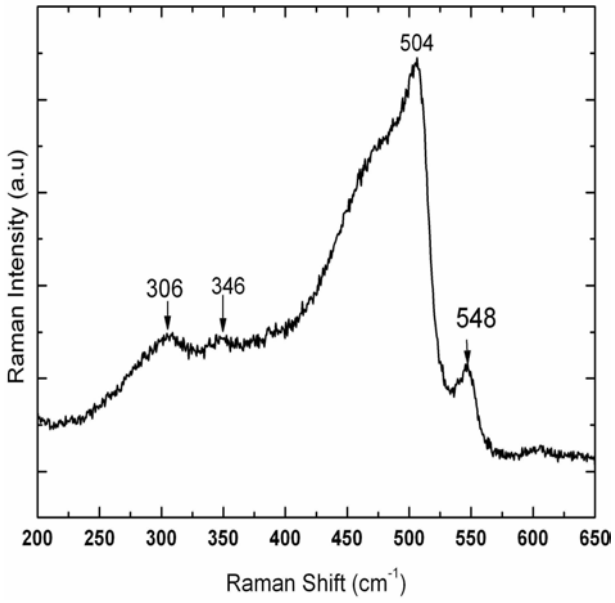

Figure 4.4.5 The Raman spectra of w-Si with Raman peak centered at 504 cm^{-1}

In the figure 4.4.5, 306 and 346 cm^{-1} belongs to $CrSi_2$ while the peak at 548 cm^{-1} belongs to Cr_2O_3 and the 504 cm^{-1} peak is attributed to w-Si. Bandet *et al.* [8] have studied the effect of laser power on the w-Si peak positions and found that with laser power the peaks shifts towards higher wave numbers. The temperature due to local heating has

immense effect on the w-Si Raman peak position. No such peak shift was observed in the current study indicating higher thermal stability.

X ray diffraction patterns of the annealed samples are shown in figure 4.4.6. The unambiguous identification of the presence of crystalline Si is difficult because there is an overlap with the reflections from the silicides. There are 2 Bragg reflections at 2θ values of 78.06^{o} and 105.33^{o}, which can be indexed as originating either from Si or CrSi2. Raman scattering experiments removes the ambiguity, in the determination of phase. However, crystallite size determination from Bragg peak's FWHM shows that the films are nanocrystalline with an average crystallite size of 6 ± 1 nm.

Wurzite Silicon has three vibrational peaks corresponding to the two vibrations in the plane of hexagonal layers and one perpendicular to these layers [5]. Zhang *et al.* have reported wurzite Silicon by laser ablation [9] and they observed Raman peaks at 516 and 518 cm^{-1} due to the hexagonal silicon. In contrast, our investigations indicate that the Si films crystallize in the mixed structure at high Cr concentrations and in the wurzite structure at low Cr concentrations. A possible explanation for the Cr induced crystallization of a-Si is based on the epitaxial growth of Si on $CrSi_2$ Crystallites.

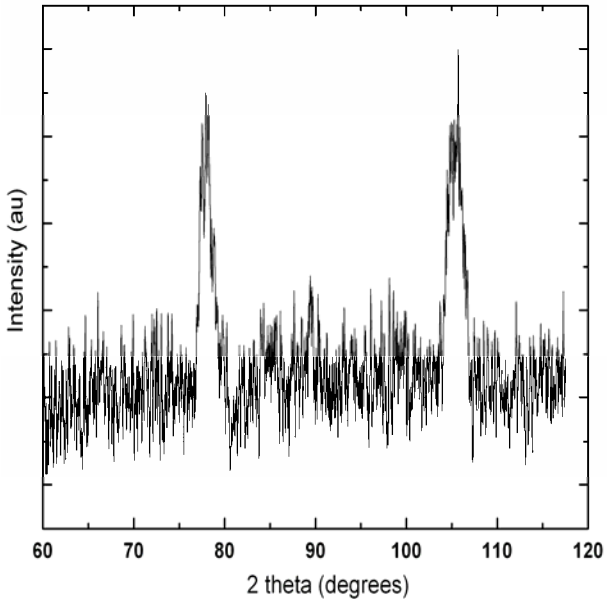

Figure 4.4.6. X ray diffraction pattern of Cr/a-Si/glass after annealing at 500 ^{O}C for 20 minutes showing to Bragg peaks at 2θ degrees of 78.06 ^{o} and 105.33 ^{o}.

A survey of the structures of Cr_2O_3 and $CrSi_2$ reveals that Cr_2O_3 exists in the corundum structure with a space group $R\bar{3}c$ with six formula units in the hexagonal unit cell. The metal ions are located in special positions along the threefold axis at ± [0 0 z ; 0 0 $\frac{1}{2}$+z] and the oxygen lie on diads at ± [x 0 $\frac{1}{4}$; 0 x $\frac{1}{4}$; $\frac{1}{4}$] [27] and in the case of $CrSi_2$ has three formula units per hexagonal unit cell. Its lattice parameters are a = 4.431 Å and c= 6.354 Å [10]. It is, therefore, clear that the silicide and the oxide both exist in the hexagonal form and are structurally isomorphous to the hexagonal form of Si. As a consequence, they act as seeds for the formation of the hexagonal-wurtzite structure of Silicon in the crystallization process.

However, as in the case of Ni induced crystallization here also we believe that the metal atoms play the key role. An interesting point, which is worth mentioning here is that, when Cr reacts with Silicon, ***silicon is the moving species*** and is the only species which moves in the thermal formation of $CrSi_2$. This fact has been proven by Affolter *et al.* [4] in their He Ion back scattering experiments using markers like Mo for Pt_2Si and W for Ni_2Si and $CrSi_2$. When Silicon is the moving species, the kind of epitaxy that occurs is still an open question.

4.4.2 *Spectral transmission*

The spectral transmittance of a 100 nm pure a-Si thin film is shown in figure 4.4.7(a). The spectral transmittance of the same film, with a 30 nm thick Cr thin film blanket is shown in figure 4.4.7(b) and optical transmission of this stack after annealing at 500 ^{O}C for 20 min is shown in figure 4.4.7(c). The transmission spectrum was recorded over the wavelength range of 350 nm to 2500 nm covering the visible and near IR regions.

The absorption edge of the films in the current study is lower than the glass substrate and is therefore not affected by the absorption of the glass substrate. From the figure 4.4.7 a few observations about the films under investigation can be made.

- The percentage transmittance of the pure a-Si film, the film with top layer of Cr and then annealed (here after termed as annealed) differ enormously from each other.

- After annealing, the transmittance is increased from 58% to 78 % between the wavelengths 600 and 700 nm.
- The height of the interference fringe, which is the measure of the refractive index decreases on annealing.
- The absorption edge remains invariant for pure and annealed samples.
- The absorption edge of the as deposited Cr/a-Si seems to be shifted towards low energies.
- The shape of the spectra is similar in the wavelength region of 1200 to 2500 nm, which is dispersion free region.

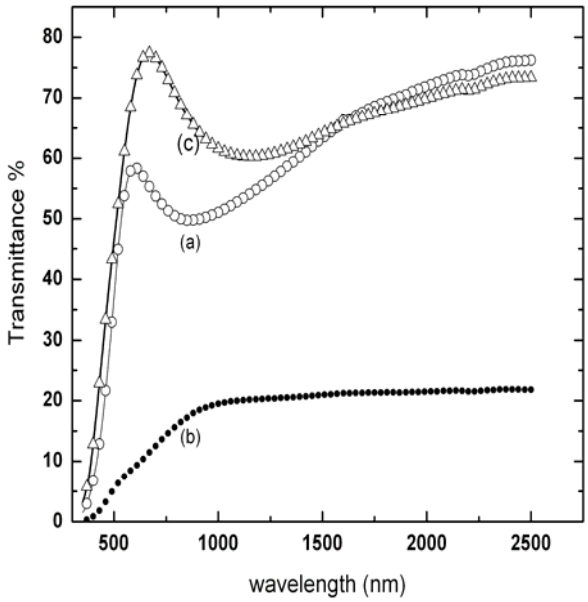

Figure 4.4.7.The spectral transmittance of the 100 nm (a) pure a-Si thin film (b) with a 30 nm Cr thin film blanket (c) after annealing at 500 ^{O}C for 20 min.

4.4.3 *Refractive index behaviour*

The refractive index 'n' is plotted as a function of wavelength in the figure 4.4.8 for the undoped sample and the doped sample. As shown in the figure the refractive index was measured in the range of 450 and 2500 nm. The refractive index of the a-Si thin films as shown in the figure 4.4.8 (*closed circles*) was 3.3, which is in good agreement with the bulk Silicon value of 3.5 at a wavelength of 1100 nm.[12]. The variation in the refractive index of the a-Si and the bulk Silicon was attributed to the density differences between the crystalline and amorphous Silicon. In the figure 4.4.8, the curve shown in *open circles* represents a-Si thin film of 600 nm with a 30 nm of Cr top-layer after annealed at $500^{O}C$ for 20 minutes. After annealing Cr metal reacts with a-Si thin film to form metal silicides like $CrSi_2$ and metal rich silicides like Cr_3Si. Apart from the silicide formation oxidation of metal is also evidenced in our studies. From Raman spectroscopy, we observed the formation of both silicides and oxides of Cr.

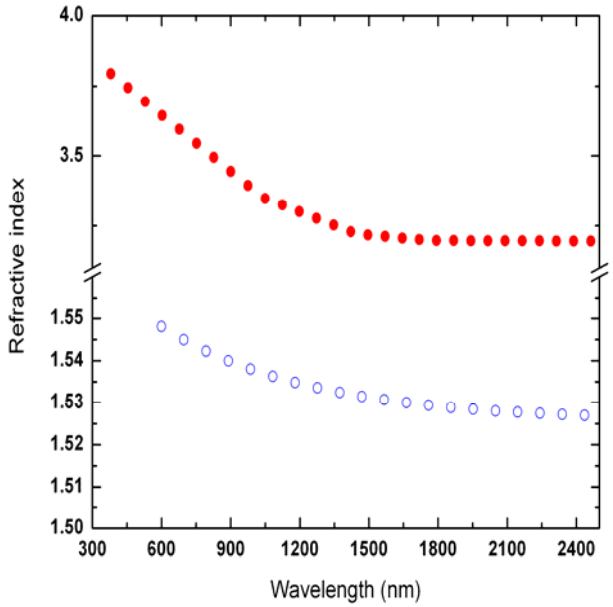

Figure 4.4.8 Refractive index as a function of wavelength for a 600 nm thick a-Si (*closed circles*) thin film after annealing with 30 nm Cr top-layer (*open circles*)

The refractive index is extremely sensitive to the chemical composition of the film under investigation. After annealing, silicides and oxides were formed within the volume as

well as on the surface of the film. All these together affect the overall refractive index. The refractive index, after annealing, decreases to 1.53 at 1100 nm, which is considerably smaller than that of the bulk and amorphous silicon value of 3.3 at 1100 nm. The use of Cr concentration up a level of 50% (alloy concentration) has been tested. The values of the refractive index were affected at lower concentrations and remained same at higher concentration. This was due to the Cr–Si bond formation or due to diffusion of Cr into Si matrix that substantially changed the coordination of Si and thus the refractive index. The relationship between coordination number and refractive index has been explained well by Wemple *et al.* [13] in their classic work about the "refractive index behaviour of semiconducting materials".

4.4.4 *Optical absorption coefficient*

The region between 350 and 800 nm is the high absorption region for a-Si in the transmission spectra and defines the absorption edge. The as deposited and the annealed a-Si thin films show similar absorption edges. A semi logarithmic plot of the absorption coefficients of these films is shown in figure 4.4.9. Both spectra show extremely sharp absorption edges at 0.7 and 0.8 eV.

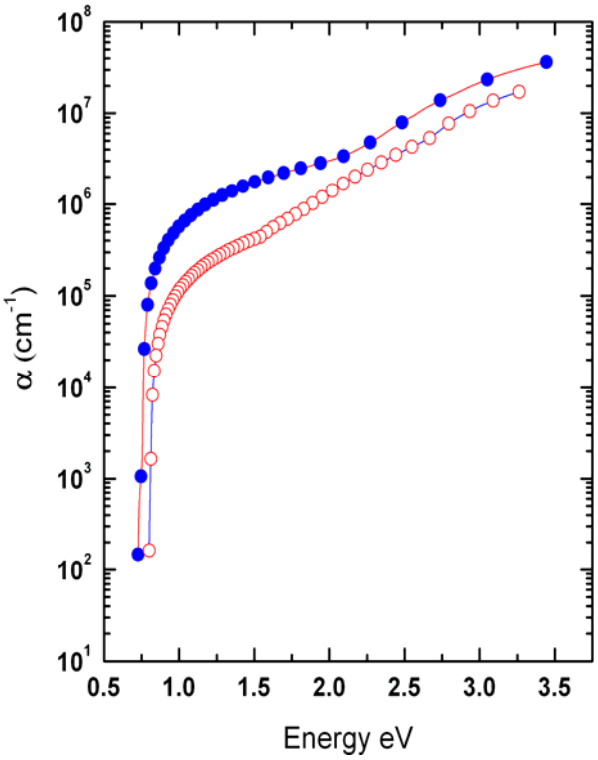

Figure 4.4.9 The absorption coefficient of a-Si thin film (*closed circles*) of 100 nm thickness and after annealing at 500 ^{O}C for 20 min (*open circles*)

A sharp absorption coefficient was observed at the thickness of 100 nm and the sharp nature remained even after annealing. Though, the films shows lowering of absorption coefficient after annealing, the edge is near the photon energy of 0.71 and 0.77 eV; which could be the resultant of combined effect of $CrSi_2$ and silicon band gaps. $CrSi_2$ has a band gap of 0.35 [14] and a-Si band gap varies from 1.4 to 1.8 eV depending on the structural defects and clustering. A detailed explanation will be given in further sections. Cr_2O_3 has

an optical band gap of 4.8 eV [15] and therefore it is believed that it does not affect the band gap of the silicon thin films.

4.4.5 *Band gap Energy*

Optical band gap (Tauc gap) is determined assuming indirect band gap for the a-Si thin films.. The figure4.4.10 (a) shows the extrapolation of linear part in the $(\alpha h\upsilon)^{1/2}$ Vs $h\upsilon$ plot for the two films of thickness 80 and 600 nm whose band gap varied form 1.83 to 1.25 eV. After annealing the band gap behavior with thickness of the a-Si thin films before and after annealing is shown in figure 4.4.10(b). The band gap varied from 2 eV for the 100 nm thick film to 1.3 eV for the film with thickness 600 nm.

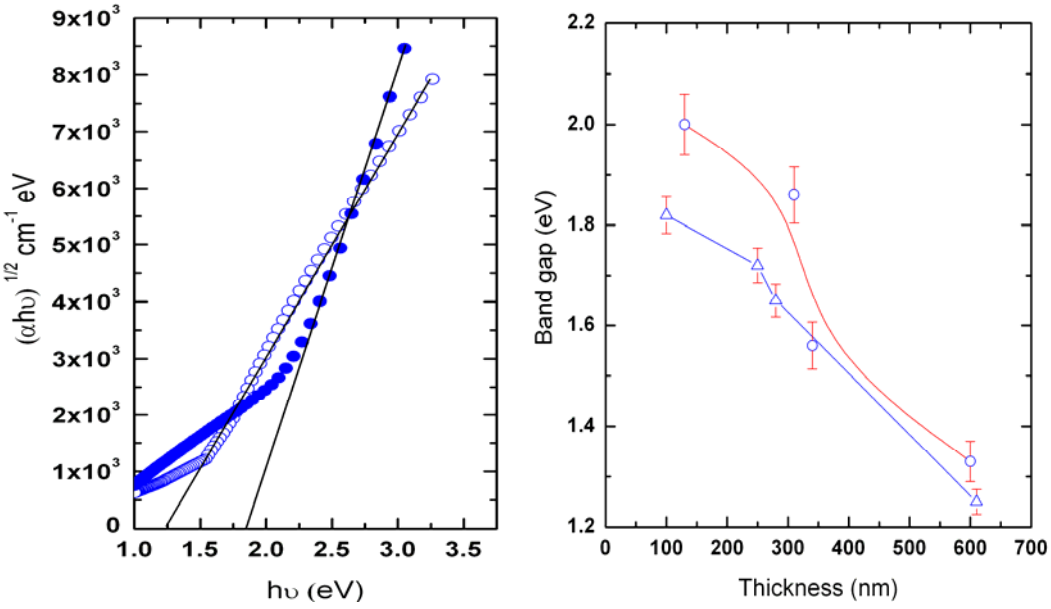

(a) (b)

Figure 4.4.10 .(a) Tauc plot of 80 nm (*solid circles*) and 600 nm (*open circles*) of w-Si thin films (b) the band gap variation with thickness before(*triangles*) and after(*circles*) annealing

Another important optical property is refractive index. The index of refraction is very sensitive to the coordination chemistry and composition. In the present study as mentioned earlier, after annealing, different compounds and of different quantity are found with in the sample and also on the surface. The band gap derived from the Tauc plot represents the mobility gap of the semiconductor. This distinction between mobility gap and optical gap is given by Davis and Mott [16]. It is always found that the mobility

gap is greater than the optical gap. The optical gap presents the gap between localized states, which have already entered the forbidden gap and the mobility gap represents the gap between bottom of the conduction band to the top of the valence band. Thus, the difference between optical gap and mobility gap gives an energy distribution of localized states. Table 1 shows the films of different thickness along with their optical gap and mobility gap.

Table 1

Thickness (nm)	Tauc gap(eV)	Optical gap(eV)	Optical band gap after annealing (eV)
80	1.83	0.74	0.76
90	1.83	0.71	0.73
100	1.84	0.73	0.76
250	1.72	0.74	0.77
280	1.65	0.72	0.68
520	1.25	0.65	0.71

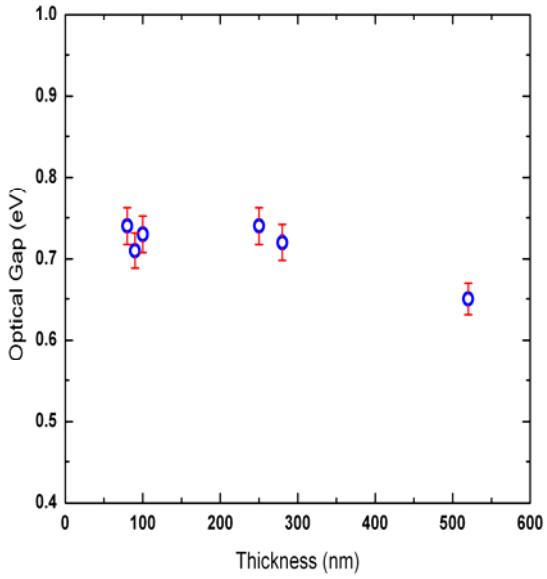

Figure 4.4.11 After annealing- Optical band gap of a-Si thin films of thickness 80 to 520 nm.

The variation in the optical gap with thickness was minimal as shown in the figure 4.4.11. Thus, in all the films the energy states in to the band gap were almost constant and have no dependence with thickness. The optical band gap before and after annealing varies 0.02 to 0.03eV from that of the as-deposited films, which is within the tolerance of the experimental error.

4.4.6 *Summary*

In summary, this section presents the structural, morphological and fundamental optical properties of Silicon thin films, crystallized by Cr metal inclusion and annealed at 500 ^{o}C for 20 minutes. The salient observation are listed below

- At a Cr concentration of 5% Si crystallizes in wurzite form.
- The Raman peak at 496 cm^{-1} was observed experimentally for the first time independent of laser incident power.
- From X ray diffraction line profiles, the crystallite size of w-Si is estimated as 6 ± 2 nm.
- The thin films after crystallization show disc like growth.
- The optical transmittance increased after annealing.
- After annealing refractive index of the thin film decreases to 2.7 at 1200 nm, from 3.4 before annealing. This reduction has been attributed to the silicide and oxide formations, which affect the chemical nature of the film.
- The Raman spectrum shows that Cr induced crystallization of the a-Si thin films occurs in the wurzite form. Thus the reported optical properties belong to the Cr silicide stabilized wurzite silicon.
- The optical band gap is found to remain similar at all the thicknesses.

Reference:

1. B G Yacobi A J Szadkowski and S Zukontynski *J. Appl Phys* **51** 6424 (1980)
2. J R Phillips L R Zheng and J W Mayer *Appl. Phys. Lett* **51** 421 (1987)
3. Jae-Bok Lee, Chan-Jae Lee and Duck-Kyun Choi *Jpn. J. Appl. Phys*. **40** 6177 (2001)
4. K Affolter, X A Zhao and M A Nicolet *J. Appl. Phys.* **58** 3087 (1985)
5. R. J. Kobliska and S. A. Solin, *Phys. Rev. B* **8**, 3799 (1973)
6. Sang-Heon Shim, Thomas S. Duffy, Raymond Jeanloz, Choong-Shik Yoo, and Valentin Iota, *Phys. Rev. B* **69**, 144107 (2004)
7. A Borghesi, A Piaggi, A Franchini, G Guizzetti, F Nava and G Santoro, *Europhysics Letters* **11** 61 (1990)
8. J Bandet, B Despax and M Caumont *J. Phys. D: Appl. Phys*. **35** 234 (2002)
9. Yan Zhang, Zafar Iqbal, Sankaran Vijayalakshmi, and Haim Grebe, *Appl. Phys. Lett.* **75**, 2758 (1999)
10. R. E. Newnham and Y. M. Dehaan *Zeitschrift fiir Kristallographie*, Bd. **117**, 235 (1962)
11. M.A Green, and M Keevers, *Progress in Photovoltaics*, **3** 189 (1995)
12. S. H. Wemple, *Phys. Rev. B* **7** 3767 (1973)
13. L. F Mattheiss, *Phys. Rev. B* **43 1863** (1991)
14. Hong, Seungbum; Kim, Eunah; Kim, Dae-Weon; Sung, Tae-Hyun No Kwangsoo *Journal of Non crystalline solids*. **221** 245 (1997)
15. E. A. Davis, N. F. Mott, *Philosophical Magazine*, **22**, 903 (1970)

Chapter 5

Summary and Scope for Future Work

5.1 Summary

In summary, four kinds of systems have been prepared and characterized, in order to understand the metal induced crystallization in amorphous silicon (a-Si) thin films and to determine their optical properties.

i. Thin films of a-Si on Borosilicate glass grown by thermal evaporation, RF magnetron sputtering and ion beam sputtering,
ii. Ni co-sputtered with Si for EXAFS studies,
iii. Ni over layer on a-Si by evaporation and
iv. Cr over layer on a-Si by evaporation.

Crystallization in a-Si thin films by metal induced crystallization has been observed in all the cases. The thin films were characterized for their crystallographic structure, microstructure, morphology and linear optical properties like refractive index, band gap energy and optical absorption edges for their correlation with local structural order.

It was observed that the as deposited films containing a-Si co-sputtered with Ni did not show any crystalline nature. The local structure was determined by EXAFS experiments. The Ni environment in as-deposited sample is surrounded by 4 Silicon atoms; where as the samples annealed at 600 ^{o}C attains coordination equal to that of $NiSi_2$ structure. At 700 ^{o}C of annealing the Ni attains the environment similar to that of the completely $NiSi_2$ crystalline sample. Based on these results it was concluded that in a pool of Si, nickel has to form silicides. The role of silicide in crystallization is secondary and metal plays the primary role. Metal atoms helps Silicon atoms while bond breaking and making new bonds by supplying extra electrons to share. As a result of co-deposition of metal (Ni) and Si, nickel silicides get trapped inside the Silicon matrix.

When the metal is added to a-Si thin films as an over layer and allowed to diffuse in to upon annealing metal silicide squeezed out of the Si films and due to metal was supplied from the top, silicides move towards the bottom of the film, which is clearly manifested in the optical studies while evaluating the refractive index of these films. In co-sputtering, metal will react with Si and forms metal silicides. This process can crystallize a-Si before all the metal is consumed in silicide formation. But in the case of layered structure the metal supply will be continuous and in small amounts until it reaches the substrate where they form metal silicides with the available a-Si layer. The major advantage of introducing metal as a blanket layer is the entire thin film can be crystallized, whereas co-sputtering gives partial crystallization with $NiSi_2$ nodules remained trapped inside the a-Si matrix deteriorating the optical and electrical properties of a-Si thin film.

Thin film Stacks of Ni/a-Si/glass substrate, with 4.5% of Ni became nano crystalline after an annealing at 600 ^oC for 15minutes with average crystallite size of 6 ± 2 nm. The structural phase and crystallite size was determined by Raman spectroscopy. The fundamental optical constants were determined from spectrophotometric data. The spectral reflectivity indicates the crystalline nature of the films with two characteristic peaks of Silicon at 3.3 and 4.3 eV. The optical absorption edges narrowed after Ni addition and annealing, which signifies improvement in the local structural order. The refractive index as a function of wavelength shows an inhomogeneity in the film due to metal silicide formation. When compared to the samples where metal is co-sputtered, the layered films crystallize at lower temperatures (< 600 ^oC). The Ni concentration and annealing time, temperatures are the key factors to tailor the crystallite size of Silicon.

It has also been found that Cr also induces crystallization in a-Si rather at very low temperatures and duration of annealing. The stabilization of ***wurzite*** Silicon (w-Si) phase in a-Si thin films with 5% Cr and annealed at 500^OC and for 20 minutes has been observed. The prominent Raman central frequency of 496 cm^{-1} peak was experimentally recorded for the first time in our films. The optical properties of these

films were not entirely different from cubic Silicon but band gap varies with crystallite size but this may be attributed to the quantum confinement in w-Si. The crystallite size derived from X ray diffraction the size of the crystallite was found to be 6 ± 2 nm.

A number of pure a-Si samples in order to estimate the Silicon thin film quality were also prepared by Ion beam sputtering and thermal evaporation. Their optical properties were thoroughly investigated and found in good agreement with earlier intrinsic Silicon thin films. Amorphous Silicon thin films were prepared by ion beam sputtering also with an aim of finding a suitable method for the preparation of "low defect density a-Si". The defects offer one kind of disorder apart from the absence of long range order. These phenomena are addressed in terms of Urbach edge shape and width.

5.2 Scope for future Work

Although some insight into lowering of crystallization temperature of a-Si when in contact with metal species has been achieved, much more still remain as open questions. While Ni and Cr start crystallizing a-Si, it is interesting to study Si local structure by measuring X ray absorption at Si K-edge. The optical properties of the MIC crystallized Silicon are promising for many applications, but the full potential of the material can be evaluated only after thorough studies on electrical properties. Ion beam sputtering (IBS) can be a viable method to prepare a-Si thin films on glass with low defect density. In order to find correlation between optical properties and local order, these IBS grown a-Si thin films are interesting systems of their own kind. Doping and band tailing studies can be much more interesting in technological point view. The ultimate test for these materials would be to put them into devices such as Thin Film Transistors (TFT) for displays and PV Cells.

List of Publications:

- N.D. Afify, G. Dalba **U. Mahendra Kumar Koppolu**, C. Armellini, YJestin F. Rocca, "*XRD and EXAFS studies of HfO_2 crystallization in SiO_2 - HfO_2 Films*", *Materials Science in Semiconductor Processing* 9, 1043 (2006).

- **K. Uma Mahendra Kumar**, Rajeeb Brahma, M Ghanashyam Krishna and A K Bhatnagar, "*An Optical study of Ni induced crystallization of a-Si thin Films"* *J. Phys.: Condens. Matter*. **19** 496208 *(2007)*

- **K. Uma Mahendra Kumar** and M. Ghanashyam Krishna, "C*hromium-Induced Nanocrystallization of a-Si Thin Films into the Wurtzite Structure," Journal of Nanomaterials*, **2008**, Article ID 736534 (2008)

- **K. Uma Mahendra Kumar**, R. Grisenti, G. Dalba, P. Fornasini, I. Chambouleyron and R. Zanatta, M. Ghanashyam Krishna "*XAFS study of Ni surroundings in Metal Induced Crystallization of thin film amorphous silicon*".(*in communication*)

- **K. Uma Mahendra Kumar**, M Ghanashyam Krishna *Urbach edges in ion beam sputtered a-Si thin Films*, (*under review)*

Conferences (International / National):

- **Uma Mahendra Kumar**, Rajeeb Brahma, M Ghanashyam Krishna and A K Bhatnagar, "Self Organized Nanostructured semi conducting thin Films", *International Conference on Nano Science & Technology ICONSAT 2006,* New Delhi, India, (March, 2006).

- **Uma Mahendra Kumar** Koppolu, R. Grisenti, G. Dalba, P. Fornasini, I. Chambouleyron and R. Zanatta, M. Ghanashyam Krishna, "XAFS study of Ni surrounding in Metal Induced Crystallization (MIC) of thin film amorphous silicon", *European Material conference, European Material Research Society, Spring meeting,* Nice, France, (June 2006).

- **Uma Mahendra Kumar**, Rajeeb Brahma, M Ghanashyam Krishna and A K Bhatnagar, " *Optical properties of ion beam sputtered wide band gap a-Si thin films" International conference on Ion beam analysis,2007;* Hyderabad Sept 2007.

Oral Presentation:

- **K. Uma Mahendra Kumar**, Rajeeb Brahma, M Ghanashyam Krishna and A K Bhatnagar "Nickel Induced Crystallization in Thermally evaporated a-Si Thin Films", *National Conference on Smart Materials and recent Technologies, SMART 2007,* Tirupati India, (Feb, 2007).